1-29-2016

An Investigation of Agricultural Produce Cooling Tunnel Performance

Jean-Paul Edward Martins
University of Windsor

Follow this and additional works at: https://scholar.uwindsor.ca/etd

Recommended Citation

Martins, Jean-Paul Edward, "An Investigation of Agricultural Produce Cooling Tunnel Performance" (2016). *Electronic Theses and Dissertations*. 5650.
https://scholar.uwindsor.ca/etd/5650

An Investigation of Agricultural Produce Cooling Tunnel Performance

by

Jean-Paul E. Martins

A Thesis
Submitted to the Faculty of Graduate Studies
through the Department of Mechanical, Automotive & Materials Engineering
in Partial Fulfillment of the Requirements for
the Degree of Master of Applied Science
at the University of Windsor

Windsor, Ontario, Canada

2016

An Investigation of Agricultural Produce Cooling Tunnel Performance

by

Jean-Paul E. Martins

APPROVED BY:

_____
Dr. T. Bolisetti
Department of Civil and Environmental Engineering

_____
Dr. B. Zhou
Department of Mechanical, Automotive & Materials Engineering

_____
Dr. G. W. Rankin, Advisor
Department of Mechanical, Automotive & Materials Engineering

January 21st 2016

Declaration of Originality

I hereby certify that I am the sole author of this thesis and that no part of this thesis has been published or submitted for publication.

I certify that, to the best of my knowledge, my thesis does not infringe upon anyone's copyright nor violate any proprietary rights and that any ideas, techniques, quotations, or any other material from the work of other people included in my thesis, published or otherwise, are fully acknowledged in accordance with the standard referencing practices. Furthermore, to the extent that I have included copyrighted material that surpasses the bounds of fair dealing within the meaning of the Canada Copyright Act, I certify that I have obtained a written permission from the copyright owner(s) to include such material(s) in my thesis and have included copies of such copyright clearances in Appendix A.

I declare that this is a true copy of my thesis, including any final revisions, as approved by my thesis committee and the Graduate Studies office, and that this thesis has not been submitted for a higher degree to any other University or Institution.

Abstract

The goal of this research is to numerically and experimentally investigate the performance of a forced air agricultural produce cooling tunnel. A porous medium approach is used to represent the produce within the containers in the numerical model. The pressure loss coefficients associated with the porous media are determined experimentally, while the heat transfer coefficients are obtained using empirical relationships from the literature. Full scale experimental studies, within a production setting, indicate a high variation in initial product temperatures and varying cold room temperatures over time. The numerical model is modified based on these findings and compared with experimental results. The numerical model shows good agreement with experimental values of pressures and the discrepancies are reduced if leaks are estimated. The numerical and experimental transient temperature variations are shown to be in significant disagreement, which indicates that alternative methods of determining the heat transfer coefficient are required to accurately determine the performance.

Dedication

I dedicate this work to my wife Jenna, and to my son Maxim. Thank you for your undying love and support.

Acknowledgments

Table of Contents

List of Figures

xii

List of Tables

List of Appendices

Nomenclature

A	Area
A_t	Area of Throat
a_{fs}	Specific Surface Area
B_f	Body Forces
C	Specific Heat of Solid
C_d	Discharge Coefficient
C_p	Specific Heat of Fluid at Constant Pressure
C_2	Forchheimer Drag Coefficient
c_F	Forchheimer Constant
d_p	Particle Diameter
E	Total Energy
e_i	Error of Type i
F	External Forces
g	Acceleration Due to Gravity
h	Heat Transfer Coefficient
h_{fs}	Fluid to Solid Heat Transfer Coefficient
h_i	Sensible Enthalpy of Species i
h_p	Pressure Head
h^*	Equivalent Heat Transfer Coefficient
J_i	Diffusion Flux of Species i
K	Permeability
K_1	Hydraulic Conductivity
k	Thermal Conductivity
L	Characteristic Length
Nu_{fs}	Fluid to Solid Nusselt Number
P	Pressure
Pr	Prandtl Number
P^*	Dimensionless Pressure
Q	Volume Flow Rate
q'''	Heat Generated per Unit Volume
Re_p	Particle Reynolds Number
S^h	Enthalpy Source
T	Temperature

T_i	Initial Temperature
T_r	Lowest Room Temperature
T(t)	Instantaneous Temperature
t	Time
U_c	Instrument Error Uncertainty
U_d	Design Stage Uncertainty
U_o	Zero Order Uncertainty
U_R	Uncertainty in Function R
V	Intrinsic Average Velocity
V_t	Velocity at the Throat
v	Superficial Velocity
z	Vertical Elevation
β	Geometric Heat Transfer Parameter
β_d	Ratio of Diameters
μ	Viscosity
$\tilde{\mu}$	Equivalent Viscosity
ρ	Density
τ	Dimensionless Temperature
τ_s	Shear Stress
φ	Porosity
∂	Partial Derivative Operator
$\vec{\nabla}$	Del Operator
$\vec{\nabla}^2$	Laplace Operator
$\forall$	Volume

1. Introduction

Leamington is a municipality within Essex County, Ontario, which boasts the largest concentration of greenhouses in North America. A number of agricultural product handling facilities exist in the surrounding area to support the greenhouse community. The agricultural commodities pass through various postharvest processes at the handling facility, which can include, cooling, cleaning, sorting, and packaging. The overall care taken in the postharvest processing stages greatly affects the resulting quality of the produce. It is widely accepted that cooling of the agricultural product to the proper level is paramount in maintaining produce of high quality. The importance is so great that retail stores supplied by the product handling facilities refuse to accept produce shipments not cooled to a sufficient level.

Clifford Produce, a local produce handling facility, has been cooling produce by placing it in cool rooms and relying on natural convection, which requires a number of days to achieve. The result of the long cooling time is their inability to supply certain orders, and hence loss of revenue. This generated their interest in a rapid cooling alternative to their current method of room cooling. Many methods of postharvest cooling are available to the product handlers, but forced air cooling is the most popular. Clifford's main concern was to be able to reduce the cooling times of their produce and to be able to estimate the expected cooling times and operating conditions of a force air cooling system for the range of products they handle as well as investigate the relative merits of various pallet-stacking configurations.

Mathematical models are of great use when trying to predict and understand the forced air cooling process. Many authors have investigated the modeling of forced air cooling of agricultural products using different approaches. In general, three modeling methods are available, with varying computational cost for each; however, each approach is product and configuration specific. The literature offers some guidance regarding modeling a forced air cooling process specific to Clifford's needs.

This thesis involves the development of a simplified numerical model using commercially available software. The complex geometry and flow conditions inside the

produce containers are approximated using a porous media approach. The method is semi-empirical as the loss coefficients associated to the specific product containers and produce within are determined experimentally. The numerical model is then compared with full-scale experiments and any discrepancies investigated.

2. Literature Review

2.1 Postharvest Cooling

Postharvest cooling was introduced to the US Department of Agriculture by Powell in 1904, as mentioned by Brosnan [1]. Postharvest cooling is also widely known as pre-cooling. It is defined as the rapid removal of field heat from an agricultural product after harvest [1].The purpose of this process is to reduce the respiration rate of the living agricultural commodity. The rate of decay is proportional to the respiratory metabolism of the product, thus; reduced respiratory rates yield longer shelf life [2]. Generally, it is accepted that postharvest cooling is paramount in achieving long shelf life [1]. Other positive consequences are: less water loss (wilting), reduced amounts of molds and bacteria, and lower production of ethylene [3]. Some common methods of pre-cooling are room cooling, forced air cooling, vacuum cooling, package icing, hydro cooling and finally cryogenic cooling. These methods exist in many similar but different configurations tailored to the product handler's specific needs. The selection of the pre-cooling method depends on the nature of the product, packaging requirements, product flow, and economic constraints [1].

2.2 Forced Air Cooling

The forced air cooling method is a modification of the room cooling method in which the boxes filled with produce are placed in a cold room, and allowed to cool under natural convection conditions in relatively stagnant air. In forced air cooling, high capacity fans pull cool air from the room directly over the product. As can be seen in Figure 1, cold air is drawn into openings of the packaging containers and over the produce driven by the negative (vacuum) pressure generated by an axial fan. Forced air cooling generally cools the produce 4 to 10 times faster than room cooling [1]. Pulling the air through the produce is recommended rather than blowing it, since the air is less susceptible to bypass and yields more homogenous temperatures throughout [4].
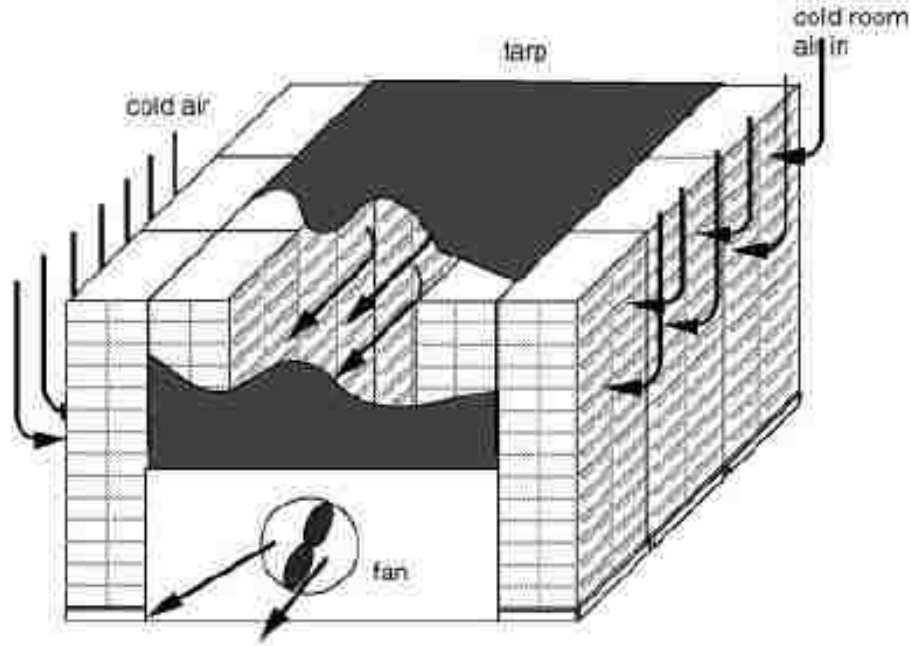
Figure 1: Forced Air Cooling Tunnel [5] Copyright © 2008 Regents of the University of California. Used by permission

Selection of the fan is based upon the flow rate required to cool the produce. The cooling rate is strongly dependent on the velocity and temperature of the flowing air. Forced air cooling is a desirable solution for product handlers who are currently using the room cooling method because it requires minimal investment in new equipment. It is also desirable since it can cool a variety of agricultural products within their respectively different shipping containers [4]. For these reasons forced air cooling is the most popular commercial postharvest cooling method [6].

2.3 1/2 and 7/8 Cooling Times

The 1/2 and 7/8 cooling times are standard terms that originate from the food product handling industry. They are defined as the times required in reducing the product temperatures by one half and seven eights of the initial temperature difference between the product and the cooling medium respectively [2]. They are graphically presented in Figure 2 and will be different for produce located at different points within the flow field. These times can be used as a benchmark for performance, where higher cooling times indicate poor performance, and low cooling times indicate good performance. The

cooling rate is dependent on the difference in the air and produce temperatures and hence is highest when cooling begins and lowest near the end of the cooling process.
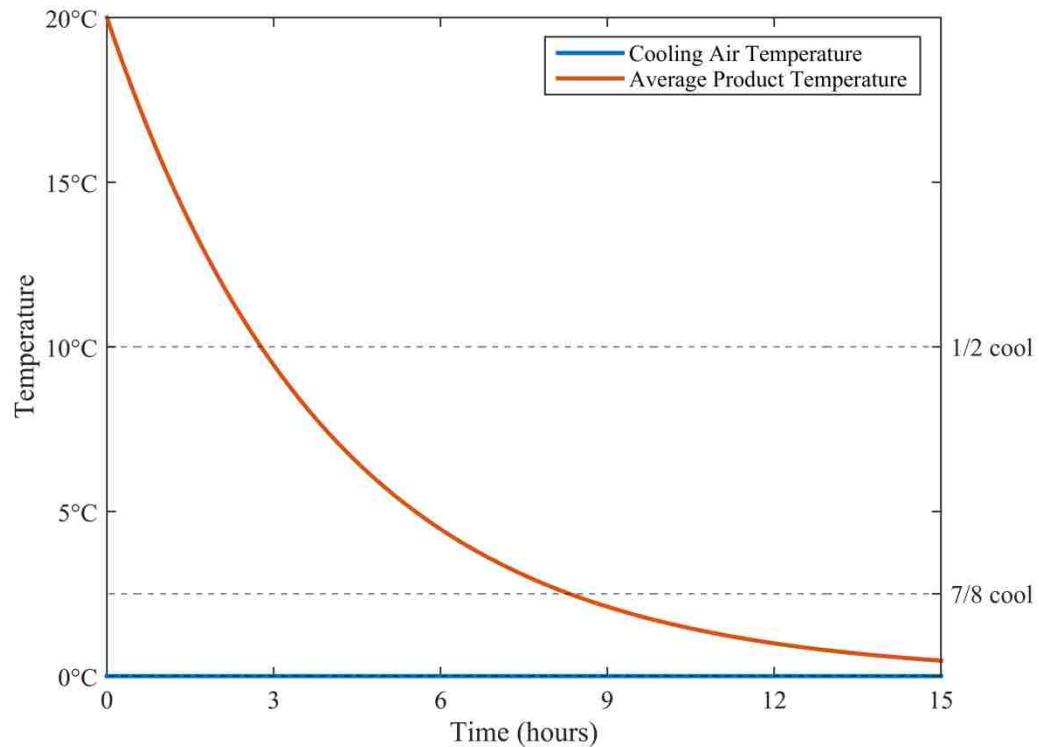
Figure 2: Cooling Curve

2.4 Modeling Approaches

It is convenient to separate the different approaches to modeling velocity and heat transfer in forced air produce cooling into three categories: zoned, fully distributed, and porous medium.

2.4.1 Zoned Approach

In the case of zoned modeling, the flow domain is separated into a number of regions or zones. The desired flow variables in each zone are described using ordinary differential equations since the air within each zone is assumed to be perfectly mixed and hence have uniform conditions. Transport of the fluid through each zone is modeled using a plug flow approach or by some other approximation. In the plug flow approach, the zones are arranged in such a way that the flow moves through the zones successively as it would physically. In the case of zoned models, only the average fluid concentrations and

temperatures in each zone are determined. Momentum equations are in general not solved, but rather data for the fluid velocity is obtained experimentally [7]. Zoned models are the least computationally expensive models, but since the airflow is based on empirical data, it is difficult to apply these models to different package designs and product arrangements.

Amos [8] used this type of approach, in 1995, to model the cooling of apples. Within his research, the airflow in each zone is modeled based on the total mass flow and proportioning coefficients based on measured velocities within product containers. It is concluded that, further measurements were required to accurately predict the cooling of alternative packaging systems. He states the major weakness of his modeling approach is the description of the airflow between zones.

In 2002, Tanner et al [9] attempted to increase the generality of the zoned approach. The authors were successful in developing a more general model by including sub-models for heat and mass transfer. The sub-models are modified at any time without affecting each other, which gives good flexibility. Although the generality of the zoned model approach increased, the main drawbacks remained, namely the requirement of extensive good quality input data for the operating conditions such as data for the external environment and airflow between zones.

2.4.2 Fully Distributed Approach

The fully distributed models apply computational fluid dynamic (CFD) methods to solve two-dimensional (2D) or three-dimensional (3D) equations of momentum transfer (Navier-Stokes), mass conservation (continuity), and energy transfer (First Law of Thermodynamics). With this method researchers are able to solve for air velocity, temperature and humidity ratio, as well as product temperature [7]. To achieve reasonably correct results, accurate models for effects such as turbulence and convective heat transfer at the differential level are required as well as a large amount of computing capacity. When modeling transport within the produce package, a complex grid system is necessary to model the complicated geometry within the produce package.

In 2008, Ferrua and Singh [10] investigated the forced air cooling of strawberries within their clamshell packaging with the fully distributed approach. From their computational results, they concluded that approximately 75% of the airflow bypasses the clamshells

entirely. They also observed that approximately 46% percent of the air that did enter the clamshells bypassed the strawberries entirely. This behavior is observed to increase the heterogeneity of the temperatures of the cooled strawberries. Ferrua and Singh [11] also conducted experiments with a simplified geometry to validate their numerical model. They observed good agreement between their experimental and numerical results concluding the observed differences could be explained by considering the limits of the experimental uncertainty. The fully distributed approach can therefore be assumed to be the most accurate approach, but also the most computationally expensive.

2.4.3 Porous Media Approach

Porous media models use a macroscopic volume-averaged approach to approximate the complex flow phenomena throughout the produce containers. The complicated discontinuous configuration of air space and produce within the container is modeled as a continuous distribution of air and produce that have uniform properties. The macroscopic continuity, momentum, and energy equations for the air and produce are solved to determine the volume-average fluid velocity and temperature, as well as produce temperature variation within each container. Some information is lost in the volume-averaging process, therefore; some empirical models are needed for closure of the equations. The empirical relationships are necessary for quantities such as the porosity, permeability, Forchheimer constant, thermal and mass dispersion, and interfacial heat transfer coefficient [7]. The porous media approach removes the need to generate complex meshes to describe the complicated geometry associated with produce in its container. Instead, a more simple structured mesh can be used. In general, the porous media approach is more computationally expensive than the zoned approach but less expensive than the fully distributed approach.

The use of the porous media model to simulate forced air cooling of agricultural produce was first introduced by Talbot [12] in 1988. The author used commercial finite element software to model the pressure drop and velocity within a container containing oranges. Experiments were also conducted by Talbot to validate the numerical model. Although Talbot observed significant disagreement between numerical and experimental temperatures, he concludes that the porous media model coupled with the appropriate

heat transfer model is a valuable tool that can be used on practically any configuration concerning forced air cooling of agricultural products.

Another attempt at modeling forced air cooling of agricultural produced was made by Xu and Burfoot [13] in 1998. The authors conducted a 3-D numerical analysis on the forced air cooling of potatoes. They compared their numerical results with the experimental results of Misener and Shove[14] from 1967. Good agreement between their numerical and the experimental results was found with differences of up to 1.4°C. The numerical model also included moisture transfer and was able to simulate the total produce weight loss by drying to within 4.5% of the experimental results.

In 2006, Verboven et al.[15] conducted a review on advances in modeling the transport phenomena in refrigerated food bulks, packages, and stacks. The authors summarized the strengths and weaknesses of recent approaches taken by various researchers. Within their summary, the authors state that few researchers have addressed the package itself (containing the produce) as a source of resistance to the airflow. Their summary concluded that great care is required in order to successfully implement a porous media model to simulate forced air cooling of agricultural produce. Transport phenomena are complicated for many reasons including variations in size and shape of the products, venting of packages, and the presence of turbulence. They also mentioned the popularity of direct numerical simulations (fully distributed approach) as they offer valuable fundamental understanding of the underlying process, but at a significant computational cost.

2.5 Historical Background of the Porous Media Model

Henry Darcy published a report in 1856 regarding the construction of a municipal water system in Dijon, France [16]. Within the report is a relationship for the flow rate of water through sand filters similar in form, but symbolically different than Equation 1.

$$Q = AK_1 \frac{(h_{p1}-z_1)-(h_{p2}+z_2)}{L} \tag{1}$$

In this equation, Q is the volume flow rate and, A is the cross-sectional area of the sand filter. K_1 is the hydraulic conductivity of the sand and, L is the distance between the two pressure taps used to measure the pressure difference. The symbol h_p represents the pressure head while z is the vertical elevation. The most notable parameter in Equation 1

is the hydraulic conductivity K_1, which requires experimental determination. Darcy conducted careful experiments using a vertical steel column filled with sand as schematically shown in Figure 3. The column was instrumented with mercury manometers to measure the pressure head. The volume flow rate was determined by measuring the total volume that was collected in the basin and dividing it by the total experiment time.
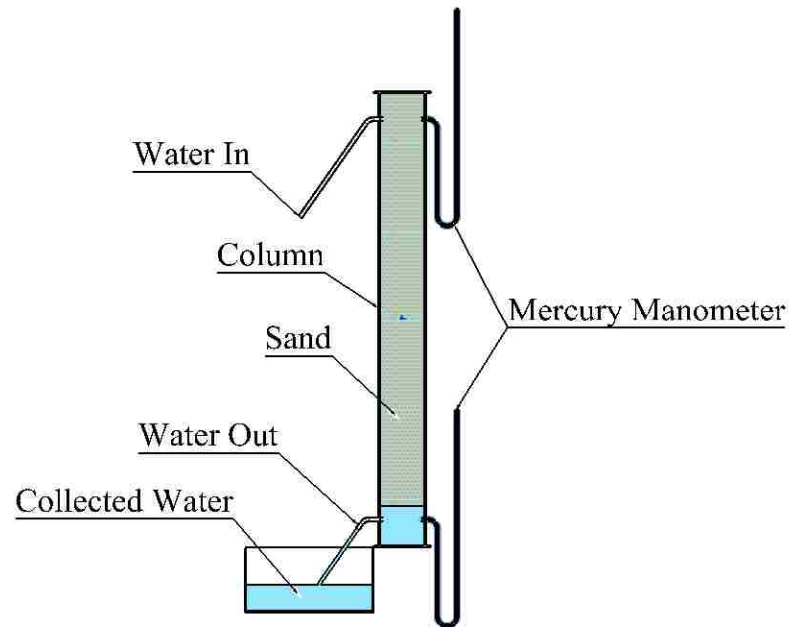
Figure 3: Darcy's Experiment

Darcy used this data and equation to determine the hydraulic conductivity of the sand filter and validate his newly discovered equation which forms the basis of the porous media model [17].

2.6 Porous Media in Detail

In general, a porous medium consists of a solid matrix with voids that are interconnected. In most, but not all cases, the solid matrix is rigid. The network of voids or pores allows for the transport of one or more fluids. Some examples of naturally occurring porous media include sand, limestone, and the human lung [18].

2.6.1 Microscopic vs Macroscopic

The microscopic approach to analyzing flow through a porous media is to consider every void and obstruction in the flow domain. Modeling with the microscopic approach involves solving the equations of motion for the flow variables within the voids. The voids in this approach are generally irregular, and if the flow domain is large and considers many voids, the solution becomes computationally expensive [18]. Alternatively, the macroscopic approach involves determining a representative elementary volume (REV) seen in Figure 4. The entire flow domain then takes on the properties of the REV and the porous media equations solved to obtain the flow variables. Experimentally measured flow variables are averages of the values over areas that cross many pores much like the REV. These flow variables are considered to be continuous with respect to space and time [18]. The macroscopic approach involves the loss of some information on the pore scale, but has the advantage of being less computationally expensive than the microscopic approach.
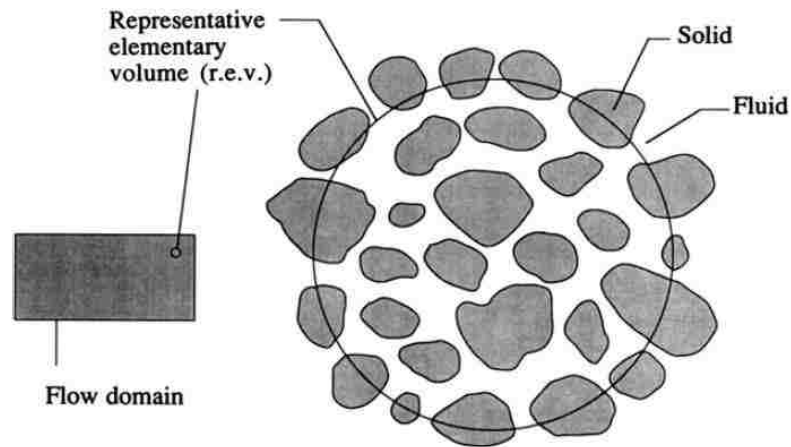
Figure 4: Porous Media [18]

2.6.2 Porosity

The porosity, φ, is defined as the ratio of void volume in the REV to total volume of the REV as described in Equation 2.

$$\varphi = \frac{Void\ Volume}{Total\ Volume} \tag{2}$$

It follows that $1 - \varphi$ is the ratio of solid matrix to total volume of the REV. In the case that the porous medium is isotropic, the porosity can be calculated as the ratio of void area divided by the total area.

2.6.3 Darcy Velocity

A continuum flow model is created with a Cartesian reference frame based on the macroscopic REV approach. It is assumed that the volume elements are sufficiently large compared to void volumes to yield reliable volume averages. Simply put, the porosity is independent of the choice of the location of the REV within the flow domain [18]. When averages of the variables are taken with respect to the medium (both solid and fluid), those variables are denoted with a subscript m. Similarly, if the average of the variable is taken with respect to the fluid only, those variables will be denoted with the subscript f. In the case of a single phase fully immersed porous medium, the void volume can be denoted as $\forall_f$. Equation 1 divided by the total cross-sectional area of the porous material results in a velocity. In Darcy's experiments the area is defined as the cross-sectional area of the column. This means that the resultant velocity represents the volume average velocity with respect to the medium. In general, the velocity can be a vector of three components. The velocity v has been given different names by many authors including, seepage velocity, filtration velocity, superficial velocity, Darcy velocity, and volumetric flux density. The terms Darcy and superficial velocity are employed in this thesis. It is important to note that the Darcy velocity does not represent the velocity of the fluid within the voids of the porous medium. The intrinsic average velocity of the fluid, V, more accurately represents the true velocity of the fluid flowing within the pores. The Darcy velocity v and the intrinsic average fluid velocity V are related using the Dupuit-Forchheimer relationship given by Equation 3 [18].

$$v = \varphi V \tag{3}$$

2.6.4 Continuity

With the continuum in mind, the usual arguments are applied to derive differential equations to express the conservation laws. One such equation is the conservation of fluid mass or continuity equation represented by Equation 4.

$$\varphi \frac{\partial \rho_f}{\partial t} + \vec{\nabla} \cdot \left(\rho_f \vec{v} \right) = 0 \tag{4}$$

The density of the fluid is denoted by ρ_f. Equation 4 is derived using an elementary unit volume of the medium and equating the rate of increase of the fluid mass within that volume $\varphi \frac{\partial \rho_f}{\partial t}$, to the net mass flux into the volume $\vec{\nabla} \cdot (\rho_f \vec{v})$. It is important to note that the porosity φ is assumed to not be a function dependent on time.

2.6.5 Darcy's Law

In the current literature, Darcy's Law for one-dimensional flow through a differential element is typically represented as seen in Equation 5 [18].

$$u = -\frac{K}{\mu}\frac{\partial P}{\partial x} \tag{5}$$

Equation 5 is very similar to Equation 1 if Darcy's column is to be considered to be lying on its side, depicted in Figure 5. In such a case, the z terms cancel because there is not a change in elevation and the velocity is in the x direction.
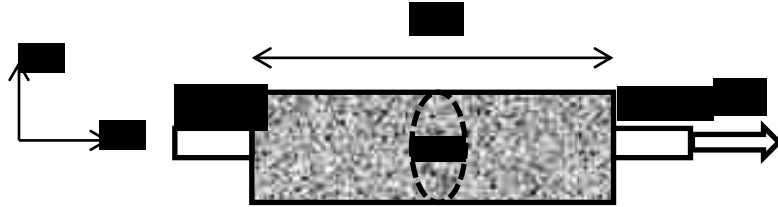
Figure 5: Horizontal Flow in a Porous Medium

In the current version of the equation $\partial P/\partial x$ represents the pressure gradient in the x direction. If the pressure gradient $\partial P/\partial x$ is constant, it is equal to $-(h_{p1} - h_{p2})\rho g/L$, and ∂x is L. Since u is equal to Q/A the permeability K is equal to $\mu K_l/\rho g$. The more recent form of Darcy's Law is independent of the properties of the fluid and hence, depends only on the nature of the medium. When considering Darcy's law in three dimensions, Equation 6 takes the form seen in Equation 6 [18].

$$\vec{v} = \mu^{-1}\vec{K}\,\vec{\nabla}P \tag{6}$$

Equation 6 represents the case where the permeability is anisotropic in which case $\vec{K}$ is a diagonal tensor. Alternatively, in the case where the porous medium is isotropic Equation 6 simplifies to Equation 7.

$$\vec{\nabla}P = -\frac{\mu}{K}\vec{v} \tag{7}$$

The term on the right hand side of Equation 7 is known as the Darcy term. Many authors have conducted experiments and have verified Darcy's law.

2.6.6 Forchheimer's Equation

In Darcy's Equation 7, the pressure gradient is linearly related to the Darcy velocity. This relationship is valid only if the superficial velocity is sufficiently small. The velocity is considered to be sufficiently small if the particle Reynolds number is of the order of unity or less. The particle Reynolds number is defined much like the general Reynolds number, where the length scale is the diameter of the particle seen in Equation 8.

$$Re_p = \frac{\rho v d_p}{\mu} \tag{8}$$

As the particle Reynolds number increases past unity and up to 10, there is a smooth transition from linear pressure drop to quadratic pressure drop. It is important to note that this transition is not a laminar to turbulent transition, since the Reynolds numbers are still quite small. It is believed that the transition is due to the form drag from the solid obstacles being comparable, in magnitude, with the surface drag due to friction [18]. At higher particle Reynolds numbers it is advisable to use a modification of Darcy's equation seen in Equation 9 known as Forchheimer's equation.

$$\vec{\nabla}P = -\frac{\mu}{K}\vec{v} - c_F \vec{K}^{-1/2}\rho_f|\vec{v}|\vec{v} \tag{9}$$

In Equation 9, c_F is a dimensionless form drag constant also known as the Forchhiemer constant. Following the previously stated convention, ρ_f represents the density of the fluid. The second term on the right side of Equation 9 is referred to as the Forchhiemer term. Equation 9 correlates well with experimental data.

2.6.7 Brinkman's Equation

Another modification of Darcy's equation is known as Brinkman's equation seen in Equation 10.

$$\vec{\nabla}P = -\frac{\mu}{K}\vec{v} + \tilde{\mu}\vec{\nabla}^2\vec{v} \tag{10}$$

The second term on the right hand side of Equation 10 is known as the Brinkman term and is analogous to the Laplacian term seen in the Navier-Stokes equation. The symbol $\tilde{\mu}$ represents the effective viscosity. Brinkman equates $\tilde{\mu}$ to μ, but this should not be the case in general. In general, the relationship of $\tilde{\mu}/\mu$ depends on the geometry of the medium and can be greater or less than unity. It is believed that Brinkman's equation should be restricted to cases where the porosity is greater than 0.6[18]. There has been limited research in the validation of Brinkman's equation. For many practical purposes, the inclusion of the Brinkman term is not needed. The Laplacian term is however required if one aims to model the no-slip boundary condition.

2.6.8 Energy Equation

In order to model changes in temperature the equation for energy or first law of thermodynamics must be included in the solution. The equation must be written separately, for each of the solid matrix and fluid phase(s). Within this work, it will be assumed that the porous medium is isotropic and radiation, viscous dissipation, and pressure work are negligible.

2.6.9 Local Thermal Non-Equilibrium

If it is required to model the heat transfer between the solid and fluid, then they must not be in thermal equilibrium. In such cases, the energy balance for the solid and fluid can be described by Equations 11 and 12 respectively.

$$(1-\varphi)(\rho C)_s \frac{\partial T_s}{\partial t} = (1-\varphi)\vec{\nabla}\cdot\left(k_s\vec{\nabla}T_s\right) + (1-\varphi)q_s''' + h(T_f - T_s) \tag{11}$$

$$\varphi(\rho C_p)_f \frac{\partial T_f}{\partial t} + (\rho C_p)_f \vec{v}\cdot\vec{\nabla}T_f = \varphi\vec{\nabla}\cdot\left(k_f\vec{\nabla}T_f\right) + \varphi q_f''' + h(T_s - T_f) \tag{12}$$

In the above equations, the subscripts s and f describe the solid matrix and fluid phase respectively. The specific heat of the solid is represented by the symbol C, similarly,

C_p represents the specific heat of the fluid at constant pressure. As usual k represents the thermal conductivity, and finally q''' is the heat generated per unit volume. It is important to recognize the term $(\rho C_p)_f \vec{v} \cdot \vec{\nabla} T_f$ in Equation 12, which describes the convective heat transfer of the fluid. On the right side of both equations is the term h, which is the heat transfer coefficient. The above equations are also commonly known as the two-equation energy model for porous media. When considering the use the two-equation model the correct determination of h becomes paramount.

2.6.10 Heat transfer coefficient

The heat transfer coefficient in Equations 11 and 12 can be determined by an empirical relationship, starting with Equation 13.

$$h = a_{fs} h^* \tag{13}$$

In the above equation a_{fs} represents the specific surface area defined by Equation 14, which is dependent on the geometric nature of the porous medium.

$$a_{fs} = \frac{Wetted\ surface\ area\ in\ REV}{Volume\ of\ REV} \tag{14}$$

According to Dixon and Cresswell the correct determination of h^* is based on a lumped parameter model defined by Stuke as given in Equation 15 [19].

$$\frac{1}{h^*} = \frac{1}{h_{fs}} + \frac{d_p}{\beta k_s} \tag{15}$$

In this equation β is a dimensionless constant, the value of which depends on the shape of the particle. The value of β equates to 10, 8, and 6 for spheres, cylinders, and slabs respectively [19]. Finally, in the above equation h_{fs} denotes the fluid to solid heat transfer coefficient, which is related to the fluid to solid Nusselt number by the relationship given by Equation 16.

$$Nu_{fs} = \frac{h_{fs} d_p}{k_f} \tag{16}$$

There have been many attempts at determining an empirical relationship for Nu_{fs}. Handley and Heggs had developed the relationship seen in Equation 17 [20].

$$Nu_{fs} = \frac{0.255}{\varphi} Pr^{1/3} Re_p^{2/3} \tag{17}$$

This equation correlates well with experimental data at particle Reynolds numbers above 100. An alternative to the above equation has been suggested by Wakao and Kaguei, seen in Equation 18[21].

$$Nu_{fs} = 2 + 1.1Pr^{1/3}Re_p^{0.6} \qquad (18)$$

Both above equations have the shortcoming of offering limited confidence at lower Reynolds numbers. Kothari has developed a relationship seen in Equation 19 that depends only on the Reynolds number [22].

$$Nu_{fs} = 0.033Re_p^{1.3} \qquad (19)$$

The above relationship is applicable in the lower Reynolds number range from approximately 1 to 100. It is therefore, recommended to use relationships offered by Handley and Heggs or Wakao and Kagei at higher Reynolds numbers flows and Kothari's equation at lower Reynolds number flows.

2.6.11 Concept of a Porous Jump

A Porous jump is a one-dimensional simplification to the porous media model, where the same equations are solved but the pressure drop occurs suddenly across a boundary. In such a case, the length of the porous medium is specified to determine the total pressure drop. Porous jumps are used whenever possible due to their simplicity; however, cannot be used to model pressure gradients or heat transfer within the porous medium.

2.7 Problem Statement and Research Objectives

In this thesis, a specific cooling tunnel configuration is modeled using porous media theory combined with computational fluid dynamics. An instrumented experimental tunnel is then constructed and tested to evaluate the numerical model. The configuration of the cooling tunnel investigated is shown in Figure 6. It consists of four pallets of agricultural product, two walls, one industrial vane axial fan, and a tarp. The entire configuration resides in a cool room kept at a temperature of 10°C .The pallets are separated into two groups of two pallets each with a gap equivalent to the width of one

pallet between them, forming a tunnel between the pallets. The fan causes a low pressure within the tunnel, pulling air through the boxes and over the produce. The solid walls and tarp restrict the airflow from entering in certain directions in order to pull cool air from the room through the openings in the sides of the product boxes into the tunnel, and finally out through the fan. The size of the produce boxes and stack layer configuration depend on the type of produce considered. This potentially introduces complex flow networks within each stacked layer of product. In the case of the large cucumbers considered initially, each box was 0.299m by 0.413m by 0.108m in size and contained 12 large cucumbers.
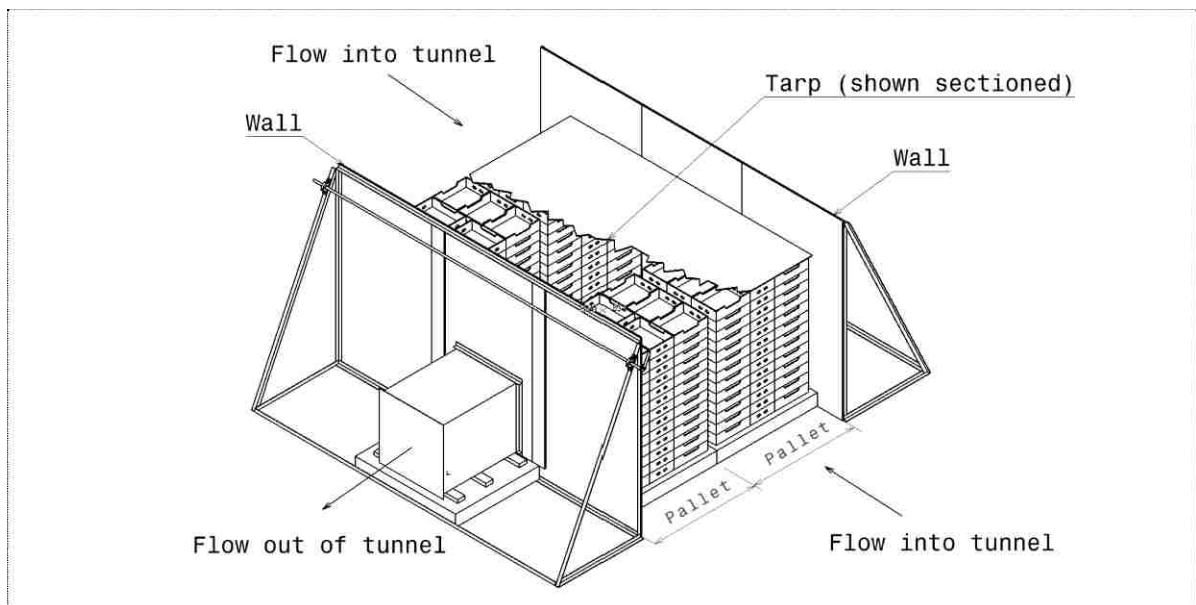
Figure 6: Tunnel Configuration [23]

The specific objectives of this study are to

1. develop a simple two dimensional numerical model for the approximation of the transient temperature variation of agricultural produce in a forced air cooling tunnel.
2. construct a cooling tunnel test facility and conduct full scale experiments to determine the validity of the assumptions made and the accuracy of the numerical model.

17

3. identify and investigate improvements to the numerical model
4. modify the constructed cooling tunnel test facility to investigate an alternate configuration.

2.8 Layout of the Remainder of the Thesis

Firstly, the details of the numerical model and its solution are described in Chapter 3. Results of the initial numerical solutions are presented and discussed in Chapter 4. This followed by a description of the experimental apparatus and procedures in Chapter 5 along with experimental results. Chapter 6 contains a description of a modified numerical model which includes adjustments made which are required to allow a fair comparison of the numerical and experimental results. The comparison of the two sets of data is presented in Chapter 7 and an investigation of the effects of air leakage given in Chapter 8. An alternate tunnel configuration is presented in Chapter 9. Also included is a comparison of the numerical and experimental results for that configuration along with a discussion on the relative performance of each configuration. Chapter 10 includes a discussion of the accuracy of all the numerical models. Conclusions and recommendations for future work are made in Chapter 11.

3. Numerical Methodology

 The numerical models are constructed and solved using commercially available computational fluid dynamic software; namely ANSYS Fluent 14. Details of flow assumptions, geometry, boundary and initial conditions, solution grid, and governing equations are presented in the following sections. All results have been computed using an Intel(R) Core™ i7 CPU x980@3.33GHz processor, equipped with 12 GB RAM, and a 64-bit operating system.

3.1 Flow Assumptions and Geometry

The first assumption made is that of incompressible flow. This notion is reasonable for the relatively low velocity magnitudes expected. Secondly, there is no flow between the layers of stacked produce. It is also assumed that there is little to no difference between the flow patterns in each respective layer of boxes. Although there is an obvious geometrical difference between the flow field in the horizontal plane of the top and bottom layers of boxes due to the location of the fan, it is anticipated (and later verified) that the pressure distribution is approximately uniform at the inlets and outlets of each stack of product. The benefit of such an assumption is the ability to use the simplified two-dimensional formulation, which greatly reduces computational cost. Lastly, it is assumed that there is a negligible difference in the flow patterns within the two respective groups of product stacks on either side of the tunnel space. This allows the use of a vertical symmetry plane through the center of the tunnel that essentially splits the tunnel and computational domain in half.

Preliminary experiments, the details of which can be found in Appendix B, indicate that the bulk of the flow resistance is due to the produce containers openings (vent-holes). The internal produce provides a smaller contribution to the flow resistances. It is also important to note that these resistances are dependent on the direction of flow (front to back or side to side) through the container, meaning the losses are anisotropic. Based on these findings, the product container vent-hole openings and contained produce are modeled using porous jumps, and anisotropic porous media respectively. The container opening shapes, number and location are different at the ends compared to the sides. In many cases when the boxes are arranged in layers to fit onto the pallet, the openings will

not coincide, essentially creating a wall. An example of when the container openings do not coincide can be seen in Figure 7. In the figure, blocked holes are represented with red areas, and unblocked holes as green areas. Each different type of agricultural product offered by the industrial partner is packaged in different containers, therefore; offering different layer arrangements.
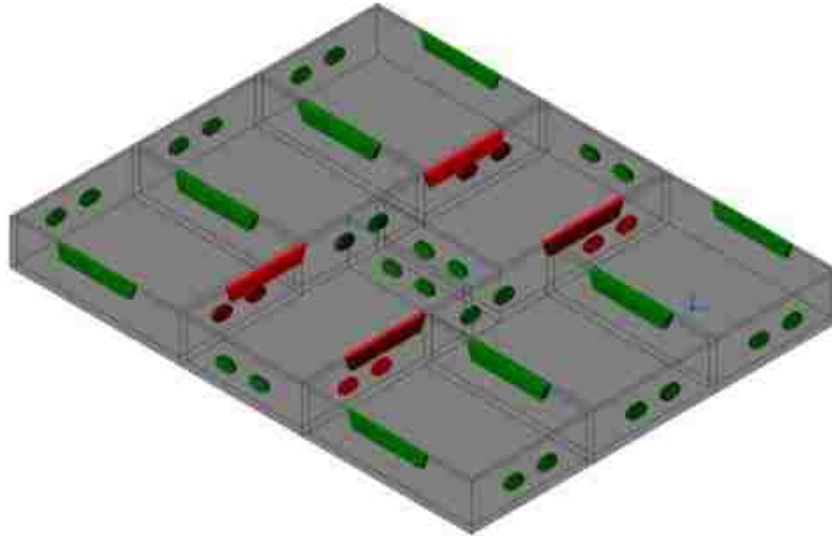
Figure 7: Container Opening Alignment

3.2 Boundary and Initial Conditions

Based on the flow assumptions, a 2-D flow field can be generated representing the pink area seen in Figure 8. The 2-D geometry and boundary conditions, for one layer of large cucumbers, can be visualized with the aid of Figure 9. In the figure, red lines and grey filled areas respectively represent the porous jumps and porous media. The porous media is assumed to be at a uniform initial temperature of 28℃. Walls are shown with black lines, with the simple boundary condition assumption of adiabatic walls with the no slip condition imposed. The blue line represents the pressure inlet assumed to be at standard atmospheric pressure with a constant temperature of 10℃. The zones not occupied by the produce contain air depicted as white filled areas. A velocity outlet is used to simulate the effect of the vane axial fan, which is illustrated as a green line. The magnitude of the velocity at the outlet is based on the total desired flow rate of air through all the boxes

filled with produce. Lastly, the yellow line indicates the plane of symmetry between the two groups of pallets.
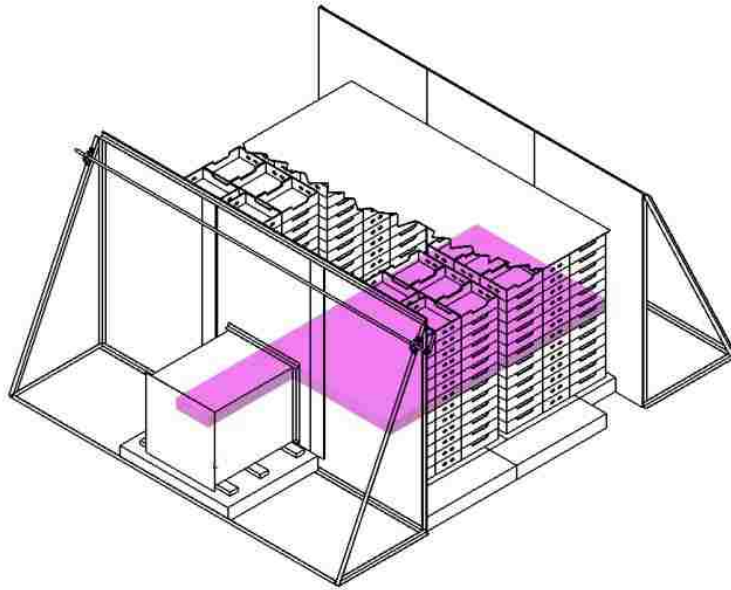
Figure 8: Resultant 2-D Flow Field
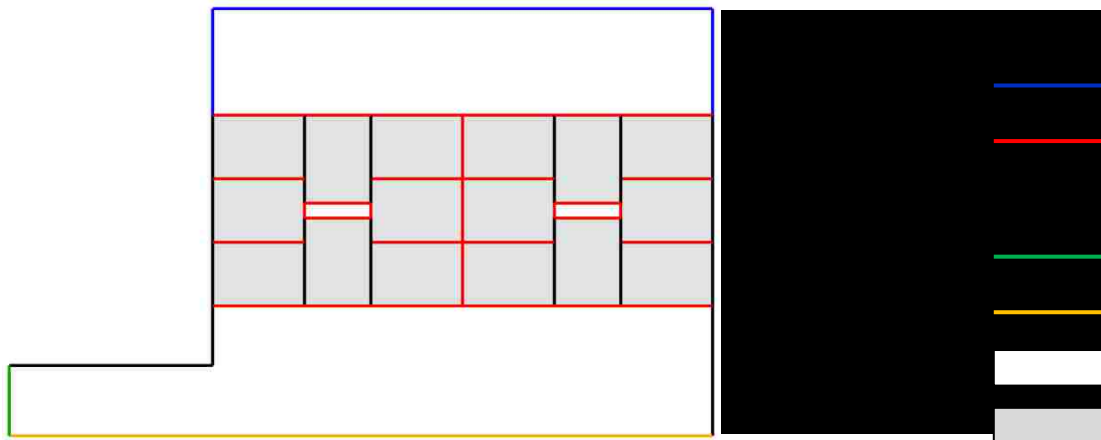
Figure 9: Initial Boundary Conditions

3.3 Solution Grid

A quadrilateral block structured format is implemented to mesh the flow domain as this gives accurate solutions near walls, and it requires less computational effort compared to other mesh types of the same spatial resolution. A dual cell mesh is employed within the

porous media zones in order to take advantage of the non-equilibrium thermal model. A coincident mesh must be created for both the solid matrix and fluid, on which the corresponding energy equation will be solved (recall Equations 18 and 19). This feature has been made available in ANSYS Fluent 14.0, released in December 2011.The material properties of the solid matrix and fluid must be specified within the model. The properties of the agricultural product were assumed to be those of water, since the produce considered is composed primarily of water [24]. Initially the solid matrix is assumed to be at a uniform temperature of 28℃. Figure 10 shows the numerical grid, generated using GAMBIT, and used in numerical calculations.
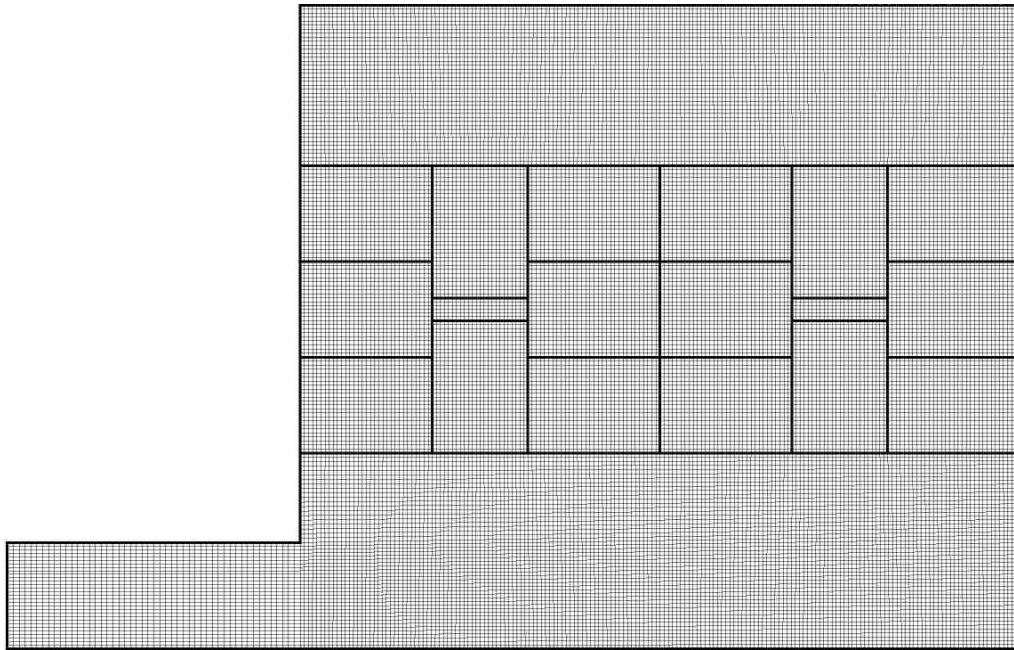
Figure 10: Mesh Generated with GAMBIT

3.4 Governing Equations

In order to simulate the transient temperature pattern within the porous medium, some parameters associated with the mathematical model need to be specified. A discussion of these parameters and the governing equations that are required to achieve an accurate simulation of the physical behavior of the produce cooling tunnel is given in this section.

3.4.1 Porosity

The numerical solution requires that the porosity of the medium be specified. In the specific case considered, the void volume is determined by subtracting the volume occupied by the produce from the total volume of the box. The volume occupied by the produce is manually determined based on the total weight of the product in each container and the specific weight of the produce. Knowing the void volume and total volume of the box the porosity can easily be specified with the use of Equation 2. In this specific case, the porosity is calculated to be 0.522.

3.4.2 Continuity

Within the ANSYS Fluent user guide, the continuity equation for a single-phase flow through porous media, with isotropic porosity, is defined using Equation 20.

$$\frac{\partial(\varphi\rho)}{\partial t} + \vec{\nabla} \cdot \left(\varphi\rho\vec{V}\right) = 0 \tag{20}$$

In the above equation, V represents the intrinsic average velocity, or the physical velocity. When the porosity is assumed constant with time and the Dupuit-Forchhiemer relationship (Equation 3) is employed, Equation 20 becomes equal to Equation 4.

3.4.3 Momentum

The standard linear momentum equation takes the form found below.

$$\frac{\partial}{\partial t}\left(\rho\vec{V}\right) + \vec{\nabla} \cdot \left(\rho\vec{V}\vec{V}\right) = -\vec{\nabla}p + \vec{\nabla} \cdot \left(\overline{\tau_s}\right) + \rho\vec{g} + \vec{F} \tag{21}$$

In the above equation, on the left hand side, the accumulation and convection terms $\frac{\partial}{\partial t}\left(\rho\vec{V}\right)$ and $\nabla \cdot \left(\rho\vec{V}\vec{V}\right)$ can be found respectively. The right hand side of the equation consists of, $\overline{\tau_s}$, the stress tensor, $\rho\vec{g}$, the gravitational body force, and $\vec{F}$, any other external body forces. The term $\vec{F}$ is used to include other model dependent source terms, including terms associated to the porous media model. When the model dependent source terms for porous media are included in Equation 21, it takes the form seen in Equation 22.

$$\frac{\partial}{\partial t}\left(\varphi\rho\vec{V}\right) + \vec{\nabla} \cdot \left(\varphi\rho\vec{V}\vec{V}\right) = -\varphi\vec{\nabla}p + \vec{\nabla} \cdot \left(\varphi\overline{\tau_s}\right) + \varphi\overline{B_f} - \left[\frac{\varphi^2\mu}{\overline{K}}\vec{V} + \frac{\varphi^3\overline{C_2}}{2}\rho\left|\vec{V}\right|\vec{V}\right] \tag{22}$$

In this equation $\overrightarrow{B_f}$ includes all body forces, including gravitational, and the last two terms within the square brackets represent the viscous and inertial drag forces caused by the pore walls. The porosity appears in Equations 20 and 22 to account for the fact that the fluid only occupies the volume of the pores while the model assumes that it fills the entire volume. The permeability, $\vec{K}$, and the Forchhiemer drag coefficient, $\overrightarrow{C_2}$, require empirical determination. The details of the experiment conducted to determine the porous medium empirical constants is presented in Appendix B. When the fluid flow is steady, the porous medium geometrically fixed, body forces are negligible and no macroscopic velocity gradients, Equation 22 reduces to a form consistent with Equation 9 [25]. In order for Equation 22 to reduce exactly to that of Equation 9 , $\overrightarrow{C_2}$ from Equation 22 would have to be equal to $2c_F/\sqrt{\vec{K}}$ from Equation 9.

The specified coefficients depend on the flow direction being in the long or short direction of the product container. For the case of the porous medium in the long direction (ie: flow through the short ends), the viscous resistance (K) and the inertial resistance (C_2) are $5.4 \times 10^{-7} m^2$ and $252.6 m^{-1}$ respectively. In the short direction (ie: flow through the long ends) of the product container the viscous resistance (K) and inertial resistance (C_2) of the porous medium are $-2.3 \times 10^{-7} m^2$ and $87.9 m^{-1}$ respectively. Although the viscous resistance is negative, which is unrealistic, the inertial resistance dominates, therefore; the combined behavior is that of a momentum sink. The porous jump coefficients are specified in the same manner. The porous jump coefficients (K and C_2) for the long and short directions are $4.2 \times 10^{-9} m^2$ and $7.4 \times 10^4 m^{-1}$ and $2.7 \times 10^{-8} m^2$ and $1.8 \times 10^4 m^{-1}$ respectively. In both cases the length of the porous jump is specified as $9mm$, which is the measured thickness of the cardboard container. Details of how the porous medium and porous jump coefficients are obtained can be found in Appendix B.

3.4.4 Energy and Heat Transfer

In order to simulate convective heat transfer from the solid agricultural product to air passing around it, the use of the non-equilibrium thermal model is required. The two-equation non-equilibrium energy equation takes the form found in Equations 23 and 24, for the solid and fluid phases respectively.

$$\frac{\partial}{\partial t}[(1-\varphi)\rho_s E_s] = \vec{\nabla}\cdot[(1-\varphi)k_s\vec{\nabla}T_s] + S_s^h + h^*a_{fs}(T_s - T_f) \tag{23}$$

$$\frac{\partial}{\partial t}(\varphi\rho_f E_f) + \vec{\nabla}\cdot[v(\rho_f E_f + p)] =$$

$$[\varphi k_f\vec{\nabla}T_f - (\sum_i h_i J_i) + (\vec{\tau}\cdot\vec{v})] + S_f^h + h^*a_{fs}(T_f - T_s) \tag{24}$$

In the above equations E denotes the total energy, and S^h represents the enthalpy source term, with the usual subscripts for the solid or fluid phase. In Equation 24, J_i represents the diffusion flux, and h_i represents the sensible enthalpy, of species i. The density of the solid, ρ_s, and the density of the fluid, ρ_f, are specified as 998.2 $kg\ /m^3$ and 1.225 $kg\ /m^3$ respectively. If one chooses to neglect enthalpy transport due to species diffusion, and any thermal energy created by viscous shear flow, Equations 23 and 24 become similar to Equations 11 and 12. When the incompressible flow assumption is applied, pressure work and kinetic energy within the total energy term become negligible, Equations 23 and 24 become equal to Equations 11 and 12 respectively.

The time variation of temperature within the porous medium, the appropriate empirical heat transfer model for each Reynolds number range needs careful attention for accurate simulation. The available relationships between the Nusselt number and the particle Reynolds number for Wakao and Kagei [21], Handley and Heggs [20] and Kothari [22] are graphically presented in Figure 11. In this figure, the intersection points of Kothari's correlation with the other two are calculated and plotted on the curve. The Reynolds Numbers at the points of intersection are found to be 80.5and 147.1 for the relationships offered by Handley and Heggs, and Wakao and Kagei respectively. Within this work, the relationships used are those of Kothari and Handley and Heggs for low and high Reynolds numbers respectively. The relationship given by Wakao and Kagei gives elevated Nusselt Number compared to that from Handley and Heggs from Figure 11. Therefore, the relationship given by Handley and Heggs is used, and the relationship given by Wakao and Kagei is not, since in general, the numerical models will be shown later to over predict the heat transfer.
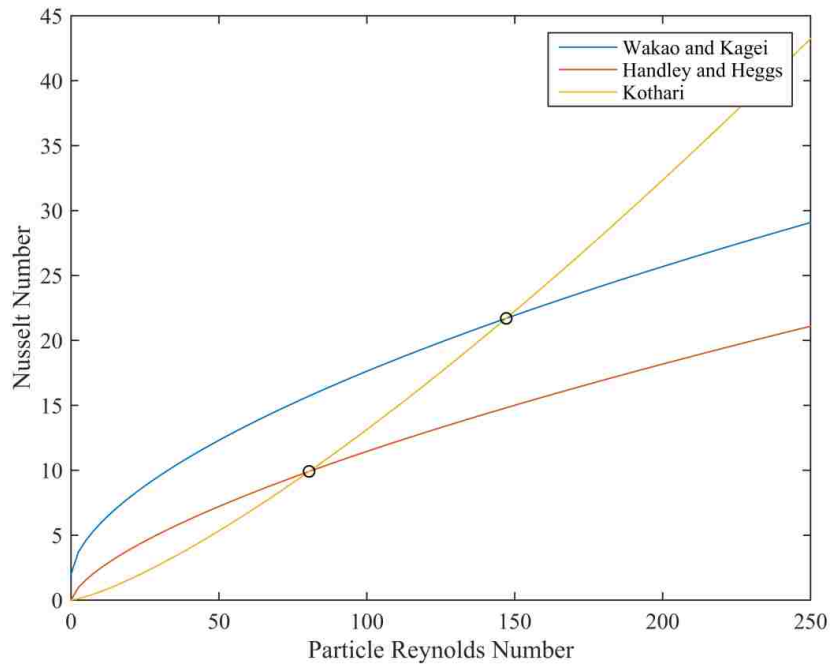
Figure 11: Nusselt Number Correlations with Particle Reynolds Number

3.5 Numerical Solution

The governing equations are solved sequentially using the pressure based segregated solver for each cell. The "SIMPLE" method is used for pressure velocity coupling. Pressure discretization is achieved using the standard method available in Fluent and the standard $k - \varepsilon$ model is used to model the turbulence. The default order of the discretization schemes are chosen as follows. Second order upwind schemes are used for momentum and energy while first order upwind schemes are used for turbulent kinetic energy and dissipation rate. Lastly, first order time advancement is used, with a time step size of 1 second (s), since time step sizes of one-half that amount gave essentially the same result and the overall computational time was of an acceptable value. It is believed that the default discretization orders offer a balance of numerical diffusion and dispersion. In general, first order methods offer lower computational cost at the expense of lower accuracy; however, solutions generated using all second order methods gave no noticeable difference in the results.

26

4. Numerical Results of the Initial Model

The initial numerical model is solved and the results are presented as follows. Firstly, the velocity and dimensionless vacuum pressure distributions throughout the flow field are considered followed by the 7/8 cooling time distribution. The time dependent dimensionless temperature is then investigated at locations that have the shortest and longest 7/8 cooling time. Finally, the temperature distribution throughout the entire flow field corresponding to that at the instant in time when the last point in the entire amount of agricultural product has reached the 7/8 cooling temperature is presented.

4.1 Non-dimensional Analysis

In the post processing of numerical and experimental results, normalization of some flow variables is implemented. The normalization technique used is a max-min type normalization within the range of 0 to 1 [26]. The standard equation for this type of technique is given in Equation 25.

$$x^* = \frac{x - x_{min}}{x_{max} - x_{min}} \qquad (25)$$

The static pressure and temperature are normalized using this technique. The static pressure is normalized in order to make more appropriate comparisons of the numerical and experimental models. In the case of the temperature of the produce the seven eights and half-cooling temperatures correspond to dimensionless temperatures of 0.125 and .5. This makes it easy to identify the seven eights and half cooling time on a plot of dimensionless temperature versus time. Normalization of other variables such as the velocity and heat transfer coefficient do not provide the same benefits and therefore, are not conducted.

4.2 Dimensionless Vacuum Pressure and Velocity Magnitude Distribution

Although the initialized values of pressure and velocity throughout the flow field are taken to be 0 Pa (gauge) and 0 m/s respectively, their values at the end of the first time step are already those of the steady state. This is due to the widely differing time scales of the flow and thermal characteristics because of the incompressible nature of the flow. These values remain constant throughout the remainder of the cooling period.

The computed dimensionless vacuum pressure,P^*, variation within the flow field is shown in Figure 12. In this equation the minimum pressure is standard atmospheric pressure (0 Pa gauge), and the maximum pressure is the maximum vacuum pressure (tunnel pressure gauge). The influence of the porous jumps can be seen to be dominant since the pressures within each box are relatively uniform. The variation of the pressures in the boxes with their long dimension vertical (henceforth referred to as "vertically oriented") compared to those with their long dimension horizontal (henceforth referred to as horizontally orientated) is due to the difference in the porous jump coefficients, and the influence of the air space in the center of each pallet.

$$P^* = \frac{P - P_{min}}{P_{max} - P_{min}} \tag{26}$$
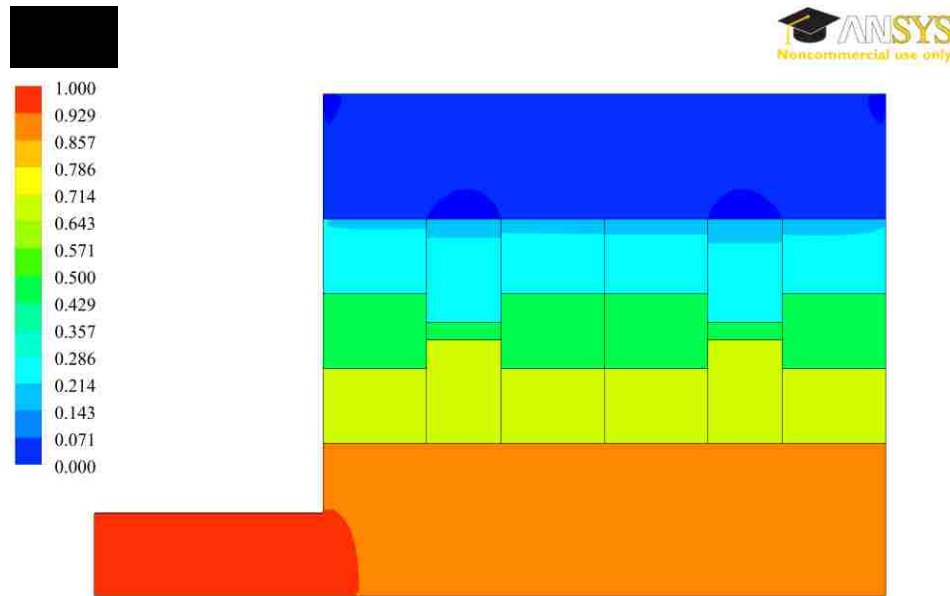
Figure 12: Contours of Dimensionless Vacuum Pressure from the Initial Solution

The small pressure variation in the tunnel region is not apparent in Figure 12 due to its relatively low variation in magnitude compared to that seen across the boxes of produce. The pressure variation within the tunnel portion of the flow field is clearer in Figure 13. From these results, it can be seen that the variation of the pressure acting on the boxes is relatively low (less than 5% difference). The minimum pressure of -138 gauge occurs at the region of separation where the fluid is flowing around a sharp edge into the fan.
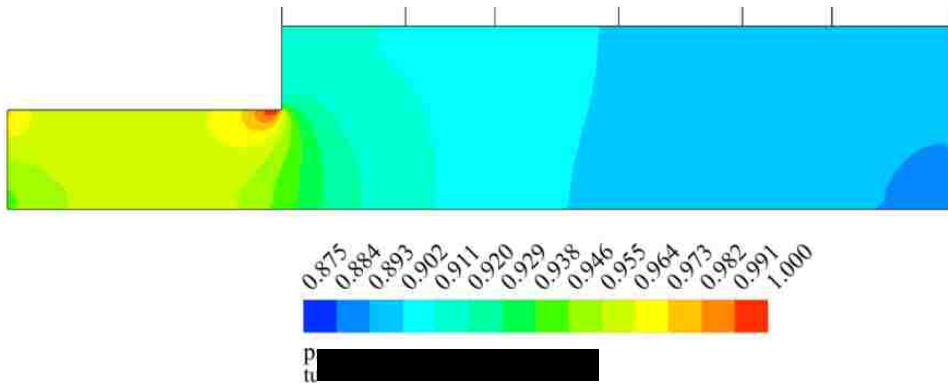
Figure 13: Contours of Dimensionless Vacuum Pressure in the Tunnel Region from Initial Solution

Results for the contours of the velocity magnitude are presented in Figure 14. It is important to note that these contours represent the magnitude of the superficial velocity within the region of the produce boxes. These velocities are consistent with the static pressure variation. The area weighted average velocity of the horizontally and vertically oriented boxes are used to calculate the heat transfer coefficient used in the transient simulation. A sample of these calculations can be found in Appendix C.
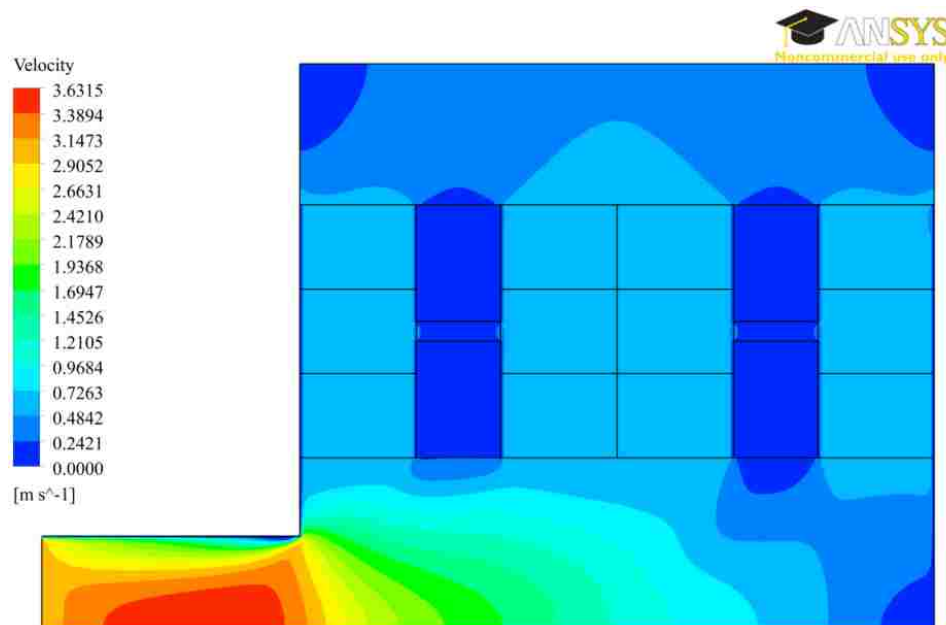
Figure 14: Velocity Magnitude Contours from the Initial Solution

4.3 7/8 Cooling Time Distribution

The 7/8 cooling time distribution within the product containers can be seen in Figure 15 with the time expressed in seconds. Contours of the 7/8 cooling time are obtained using the User Defined Function (UDF) capability of the ANSYS Fluent package. The UDF includes a logical statement used to record the current time step unless the cell is 7/8 cool. Once all cells are 7/8 cool, subsequent time steps do not alter the 7/8 cooling time distribution since no further data will be recorded. Details of the UDF used can be found in Appendix D.

The effect of the variation of the superficial velocity in the vertically oriented boxes, compared to that of the horizontally oriented boxes, is clearly seen. Since the superficial velocity is larger in the horizontally oriented boxes, they have lower cooling times. Conversely, the vertically oriented boxes have larger cooling times due to lower superficial velocities. It is also important to note that the produce located further from the tunnel section cools faster. This is because the cool air enters those boxes first and the enclosed produce rejects heat into the cooling air increasing its temperature, which then travels into the boxes close to the tunnel. This yields reduced heat transfer to those boxes of product.

The longest 7/8 cooling time was determined to be 18480 seconds (5.13 hours), which occurs at the outlet of the vertically oriented boxes nearest to the cooling tunnel. The shortest cooling time is estimated to be 3960 seconds (1.1 hours), and is located at the inlet of the horizontally oriented boxed closest to the cool incoming surrounding air.
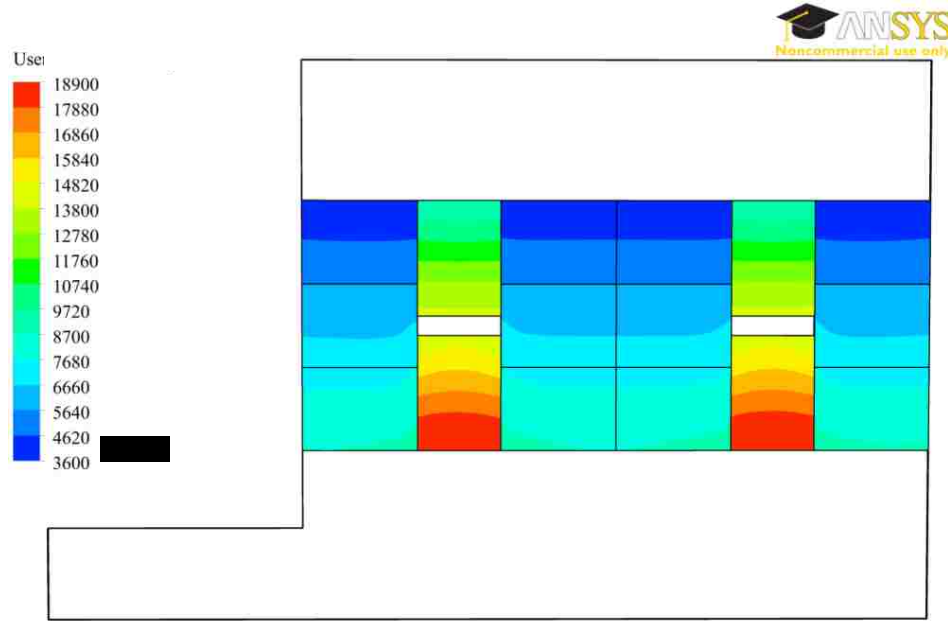
Figure 15: Seven Eights Cooling Time Distribution

4.4 Tunnel Minimum and Maximum 7/8 Cooling Times

The dimensionless produce temperature versus time corresponding to the region of minimum and maximum 7/8 cooling time can be seen in Figure 16. The dimensionless temperature is defined in Equation 27.

$$\tau = \frac{T(t) - T_r}{T_i - T_r} \tag{27}$$

The dimensionless temperature τ, is calculated knowing the instantaneous temperature $T(t)$, initial temperature T_i, and final temperature T_r. In this simple case, the final temperature is the same as the constant room temperature.
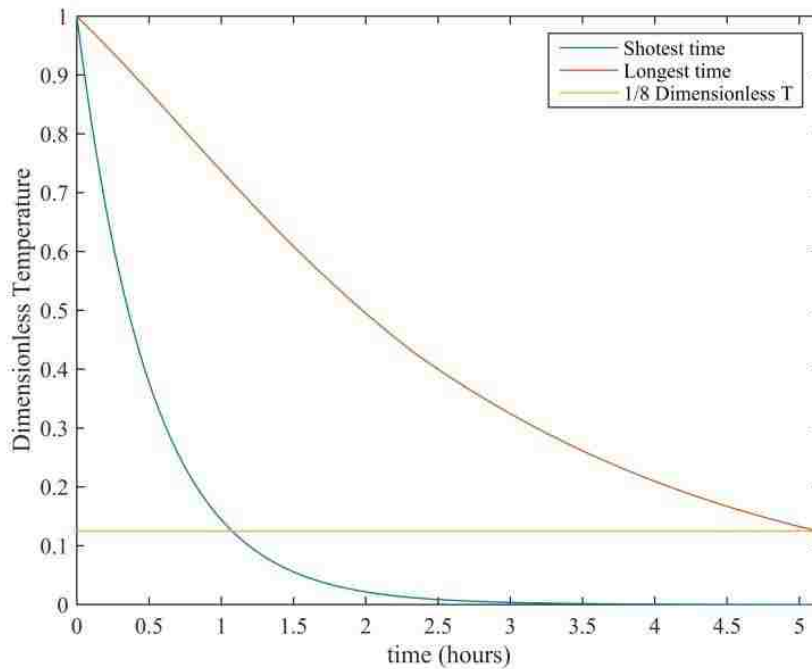
Figure 16: Limits of Product Temperatures

The shortest time case is important since it indicates the largest rate of heat rejection from the produce. Excessively high rates could potentially result in damage to the agricultural product. The longest cooling time is important as well, since it indicates how long the cooling tunnel is required to run. All other points in the flow field fall between the curves for shortest and longest cooling times.

4.5 Product Temperature Distribution at End of Cooling

Contours of the dimensionless temperature within the produce at the largest 7/8 cooling time are shown in Figure 17. The variation of the dimensionless temperature in Figure 17 is from fully cool to seven eights cool, with corresponding values of 0 and 0.125 respectively. This figure is helpful to see which areas are fully cooled to the surrounding room temperature once all the produce is at least 7/8 cool. From the figure, it can be seen that the horizontally oriented boxes are almost all fully cooled by the time all the produce is 7/8 cool.
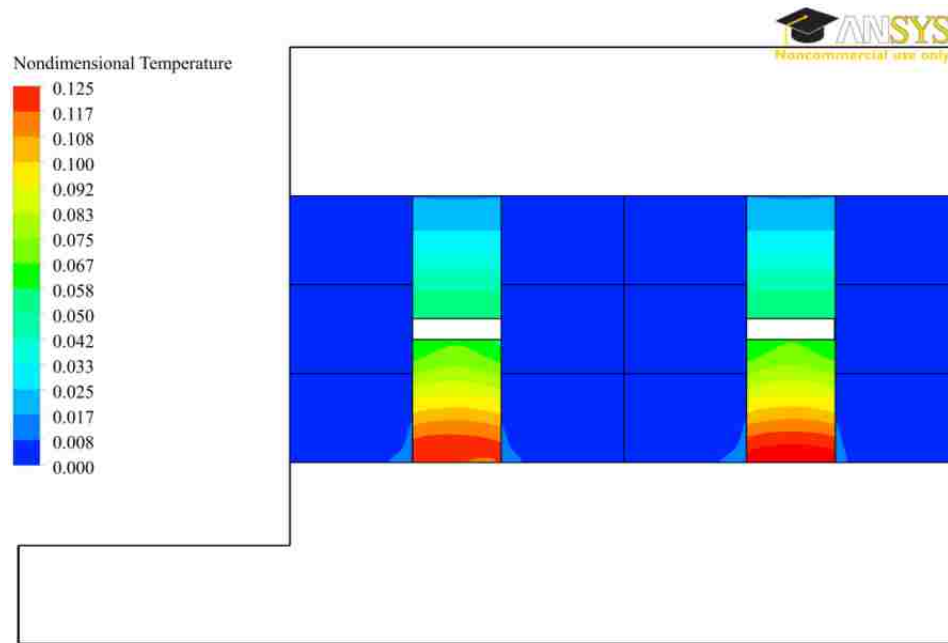
Figure 17: Dimensionless Temperature Contours in Produce When All Produce is at Least 7/8 Cool

4.6 Summary and Discussion of Initial Model Simulation Results

The initial 2D numerical model, with symmetric flow, no flow between layers, uniform initial temperature, and constant room temperature using the porous medium approach has successfully been implemented using typical values for the initial and boundary conditions. The simulations are valuable in identifying zones of fast and slow cooling and in characterizing the homogeneity of the process. In spite of the simplifying assumptions and approximations, the model yields reasonable results compared to cooling times seen in industry [4].The numerical results are verified to be consistent with the porous medium and jump coefficients supplied to the computational software.

5. Experimental Study

In order to validate the numerical model, full-scale experiments are performed. The experiments are conducted at the industry partner's facility during production hours within a cool storage room. The experiments allow for an evaluation of the numerical model to determine areas requiring improvements.

5.1 Experimental Facility

The experimental facility consists of four pallets each having 13 layers of boxes containing field heated agricultural product as previously depicted in Figure 6. The air is restricted to enter only the outer face of the pallets by using two self-standing portable walls in the front and back, and a tarp on top. Foam seals are used between pallets and boxes in order to reduce air bypass (short-circuiting). In order to pull the air through the pallets, a 24-inch diameter, direct drive, 8-blade cast aluminum propeller, Twin City WPD-24-E8-24 vane axial fan is mounted to the front wall. The back wall is equipped with a bypass door in order to have control over the negative (vacuum) pressure of the tunnel. Details on the fan selection and drawings of the prototype cooling tunnel can be found in Appendix E.

The test produce used in the experiments consisted of medium size cucumbers because they were the only agricultural product with sufficient quantity and field heat available during the time allocated for testing. A picture of the experimental setup is presented in Figure 18. The visible pallets in the figure are referred to as the right pallets, while the other pallets (on the far side) are referred to as left pallets. The pallets on each side are numbered with pallet 1 being closest to the fan side of the cooling tunnel, and pallet 2 being further from the fan side.

Figure 18: Experimental Facility

The experiments are performed in a large cooling room located within the production facility of the industrial partner. The cooling room is 21.5m long, 11m wide and 5m tall. The room is kept at the desired holding temperature with four refrigeration units, also seen in Figure 18.

5.2 Product Configuration

It is important to note that the arrangement for medium cucumbers is not the same as the arrangement for large cucumbers seen in the initial numerical investigation. The size of the medium cucumber box is 0.283m by 0.384m by 0.108m and contains approximately 12 medium cucumbers. The 13 layers of boxes in each pallet are configured in the same pattern, each of which contained 10 boxes of medium cucumbers. Figure 19 depicts the box configuration for each layer used in the medium cucumber case.
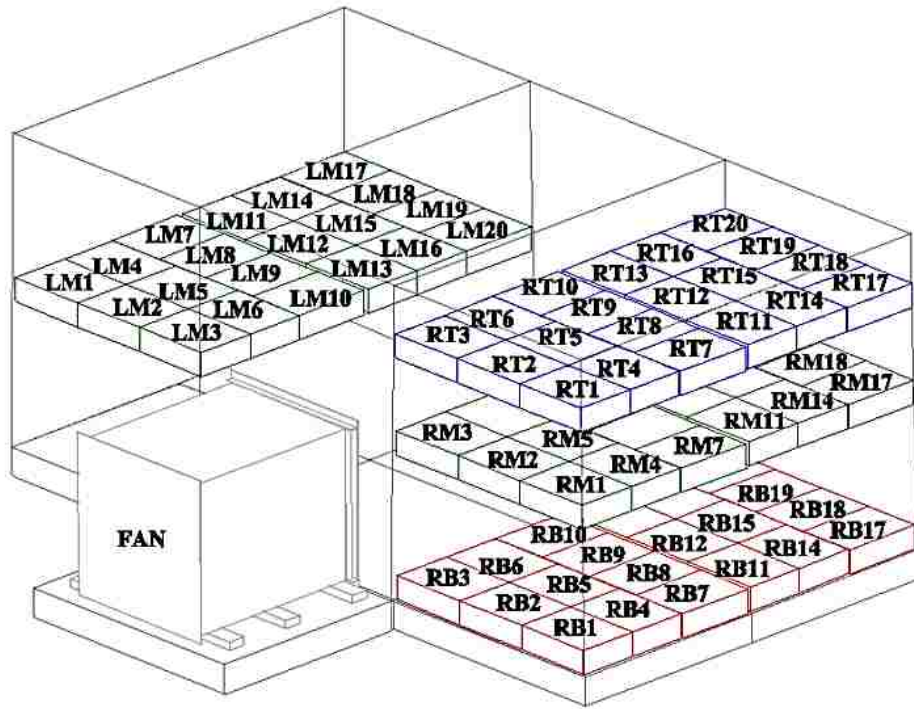
Figure 19: Medium Cucumber Box Indexing Arrangement

In order to organize the experimental data in a way that is consistent, a numbering system is developed. This indexing system is useful in order to understand which box in the flow field is being considered. A perspective view showing the numbering system used in this work can be seen in Figure 19. The boxes in each layer are numbered from 1 to the maximum number of boxes on each side of the cooling tunnel. The box index begins with the letter R or L depending on whether it is on the right or left side respectively. Following the side identification character is the layer identification character. The layer identification character will be T, M, or B indexing the top, middle, or bottom layer respectively. Within this work, the top layer corresponds to the layer of boxes located 3 boxes from the top of the pallet of stacked product. The middle layer corresponds to the layer of boxes located 7 boxes down from the top of the stack. Finally, the bottom layer is located on the bottom of the stack.

5.3 Experimental Equipment

The temperatures of certain representative cucumbers, which will be explained later, are measured using 32 Type T thermocouples connected to a desktop computer through a data acquisition system. The data acquisition system used is a Measurement Computing

24-bit, isolated, high channel count multifunction DAQ module (USB-2416), coupled with an analog input expansion module (USB-EXP32). The room relative humidity is also monitored using a Honeywell HIH-4021-003 humidity sensor. The humidity sensor is also connected to a separate identical multifunction DAQ. Pressures are measured using a handheld electronic manometer (Omega Model HHP-103), and recorded manually.

5.4 Data Acquisition

The multifunction DAQ is situated in the cold room and connected to computer via USB. National Instruments data acquisition software (LabVIEW) is used to record all data. The analog input data from the DAQ is converted into the desired units and saved on a 5 second interval. LabVIEW is also used in order to be able to monitor the temperatures in real-time. Details of the virtual instruments used in this work is contained in Appendix F.

5.5 Instrumentation Procedure

Instrumentation of boxes during the production process (original loading of the boxes and pallets) is not possible, as it would slow down production. Pallets of medium cucumbers, stacked in the appropriate arrangement ready for shipment, are then arranged in the cooling room in the desired cooling tunnel configuration. Partial disassembly of the stacks is required in order to instrument the boxes. Each of the pallets requiring instrumentation is disassembled to the bottom layer to be instrumented with the required thermocouples and Tygon® tubing as needed. For temperature measurement, the thermocouples are either placed under the plastic protective layer on the cucumber for surface temperature measurement, or inserted into the middle of the cucumber by puncturing the cucumber with the thermocouple, for core temperature measurement. Locations RM12, RM15, and RM20 (see Figure 19) are instrumented with both core and surface mounted thermocouples. The room is also instrumented with a thermocouple. Tygon® tubing ends are situated in the boxes in regions of low air velocity so that an accurate pressure measurement can be taken. Pressures are recorded in the boxes located in the right middle layer (RM) locations mostly, but are also placed in locations LM20, RT2, and RB20 in order to evaluate assumptions made in the numerical model. The

pallets are then rebuilt to original configuration from the bottom up with included instrumentation as required.

5.6 Experimental Procedure

Once the boxes are instrumented, the tarp is pulled over the top of the pallets, and the foam installed to achieve a good seal. The axial fan is then started which produces a vacuum pressure in the tunnel. The desired vacuum tunnel pressure is achieved by adjusting the bypass door on the back wall of the tunnel. The value is then recorded and the data acquisition system started in order to collect the data. Pressure readings are manually recorded for the boxes instrumented with Tygon® tubes. These pressure readings are taken at approximately 60 minute intervals to ensure that the flow conditions remain constant.

It is important to mention that, in some cases, the overall testing time was restricted because that testing was performed during the industrial partner's normal production hours. It is also important to note that during the testing period forklifts and personnel were sometimes actively present in the cooling room, which may have a minor effect on the results.

5.7 Experimental Results

In the following section, results from the full-scale experiment are presented. First, the initial core temperatures are considered. Recorded pressures are presented in their dimensionless form. Finally, results for the time dependent dimensionless core temperatures and room temperature are shown.

5.7.1 Initial Core Temperatures

The initial core temperatures of the produce for the middle layer are given in Figure 20. The boxes are colored such that the warmer boxes are red (25℃) and the colder boxes are blue (14℃). It is evident that there is a significant variation in the initial product temperature. The maximum temperature difference between boxes is found to be 9℃. It can also be seen that there is a large initial temperature variation within containers 11-20, whereas; in containers 1-10 the temperature variation is much smaller. There is also a noticeable difference in the initial temperatures of products of similarly located boxes on opposing sides of the tunnel; for example RM2 and LM2. This reflects the variation that

can occur in a production environment as opposed to more controller laboratory setting. It is clear that the assumption made of uniform initial temperature that is made in the initial numerical model is not valid.
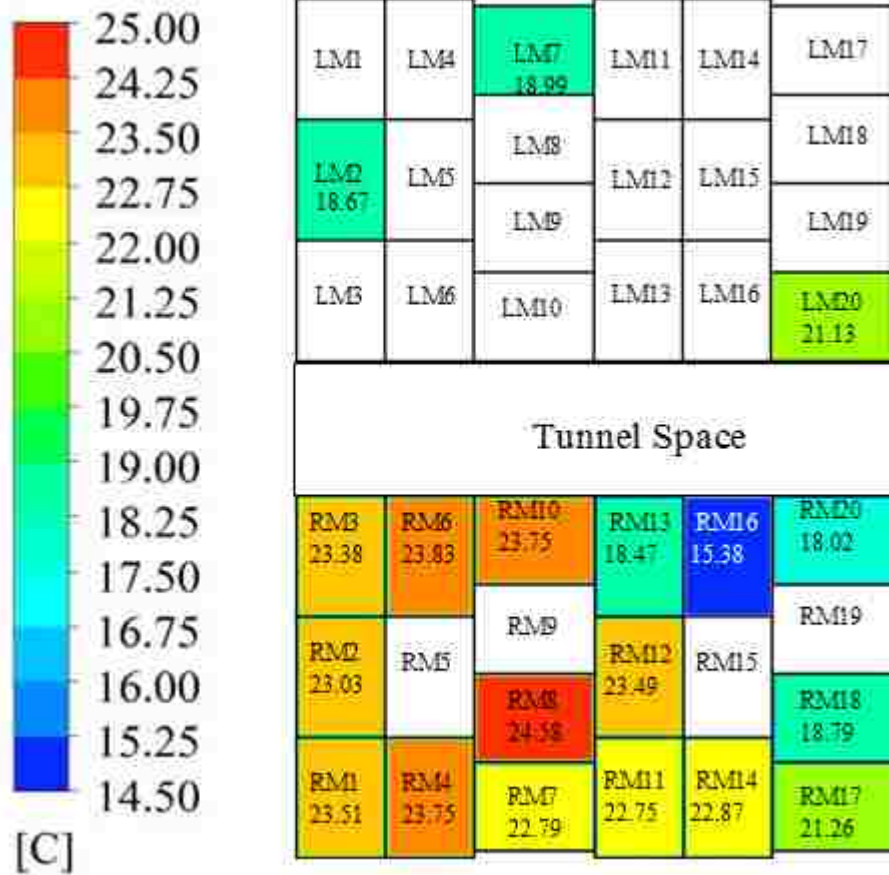
Figure 20: Initial Temperature Distribution in Middle Layer

The variation in initial core temperatures of the top and bottom layers can be seen in Figure 21. Again, there is a smaller variation in containers 1-10 than in containers 11-20 when considering boxes of similar locations.
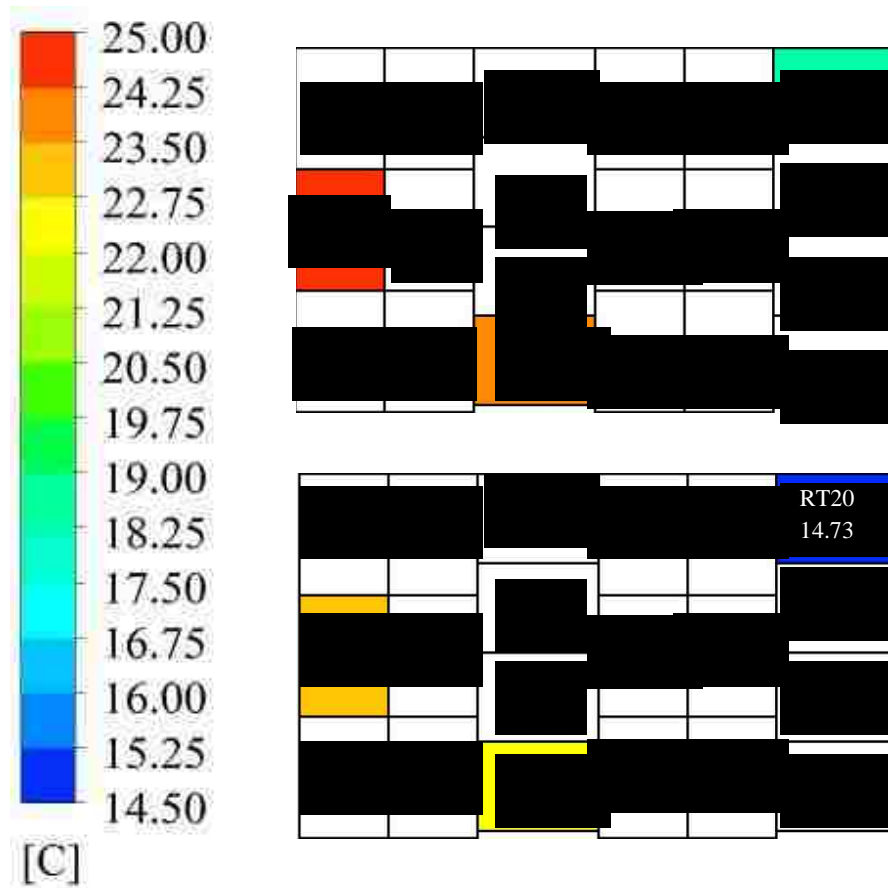
Figure 21: Initial Temperature Distribution in Bottom and Top Layers

Because of the variation of initial core temperatures throughout the pallets, only the temperatures measurements taken in boxes RM1 to RM10 will be considered for comparison with the numerical transient temperature results. The larger temperature variation throughout the other produce should not influence the temperatures in the layer considered, since the openings in the boxes that are in contact between the two pallets are not aligned, similar to what is seen in Figure 7. There should therefore, be no airflow from containers 1-10 to 11-20 or vice versa.

5.7.2 Average Dimensionless Vacuum Pressures

The average dimensionless vacuum pressure values for each box in the middle layer of the right pallet are depicted in Figure 22. In this case the minimum pressure is the atmospheric pressure of 0 Pa gauge and the maximum vacuum pressure is defined as the tunnel pressure of -113 Pa gauge. The pressures are observed to be lower in boxes closer to the tunnel side and, as expected, tend to increase toward the cold room side. To

40

investigate the variation in pressure in the different layers and on the different sides, the dimensionless pressures are calculated for boxes LM20, RT2, and RB20. They are found to be 0.91, 0.87, and 0.95 respectively. When comparing these dimensionless vacuum pressures with those located in similar locations in the middle right plane depicted in Figure 22, it is observed that the differences are less than 7%. For this reason, it can be concluded that the assumptions of symmetry and no variations between layers are reasonably valid.
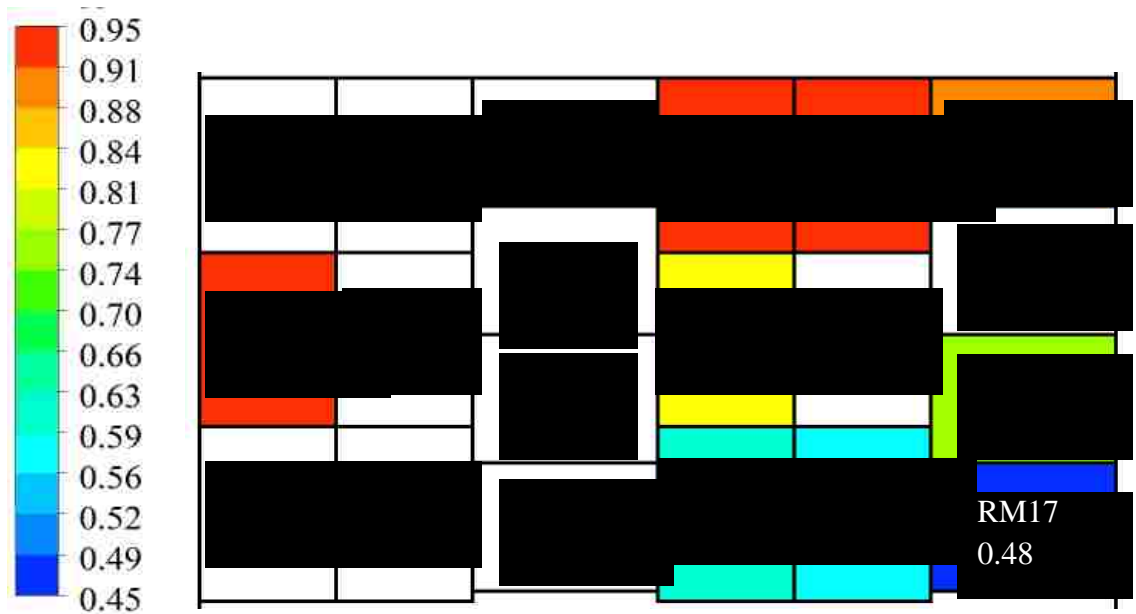
Figure 22: Experimental Dimensionless Vacuum Pressures in the Middle Layer of Boxes on the Right Side of the Tunnel

5.7.3 Time Dependent Dimensionless Core Temperatures

The time dependent dimensionless core temperatures of the cucumbers in boxes RM1 to RM10 are presented in Figure 23. It should be noted that boxes RM5 and RM9 not instrumented. These cooling curve trends are quite similar to those predicted in the initial numerical study as shown in Figure 2. The dimensionless temperature corresponding to 7/8 and 1/2 cool are 0.125 and 0.5 respectively. From the figure of the experimental values of dimensionless temperatures, it becomes clear that not all boxes in the experiment have reached the 7/8 cooling temperature criteria. This is because the tunnel did not run for a sufficiently long time due to the limitation of the operating hours of

industrial partner's facility. As a result, only comparisons of the half-cooling times of the numerical and experimental results are made.
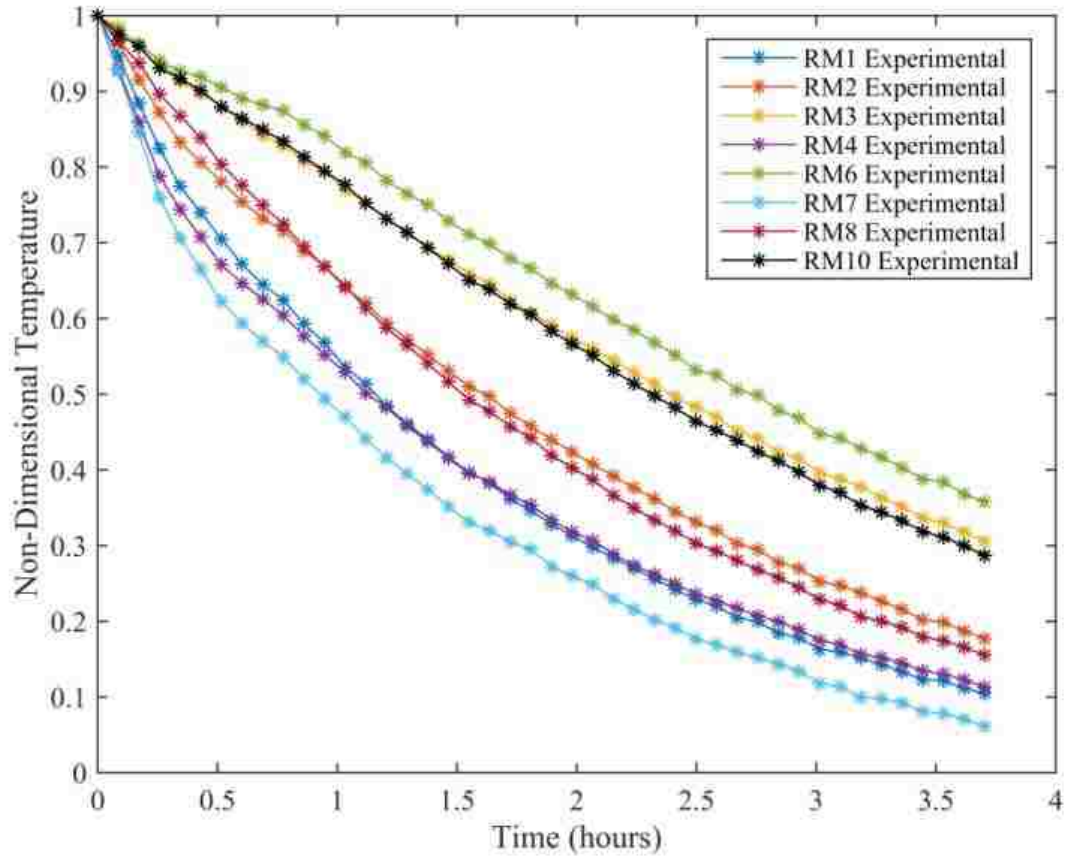
Figure 23: Experimental Dimensionless Temperatures

5.7.4 Time Dependent Room Temperature

The room temperature as monitored during the experiment can be seen in Figure 24. The room temperature rises initially and then, after some time, comes back down. The room temperature increased because the refrigeration units could not adequately reject the heat provided to the room by the cooling tunnel. As the agricultural product cools, the cooling tunnel provides less heat to the room and the refrigeration unit is capable of sustaining a constant room temperature. It is believed that the two large sudden spikes in temperature evident in Figure 24, are a result of an accidental handling of the thermocouple and do not reflect actual changes in the room temperature. These results indicate that the assumption of constant room temperature is not valid. In cases such as this, the term

42

T_r used to determine the dimensionless temperature in Equation 27 is taken to be the lowest measured temperature of the room
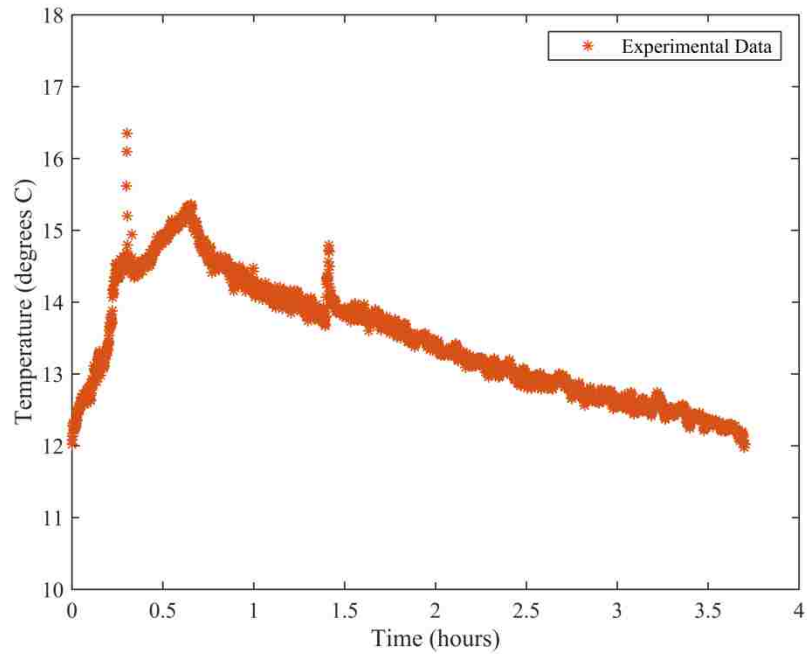
Figure 24: Experimental Room Temperature

5.8 Summary of Experimental Study

From the experimental results, it is observed that the initial core temperatures of the produce in separate containers are non-uniform, contrary to the assumption made in the numerical model. The results for the dimensionless vacuum pressure are found to support the assumption of no flow between layers and symmetric flow about the centerline of the cooling tunnel. The pressure difference between similarly located containers was a maximum of 7%. The uncertainty in the dimensionless vacuum pressures, measured during the experiment, are determined to range from ±6.9% to ±8.8% for measured pressures of -0.218 inches of water (-54 Pa), and -0.455 inches of water (-113 Pa) respectively. Details of the uncertainty calculations can be found in Appendix G. The transient dimensionless temperatures of the products are observed to behave similarly to what is expected from reports of industrial applications [4]. The assumption of constant room temperature is also determined to be invalid, as the room temperature changes significantly with time. In order to make a fair comparison of the numerical and

43

experimental results, modification of the numerical model is required to take into account the incorrect initial assumptions made in that model.

6. Modified Numerical Model

From the results of the full scale cooling tunnel experiments, the numerical model requires modification to the, mesh, boundary conditions, initial conditions, and zone conditions. Most of these modifications are accomplished by enhancing the functionality of the compiled UDFs.

6.1 Modified Mesh

The numerical grid requires modification since the pallets in the original numerical model contained large cucumbers, while in the full-scale experiments they contained medium cucumbers. Since each agricultural product has specific container dimensions, the layout of a single layer differs from one agricultural product to another. The porous medium and porous jump coefficients also required adjustment. The Modified numerical grid is generated using GAMBIT meshing software and can be seen in Figure 25.
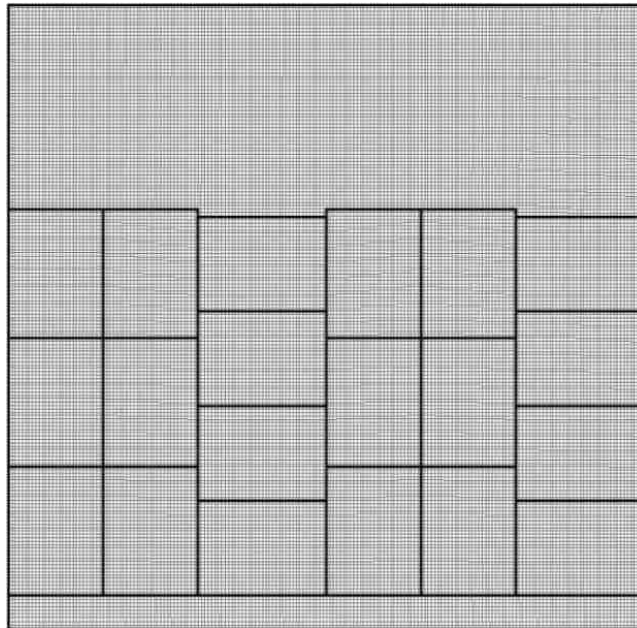

Figure 25: Modified Numerical Mesh

6.2 Modified Boundary Conditions

From the initial numerical results, it is observed that the pressure does not vary significantly in the tunnel portion of the cooling tunnel. For this reason, a pressure outlet boundary condition is used instead of the original velocity outlet condition. The modified boundary conditions are shown in Figure 26. The required changes are applied to the porous medium and jump coefficients. The viscous and inertial resistances for the porous region in the long direction are $4.8 \times 10^{-7}\ m^2$ and 170.7 respectively. In the short direction of the product container the viscous and inertial resistances of the porous medium are $1.5 \times 10^{-6}\ m^2$ and $63.8 m^{-1}$ respectively. The porous jump coefficients are specified in the same manner. The porous jump coefficients for the long and short directions are $3.9 \times 10^{-9} m^2$ and $5.7 \times 10^4\ m^{-1}$ and $1.8 \times 10^{-8}\ m^2$ and $2.8 \times 10^4\ m^{-1}$ respectively. In both cases, the length of the porous jump is specified to be $9 mm$. These restructured boundary conditions not only eliminate some unnecessary mesh points in the numerical solution, but also allow for the implementation of a pressure boundary set to be consistent with the tunnel pressures measured during experiments.
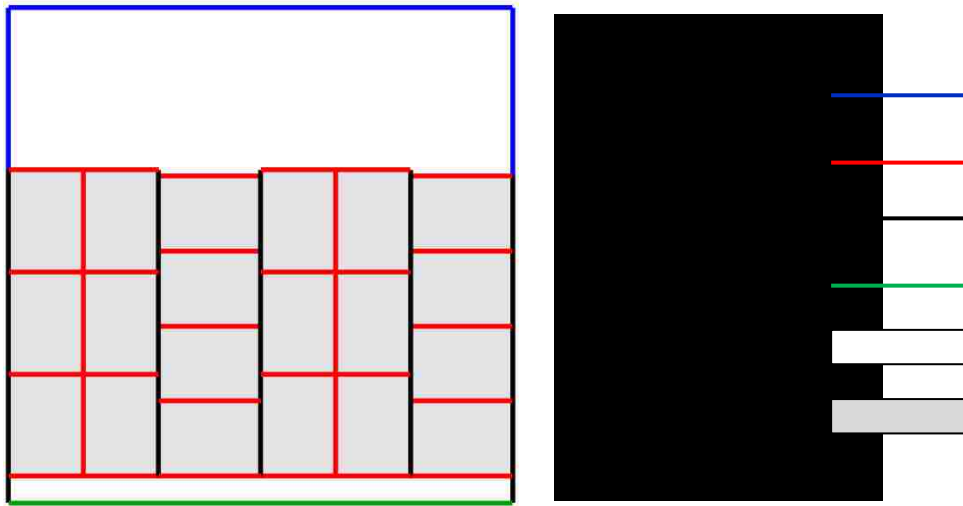

Figure 26: Modified Boundary Conditions

6.3 Modified Initial Conditions

From the initial produce temperature distribution observed in the experiment, the uniform initial temperature assumption made in the original numerical model is inconsistent. In order to regain consistency with experiments it is necessary to initialize the product

temperatures in each box to the temperatures observed in the experiment. In the boxes where the temperatures are not measured, the average temperature of the box above and below the box in question is used. This strategy is implemented with a UDF, the details of which can be found in Appendix H.

6.4 Modified Cool Room and Zone Conditions

In the original numerical model, the temperature of the room is assumed constant. From the results of the experiment, it is observed that the temperature in the room does not remain constant. In order to make a direct comparison between the numerical model and the experiments, it is necessary to model the transient room temperature. An expression for the time dependent room temperature is obtained using a Fourier series approximation, and is implemented with a UDF for the cold room zone. This allows the cold room zone temperature to match that of the experimental data. The details of the UDF used to achieve this is described in Appendix I.

More advanced UDFs have been generated to determine the heat transfer coefficient, seven eights cooling times and half-cooling times in the solid porous zones (produce). Details of the UDFs to determine the heat transfer coefficient and cooling times are given in Appendix J and Appendix K respectively.

Although not a result of the numerical solution, the room temperature versus time from the experimental and numerical investigation can be seen plotted in Figure 27. It is clear that the UDF with Fourier series approximation accurately simulates the room temperature conditions found during the experiment. The figure serves as a check to ensure that the UDF properly defines the cold room zone temperature, which is critical to the proper comparison with the numerical and experimental results.
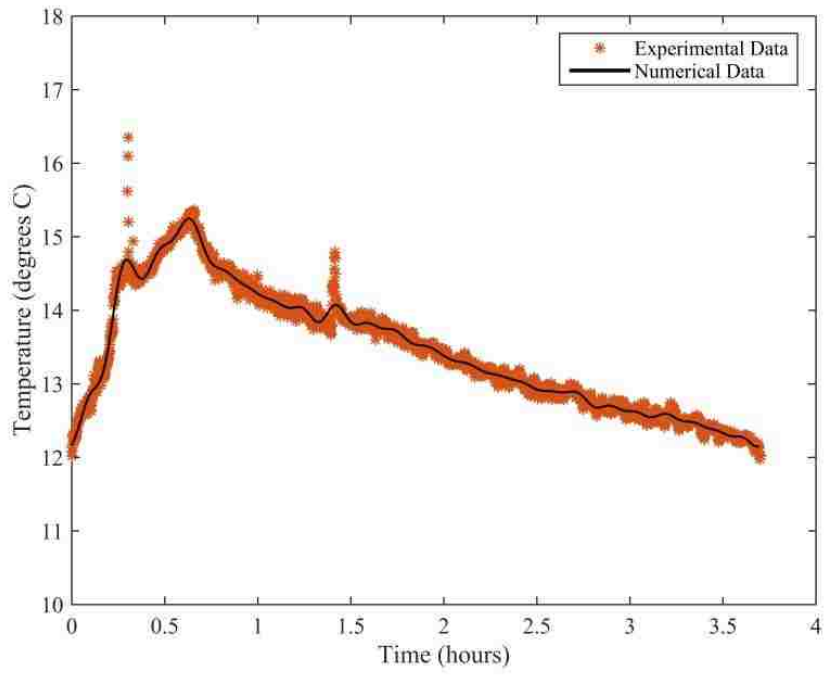
Figure 27: Transient Room Temperature

7. Modified Numerical Model and Experimental Result Comparison

To evaluate the validity of the numerical model, comparison with the experimental results is necessary. In the following sections, the numerical results (from the modified model) for pressure, time dependent temperature, and half-cooling time for each box are compared to the full scale experimental results.

7.1 Percent Difference

 The percent difference is used to determine the relative agreement between the numerical and experimental results. Within this work, the percent difference is defined as the difference between the experimental and numerical values divided by the maximum possible difference as indicated in Equation 28.

$$\% \ difference = \frac{experimental - numerical}{maximum \ possible \ difference} \tag{28}$$

As an example, consider the calculation of the percent difference of the non-dimensional temperature found in Equation 29.

$$\% \ difference \ in \ \tau = \frac{\frac{T_{exp}-T_r}{T_i-T_r} - \frac{T_{num}-T_r}{T_i-T_r}}{\frac{T_i-T_r}{T_i-T_r}} \tag{29}$$

In the case of temperature, the maximum possible difference is the initial difference between the produce and the room. Similarly, in the case of dimensionless vacuum pressure, the maximum possible difference is the difference between the room pressure and the tunnel pressure.

7.2 Dimensionless Pressure Comparisons

In order to compare the pressures, the area weighted average value of the numerical dimensionless vacuum pressure of the product in the containers is compared to the measured average dimensionless vacuum pressure for the corresponding experimental container. A comparison of the dimensionless vacuum pressures is presented in Figure 28. It is seen that the numerical and experimental results are not in good agreement. The maximum and minimum percent difference between the two data sets are 41% and 6% respectively. It can also be seen that the boxes situated closer to the tunnel section are in

48

better agreement than boxes closer to the cold room side. The maximum and minimum percent differences occur at locations RM2 and RM20 respectively.
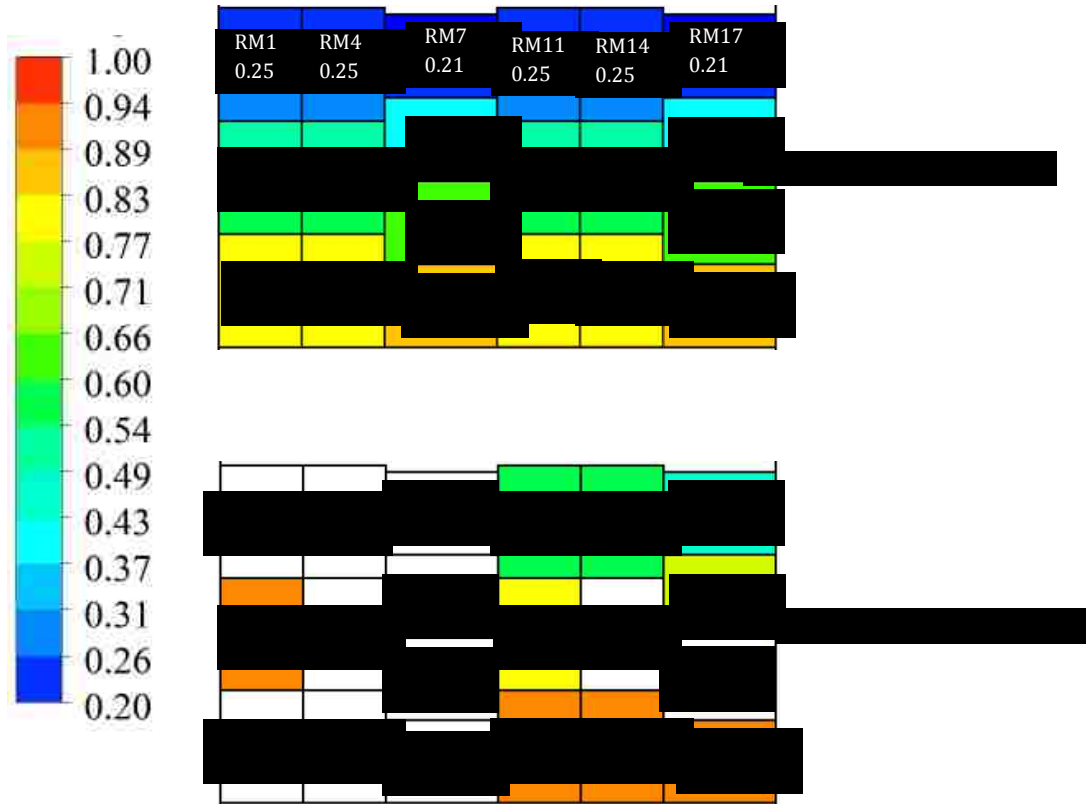
Figure 28: Dimensionless Vacuum Pressure Comparison

7.3 Numerical Velocity Magnitude

Although the velocity magnitude of the air is not measured during the experiment, the numerical results for the velocity magnitude are helpful in understanding the behavior of the model and will be referred to when explaining the results of the transient produce temperature variations in Section 7.5. The velocity magnitude from the numerical model is shown in Figure 29. It can clearly be seen that the superficial velocity magnitudes in the horizontally oriented boxes are predicted to be larger than those predicted for the vertically oriented boxes.

Figure 29: Numerical Velocity Magnitude of Modified Model

7.4 Numerical Heat Transfer Coefficients

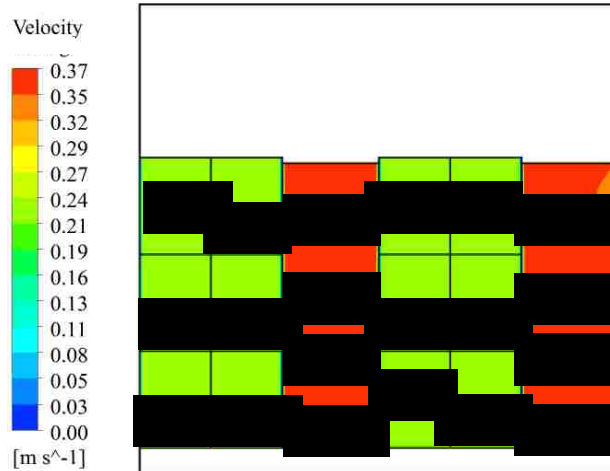The variation of heat transfer coefficient throughout the boxes is also useful in explaining the results of the model and will be referred to in Section 7.5. Contours of the predicted heat transfer coefficients, expressed in the units of W/m^2K, can be seen in Figure 30. From the figure, it becomes clear why the horizontally oriented boxes cool the fastest. Conversely, the vertically oriented boxes cool slower due to their reduced heat transfer coefficient compared to the horizontal containers.
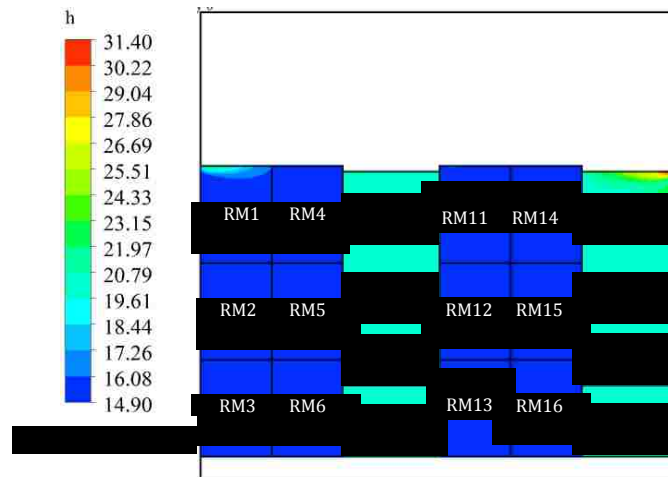

Figure 30: Numerical Heat Transfer Coefficient of Modified Model

7.5 Time Dependent Temperature Comparisons

The time dependent dimensionless temperature of the product in containers RM1 to RM10 (skipping RM5 and RM9 since they were not obtained experimentally) from the

50

experiment and numerical simulation are plotted in Figures 30 and 31. The plots are separated into two groups to reduce the congestion of the trend lines to allow clear comparisons. Each box is indicated using a specific color for comparison; however, data representing the experimental values are shown with symbols and the numerical data without symbols. The data corresponding to the slower cooling boxes RM6, RM3, RM2, and RM1 are presented in Figure 31 while the data corresponding to the faster cooling boxes RM10, RM8, RM7, and RM4 are shown in Figure 32.
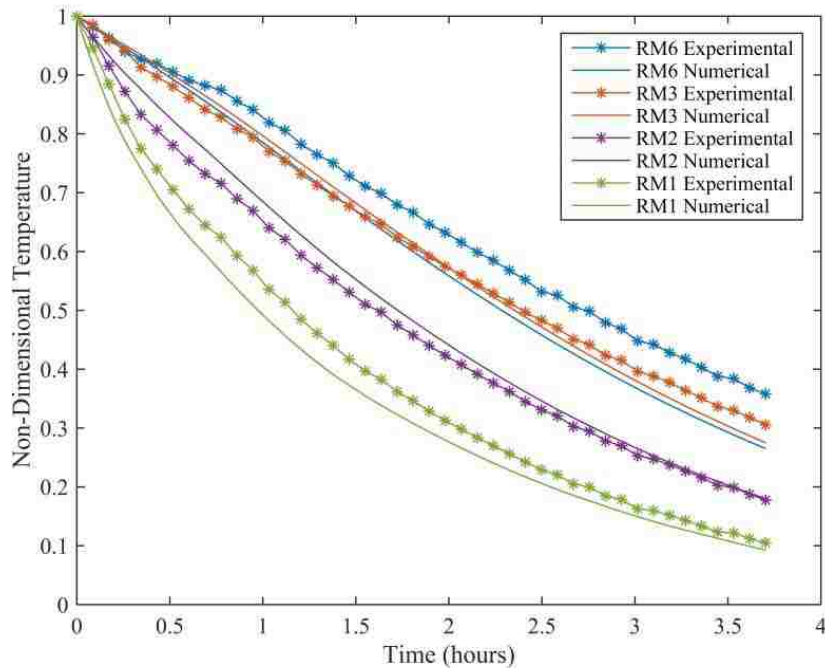
Figure 31: Transient Dimensionless Produce Temperature from Modified Model: Part 1

In Figure 31, it can be seen, for both the experimental and numerical results that the produce in container R1 cools the fastest of the four containers shown. This is due to the produce box in location RM1 being the first box to receive fresh cool air from the cold room. As the air flows in from the cold room, it cools the produce, and in turn gains heat. This leads to reduced potential for heat transfer as the warmed air must flow through subsequent containers into the tunnel section. Containers RM3 and RM6 show very similar experimental and numerical results due to their similar location with respect to the cold room.

Results similar to those seen in Figure 31 are observed in Figure 32. Once again, the fastest cooling produce container, RM7, is located closest to the cold room side. Although container RM4 is also situated next to the cold room, it is observed, both experimentally and numerically, to cool slower, than container RM7. This is due to the orientation of the containers and the resultant flow rate across the containers associated with those losses, consistent with Figures 28 and 29.
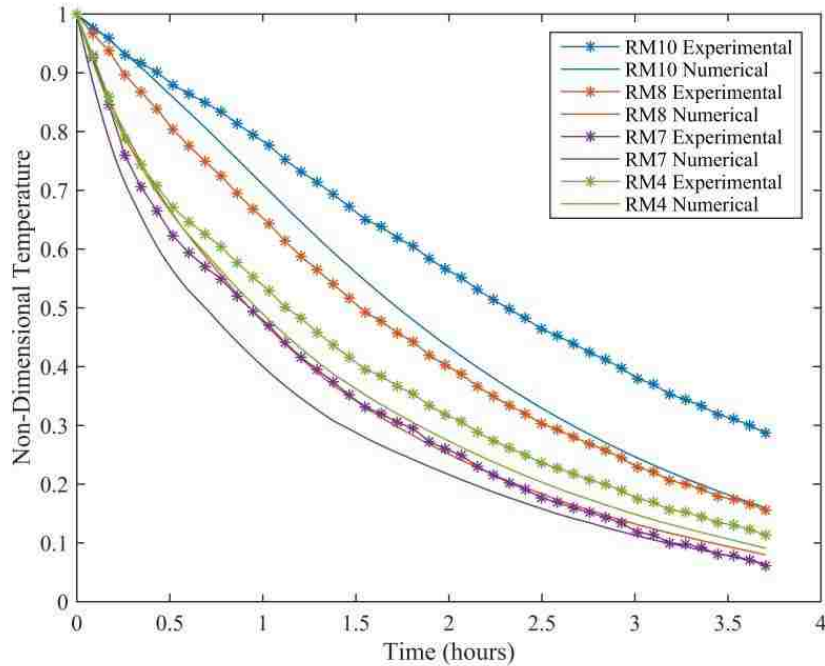
Figure 32: Transient Dimensionless Produce Temperature of Modified Model: Part 2

The maximum difference of the experimental and numerical time dependent dimensionless temperature is 18% that occurs at the RM8 location. The minimum difference is found at the RM3 location with a difference of 3%.

7.6 Half Cooling Time Comparison

The experimental and numerical results for the average half-cooling time (in hours) for each container can be seen in Figure 33. The maximum and minimum percent difference between the numerical and experimental results are 43% and 2% respectively. The maximum percent difference occurs in container RM8, while the minimum percent difference occurs in container RM6.

Figure 33: Comparison of Half Cooling Times of Modified Model

7.7 Summary of the Modified Numerical Model Study

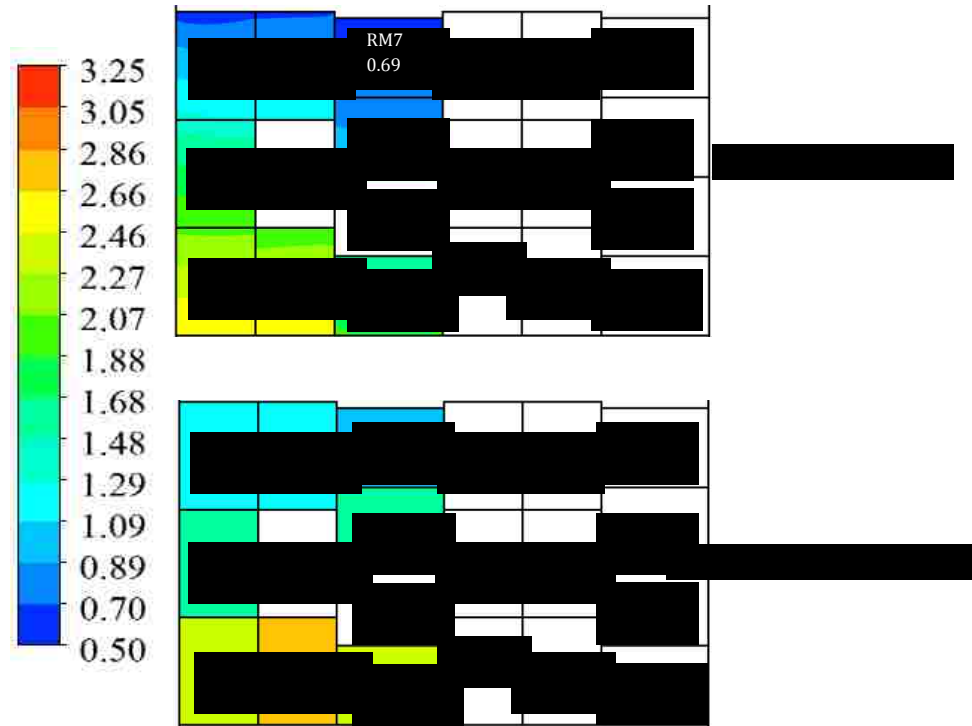Direct comparisons are made with experimental results and the modified numerical model for the case of medium cucumbers. The modified model includes non-uniform initial temperature and the variation in the room temperature. Despite the disagreement for pressure, the numerical transient temperature trends and values are in reasonable agreement with the experiment. This is based on the maximum percent difference of 41% with an experimental uncertainty ranging from ±6.9% to ±8.8% for measured pressures of -0.218 inches of water (-54.36 Pa), and -0.455 inches of water (-113.25 Pa) respectively. It is believed that zones of fluid by-pass (leaks) in the experiment that were not taken into account in the modified numerical model are the main source of the discrepancy. The predicted industry standard metric of half-cooling times are also compared and most containers show reasonable agreement. The maximum percent difference is determined to be 18%. This is considered as acceptable considering all the simplifying assumptions. The minimum uncertainty in the dimensionless temperature is ±4.7% occurring at location RM7. The maximum uncertainty in the dimensionless temperature is ±6.7 %, also at RM7. Additional modifications to the numerical model are

made to investigate whether leaks which cause by-pass of some of the cooling air around the produce boxes is a source of the discrepancy.

8. Numerical Model with Leaks and Comparisons

The effects of leaks in the numerical model are investigated using the same room zone conditions and initial values used in the previous chapter. The main difference is with the mesh and boundary conditions.

8.1 Mesh and Boundary Conditions with Leaks

In order to include areas where the cool air could by-pass the produce, zones of open air spaces are included in the mesh. They are added on each of the sides of the pallets of agricultural produce. The size of the by-pass zone is selected to be 1.5 inches (3.81cm). This yields gaps between the pallets and the walls of 1.5 inches (3.81cm) and a gap between the pallets of 3 inches (7.62cm). With the addition of the leak areas, porous jumps are included to the interacting container edges previously assumed to be blocked. The boundary conditions of the numerical model including provision for the leaks is shown in Figure 34.

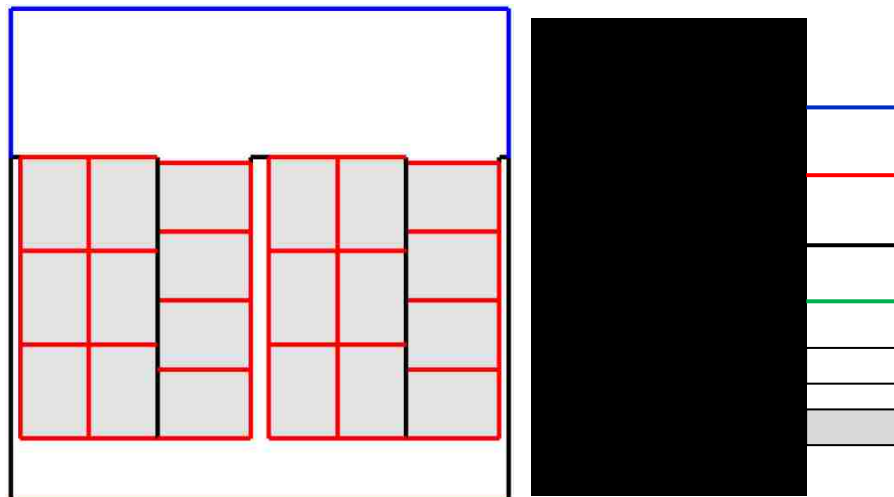**Figure 34: Boundary Conditions with Leaks**

8.2 Dimensionless Experimental Vacuum Pressure Comparison with Numerical Model Including Leaks

Comparison of the dimensionless pressure seen in the numerical model those in the experiments is shown in Figure 35. The pressure variation in the model containing leaks is in significantly better agreement with the experiment compared to the previous model

without leaks. The maximum and minimum percent difference is determined to be 18% and 5% respectively.
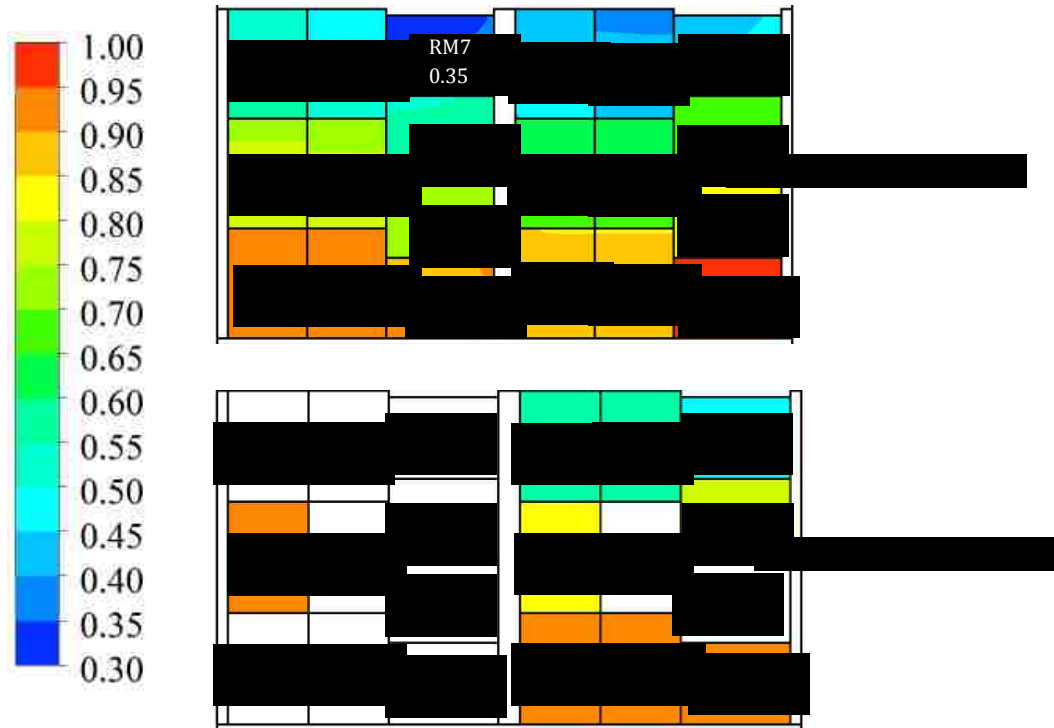
Figure 35: Dimensionless Vacuum Pressure Comparisons with Leaks

8.3 Numerical Velocity Magnitude

Contours or the velocity magnitude obtained from the model accounting for leaks are presented in Figure 36. It is observed that the velocity magnitude is largest at the outer edges of the product containers, which are in direct contact with either the cold room or leak area. The velocity magnitude is also observed to be lowest in the containers, which have no edges in direct contact with the leak area or cold room.
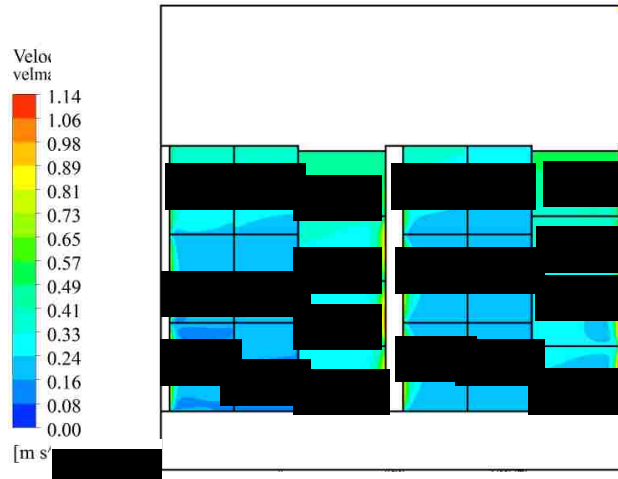
Figure 36: Numerical Velocity Magnitude of Model with Leaks

8.4 Numerical Heat Transfer Coefficient

Contours of the heat transfer coefficient in units of W/m^2K are presented in Figure 37. It can be seen that the maximum heat transfer coefficient is larger in the model containing leaks compared to those seen in the model without leaks. Similarly, the minimum heat transfer is lower as well. This is due to the non-uniform velocity field compared to those seen in the model with leaks.
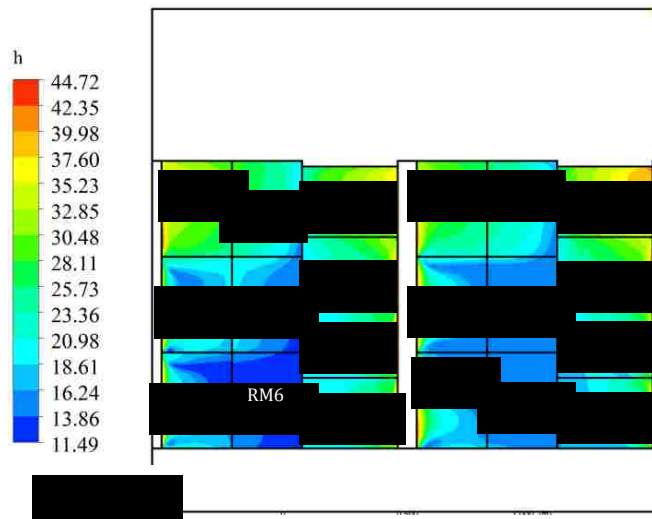
Figure 37: Numerical Heat Transfer Coefficient in Models with Leaks

8.5 Time Dependent Dimensionless Temperature Comparison

The time dependent dimensionless temperature comparison of the results of the numerical model with leaks to the experimental results is presented in Figure 38 and 39 in the same way as presented in the previous chapter. From both figures, it is clear that

the numerical model with leaks predicts faster cooling compared to the experiment. The maximum and minimum difference is computed to be 21% and 5% respectively. The maximum difference occurs in container RM8 and the minimum occurs in container RM6. The percent difference has increased, in general, compared to the model with no leaks.
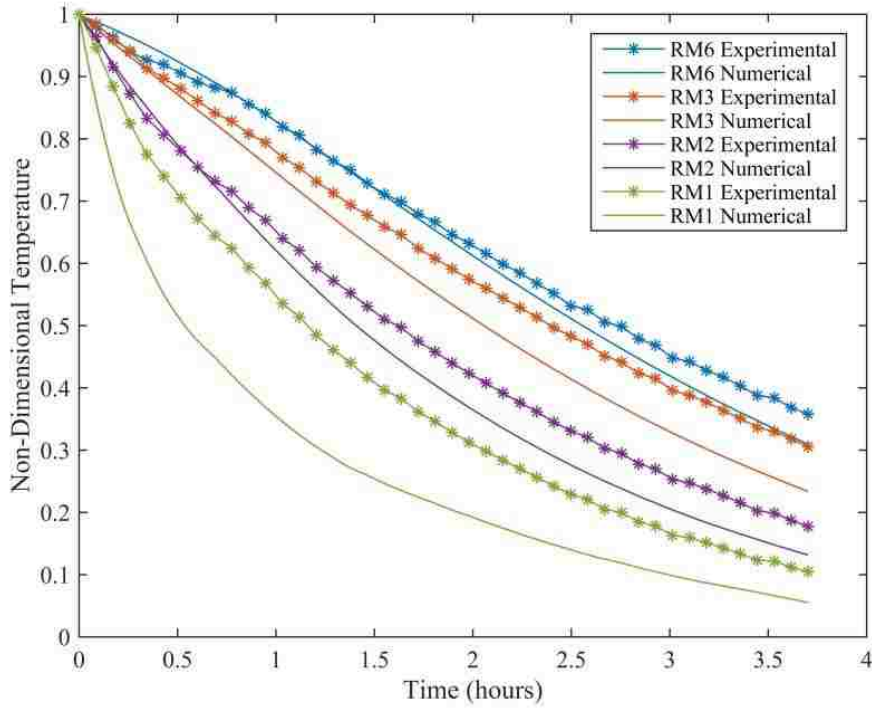
Figure 38: Transient Dimensionless Temperature for Model with Leaks: Part 1
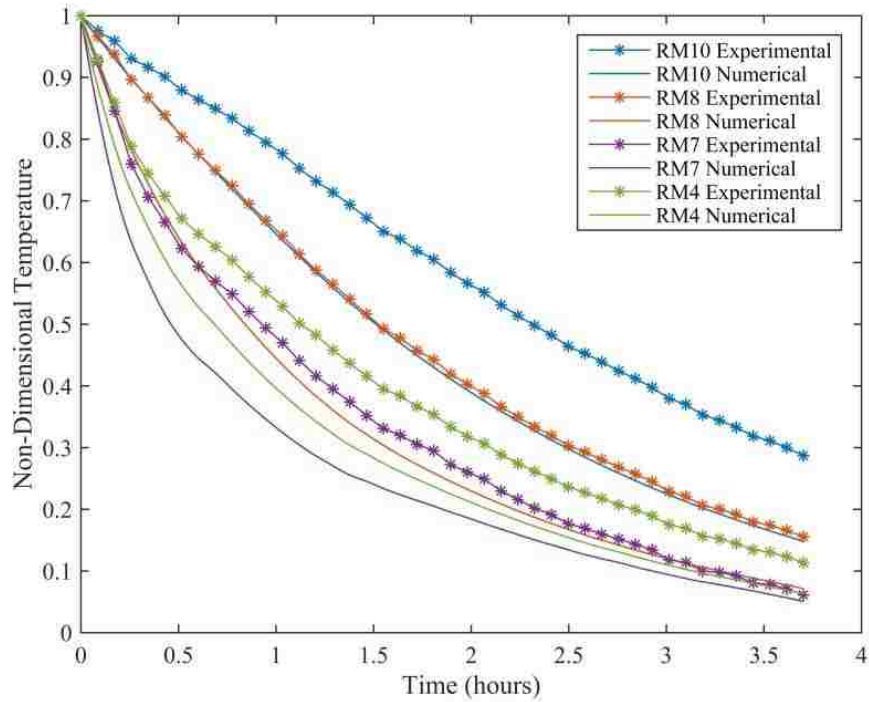
Figure 39: Transient Dimensionless Temperature for Model with Leaks: Part 2

8.6 Half Cooling Time Comparison

Comparisons of the half-cooling times predicted using the numerical model containing leaks and experiment can be seen in Figure 40. It is clear that the numerical model containing leaks is not in very good agreement with the half cooling times seen in the experiment. The maximum and minimum percent difference is determined to be 69% and 6% respectively, occurring in containers RM1 and RM6 respectively.

Figure 40: Half Cooling Time Comparisons of Model with Leaks

8.7 Summary and Discussion of the Numerical Model Including Leaks Study

An effort is made to investigate the modified numerical model with leaks to determine if they are responsible for the discrepancy between the numerical and experimental pressures. This is achieved by allowing fluid to by-pass some boxes into gaps that are introduced between containers and the walls across addi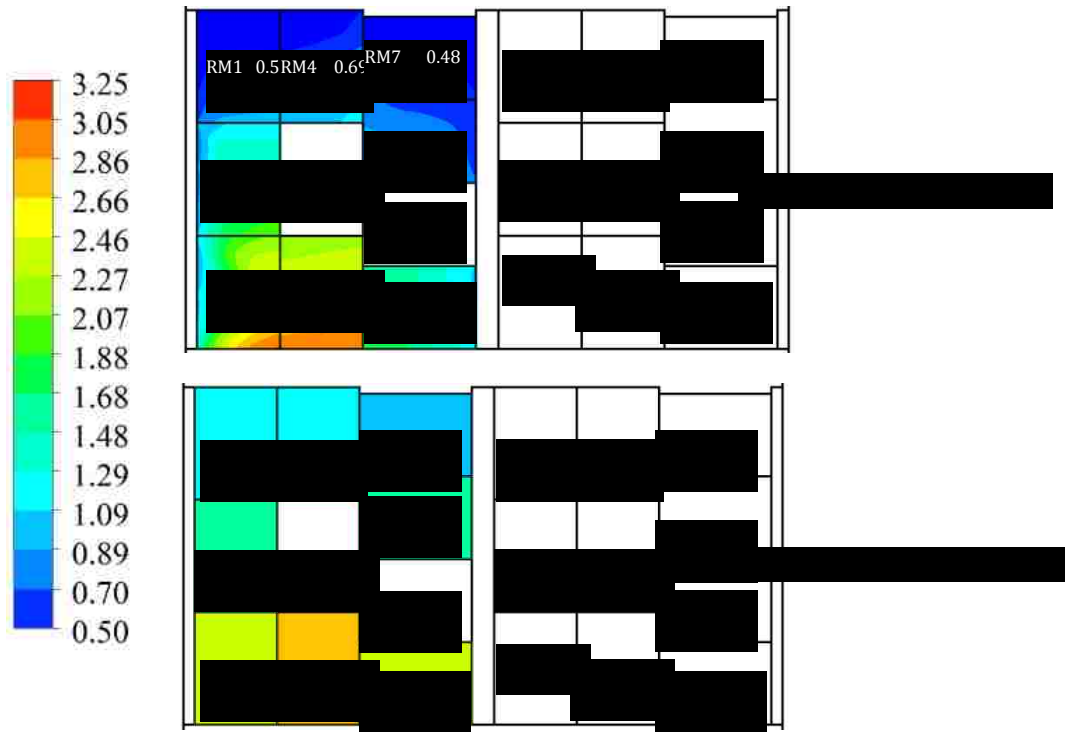tional porous jumps. The maximum percent difference for the dimensionless vacuum pressure is reduced to 17%. Not only is the maximum percent difference reduced by 23%, but the whole flow field can be visualized to be in much better agreement. It is important to note however that the size of the by-pass areas can only be estimated. The size of the by-pass area and relative size of the gap area between the pallets compared to those between the pallets and the walls have an impact on the numerical results. The agreement of the transient non-dimensional temperatures is observed to worsen with the inclusion of leaks. The maximum percent difference is seen to grow to 21%. This seems to imply that the heat transfer coefficients might not be appropriate. The experimental uncertainties for the dimensionless vacuum pressures and temperatures are the same as those indicated in section 7.7.

9. Investigation of Alternate Cooling Tunnel Configuration

From the results seen in previous chapter it is apparent that leaks are a significant factor affecting the accuracy of the simulation of forced air cooling in produce cooling tunnels. An alternate configuration is therefore, chosen for investigation that would potentially be less susceptible to leaks. The alternate configuration only considers one pallet on each side of the cooling tunnel due to the limited amount of product available during the day of experimental testing. All other conditions are kept the same in order to conduct a proper comparison. This configuration is also similar to a configuration made available commercially by Global Cooling Inc. [27].

9.1 Alternate Configuration Mesh

The alternate cooling tunnel configuration requires a different mesh than those used in previous chapters for two reasons. The first reason is the change in geometry already mentioned. The second reason is that the air is allowed to enter three sides of the pallet instead of just one seen in previous chapters. The mesh for the alternate configuration is displayed in Figure 41.
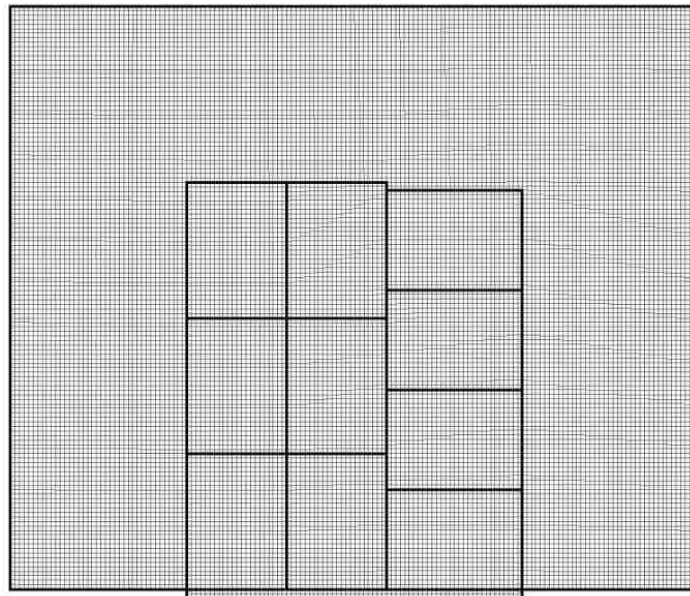

Figure 41: Alternate Configuration Mesh

9.2 Boundary Conditions

The conditions on the boundaries must be changed in order to allow air to flow into three sides of the pallets instead of just one. This is accomplished by removing the wall on the left and right hand sides and replacing them with porous jumps. The boundary conditions can be visualized with the help of Figure 42.
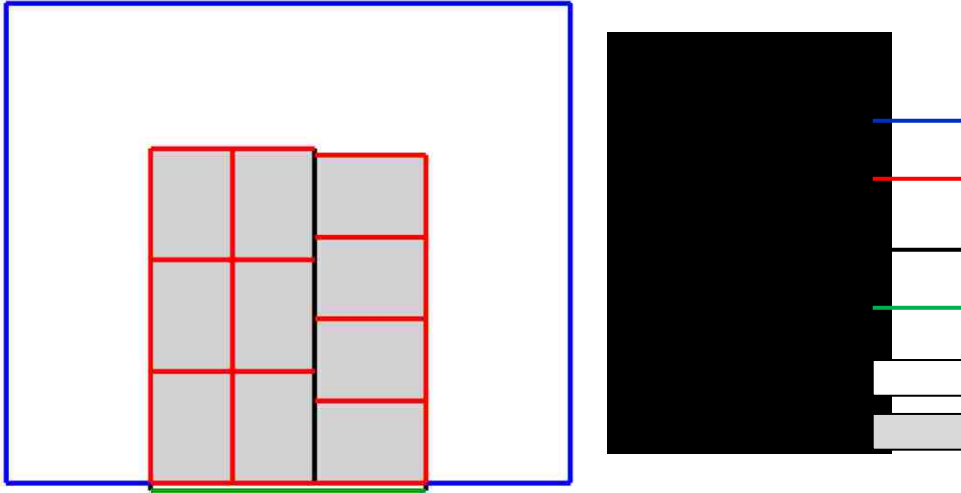

Figure 42: Alternate Configuration Boundary Conditions

9.3 Initial Conditions

The initial conditions for the alternate configuration are the same as those used in the modified numerical model. The initial temperatures of the produce are initialized to the same values as those seen in the experiment. It is important to note however that in this experiment the initial product temperatures are different from those seen in previous chapters. The initial product temperature range is from 20 ℃ to 17℃.

9.4 Cool Room Conditions

The cool room conditions are also approximated in the same manner as in the modified numerical model, however; the transient temperature of the room is significantly different. The transient experimental room temperature data can be seen to be in good agreement with the numerical approximation plotted in Figure 43. The behavior of the room temperature is cyclical due to the activation and deactivation of the cooling system based on some upper limit of temperature near 12.5 ℃.
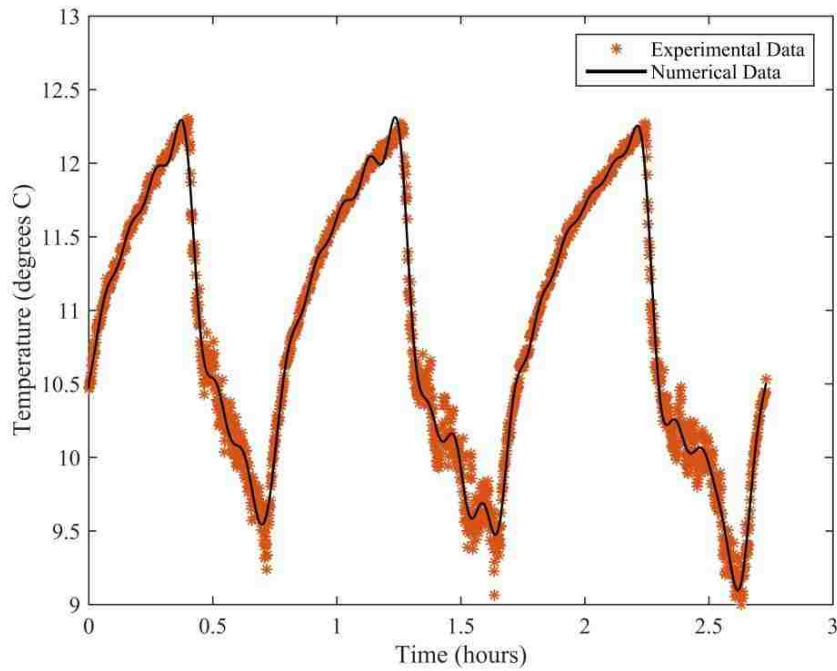
Figure 43: Transient Room Temperature for the Alternate Configuration

9.5 Dimensionless Vacuum Pressure Comparison

Comparison of the numerical and experimental results for the dimensionless vacuum pressure, for a tunnel pressure of -138 Pascals (Pa), can be seen in Figure 44. It is clear that the numerical and experimental results are in good agreement. The alternate configuration offers the best agreement between the non-dimensional vacuum pressures when comparing the numerical and experimental results. The maximum and minimum percent differences are found to be -6% and -1% respectively.
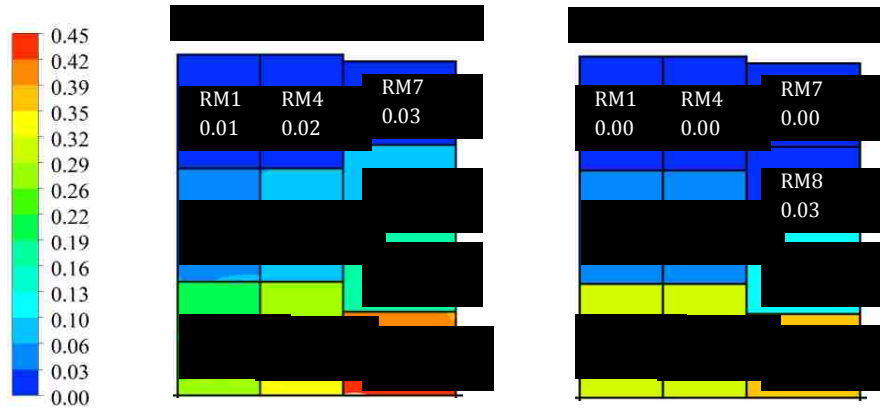
Figure 44: Dimensionless Vacuum Pressure Comparison for the Alternate Configuration

9.6 Numerical Velocity Magnitude

Contours of the numerical velocity magnitude in the case of the alternate configuration are presented in Figure 45. The velocity magnitude is seen, in general, to be larger for locations closer to the tunnel side and diminishes at locations further away.

Figure 45: Numerical Velocity Magnitude for the Alternate Configuration

9.7 Numerical Heat Transfer Coefficient

Contours of the numerical heat transfer coefficient are presented in Figure 46. The heat transfer coefficient is largest in the product containers that are in direct contact with the tunnel and the surroundings. The heat transfer coefficient is lowest in location RM4.
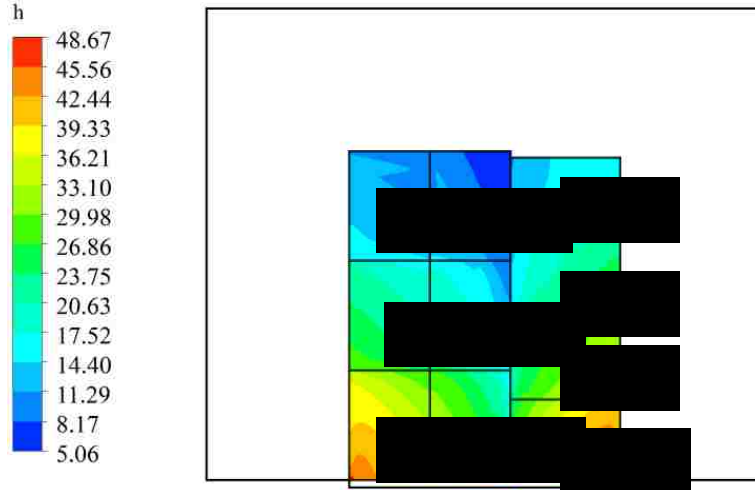
Figure 46: Numerical Heat Transfer Coefficient for the Alternate Configuration

9.8 Time Dependent Dimensionless Temperature Comparison
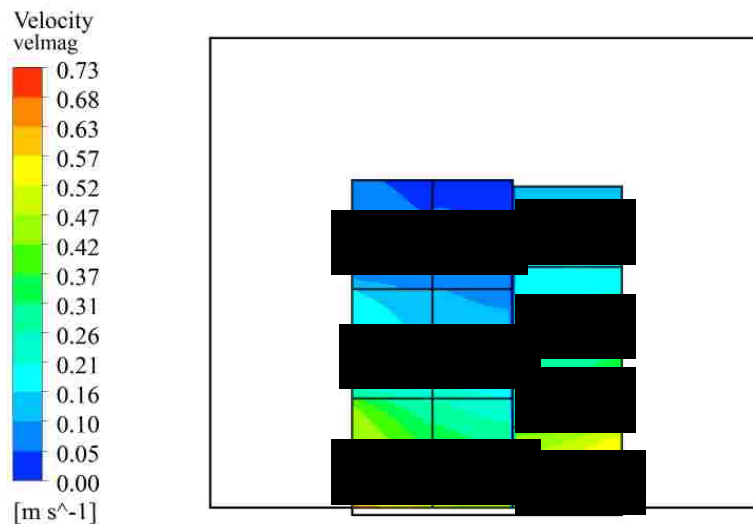
The numerical and experimental time dependent dimensionless temperatures are plotted in Figure 47 and 48 in the same way as in previous chapters. These figures show that the numerical model predicts faster cooling compared to the experiment. The fluctuating transient room temperature is also seen to have a more significant effect on the behavior of the cooling curve as indicated by their wavy behaviour.
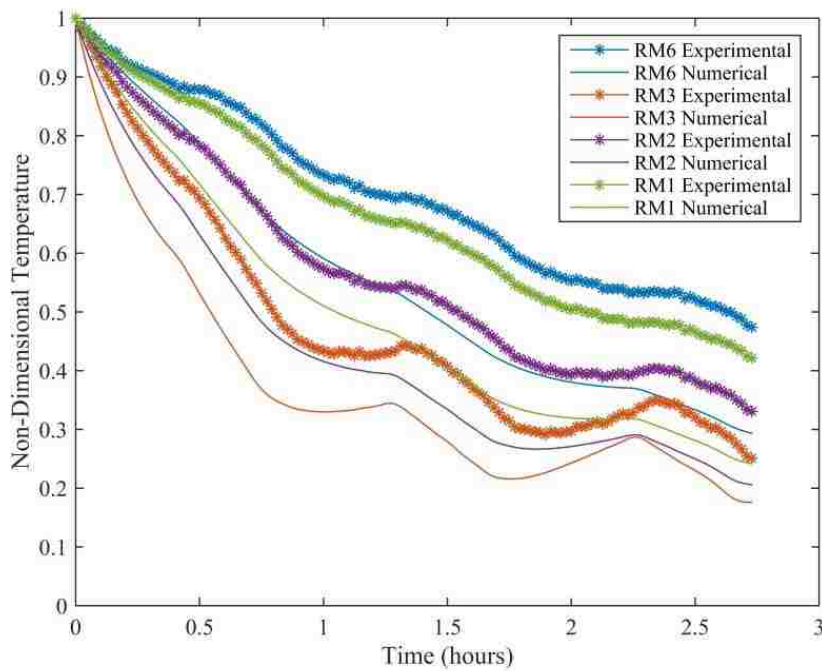
Figure 47: Transient Dimensionless Produce Temperature for the Alternate Configuration: Part 1
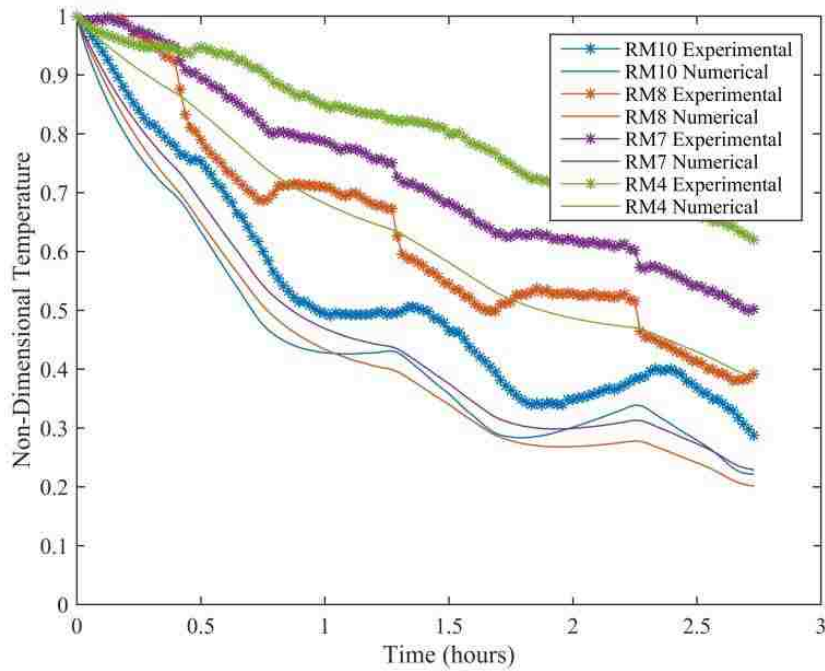
Figure 48: Transient Dimensionless Produce Temperature for the Alternate Configuration: Part 2

In Figure 48, the experimental results for locations RM7 and RM8 are suspected to be faulty. This is due to the sudden large decrease in dimensionless temperature that occurs at particular times during the cooling process. The slope of the sudden decrease is larger than that of the fastest cooling cucumber, which raises doubt on the validity of the measurement. It is clear that some transient event drastically affected the thermocouple readings in those two containers. For this reason, locations RM7 and RM8 have been replaced with data from locations RM5 and RM9 respectively and are plotted in Figure 49. Comparisons are made with Figure 47 and 49, as they are believed to represent more trustworthy data compared to Figure 48. The maximum percent difference is determined to be 25% and occurs in container RM4. The minimum percent difference occurs at location RM10 and is 14%.

Figure 49: Transient Dimensionless Product Temperature for the Alternate Configuration: Part 3

9.9 Alternate Configuration Summary
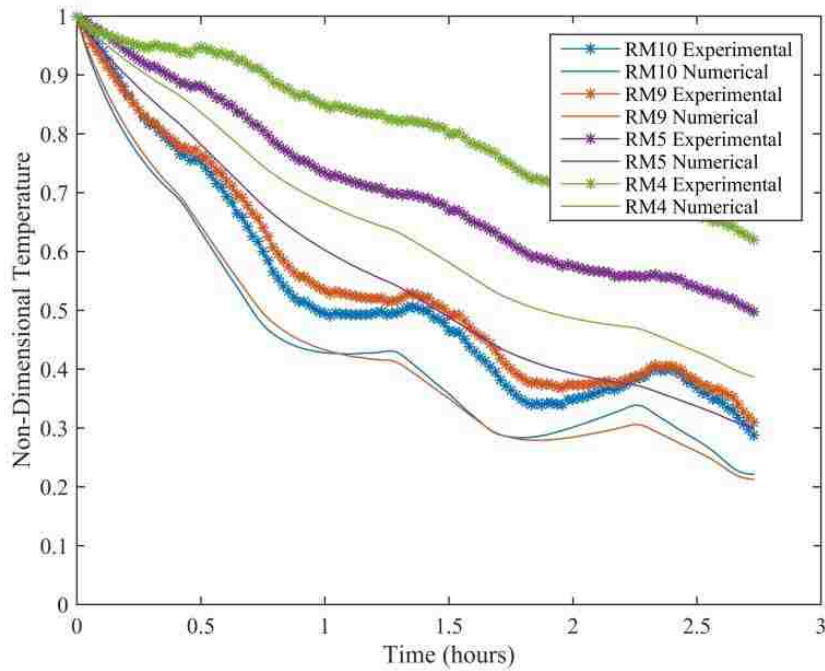
An alternate configuration is investigated where the air is allowed to enter through three sides of the pallets, as described in section 9.2 to 9.5. This type of configuration is believed to have to have less potential for by-pass (leak) errors. This is confirmed with the best overall agreement of dimensionless vacuum pressures. The maximum percent difference between the numerical and experimental dimensionless vacuum pressure is found to be -6%. Experimental uncertainty in the measured pressures are found to be in the range ±5.1% to ±7.3% for measured pressures of 0 inches of water (0 Pa), and -0.552inches of water (-138Pa) respectively. The agreement between the transient dimensionless temperatures however, is found to be the worst. The maximum percent difference between the dimensionless temperatures is calculated to be 25%. The minimum experimental uncertainty in the dimensionless temperature is ±5.6%, occurring at location RM5. The maximum experimental uncertainty in the dimensionless temperature is determined to be ±8.5%, in container RM10. When analyzing the comparisons time dependent dimensionless temperatures for the alternate configuration some consistency in the trends can be seen. Although the numerical model is observed to

67

over predict the cooling rate, the order of which containers cool (fastest to slowest) are in very good agreement. The alternate configuration also demonstrates the significant effect of the transient room temperature, numerically and experimentally.

10. Comparison of Numerical Models and Discussion

10.1 Comparison of Numerical Models

A summary of the maximum percent difference in the case of pressure variation in each tunnel configuration is found in Table 1. The experimental and numerical results for pressure are in the best agreement compared to other geometrical configurations in previous chapters. It is believed that this is due to the alternate orientation being less susceptible to by-pass since there are less blockages.

Model	Experimental Dimensionless Vacuum Pressure	Numerical Dimensionless Vacuum Pressure	Tunnel Pressure (Pa)	% Difference
Modified	0.94	0.53	-113	41%
Leaks Included	0.94	0.76	-113	18%
Alternate Configuration	0.12	0.18	-138	-6%

Table 1: Percent Difference in Pressures Summary

When comparing the numerical and experimental dimensionless produce temperature, the percent difference is seen to increase, compared to the previous configurations. The maximum percent difference for temperature is summarized in Table 2. Comparisons of the half-cooling times are not considered as not all the products reached half cool within the experiment due to time constraints.

Model	Experimental Dimensionless Temperature	Numerical Dimensionless Temperature	Minimum Room Temperature (°C)	% Difference
Modified	0.52	0.44	12	18%
Leaks Included	0.62	0.41	12	21%
Alternate Configuration	0.64	0.40	9	24%

Table 2: Percent Difference in Temperature Summary

10.2 Discussion

It is believed that the alternate configuration yields the most accurate comparison to experiment within this work. The reason for this is due to its superior agreement for the dimensionless vacuum pressures. It is important to recall that the numerical results for pressure rely on previously obtained empirical results. For this reason, the pressures obtained in the experiment should be in relatively good agreement. Since the superficial velocity and volume flow rates are directly related to the pressure, it is safe to assume that these flow variables are the most accurately predicted compared to previous models. When comparing the experimental and numerical temperatures, the agreement is the worst compared to other configurations in spite of the best agreement with pressures. The empirical models used for modeling forced convective heat transfer; however, have not been obtained experimentally within this work. In fact, the produce is not uniformly distributed within its container, unlike the conditions used to obtain the relationships for the heat transfer coefficients found in the literature. It is expected that a percentage of the air entering the product containers is bypassing the produce altogether, consistent with observations made by Ferrua and Singh [10]. This type of behavior would yield reduced heat transfer coefficients, as not all the cooling air encounters the produce.

11. Conclusions and Recommendations for Future Work

11.1 Conclusions

The following conclusions are made from this work:

- A simple computational model using the porous medium approximation is successfully developed to simulate forced air cooling in an agricultural produce cooling tunnel.

- Based on the results of the full-scale experiments, the assumptions of no flow between layers, and symmetric flow about the centre of the cooling tunnel, are shown to be appropriate; however, the assumptions of uniform initial temperature and constant room temperature are not.

- Modifications to the original numerical model to account for different initial produce temperatures as well as varying room temperature yielded reasonable results for the variation of produce temperature with time but not the product container pressures.

- Further modification of the model to approximate the leakage of air around rather than through the produce containers resulted in a much improved prediction of the produce container pressures but yielded produce temperature variations with time that are less accurate, hence flow leakage should be considered in studies of produce cooling tunnels

- Similar modeling of an alternative cooling tunnel configuration in which leakage is not a factor resulted in similar findings.

- The model used to estimate the heat transfer from the produce to the air is thought to be the likely cause of the discrepancies in temperature and hence improved methods must be developed.

11.2 Recommendations for Future Work

Treating the produce as a continuous porous medium does not accurately describe the heat transfer that occurs. It is expected that better agreement with the experimental results would be achieved with a 3-D model of the flow through one layer of stacked product,

which allows for the effect of the locations of the openings in the containers to be taken into account. The same empirically determined porous jump boundary conditions can be used to numerically model the container openings. The produce would still be treated as a porous medium to reduce computational time, however, the porous medium would occupy only regions of the container where produce is found, and not be fully distributed throughout each container. In this way some non-homogeneous flow would be observed, which would more accurately represent the physical behavior of the air within the containers. With the additional dimension, out of plane temperature gradients within the porous medium (produce) could also be captured.

Because the temperature of the room can have a significant effect on the cooling of the produce, some consideration should be made to estimate the response of the room to the rapid heat rejection by the produce. This will require more information on the characteristics of the room and cooling system.

Bibliography

[1] Brosnan, T., and Sun, D.-W., 2001, "Pre-cooling techniques and applications for horticultural products – a review," International Journal of Refrigeration, **24**(2), pp. 154‑170.

[2] Gross, K.C., C.Y. Wang, and M. Saltveit, 2002, The Commercial Storage of Fruits, Vegetables, and Florist and Nursery Stocks.

[3] Boyette, M. D., 1989, Introduction to Proper Postharvest Cooling and Handling Methods, The North Carolina Agricultural Extension Service, Raleigh, North Carolina Agricultural and Technical State University at Greensboro,.

[4] Fraser, H., 2014, "OMAFRA Factsheet 14-039: Forced-Air Cooling Systems for Fresh Ontario Fruits and Vegetables."

[5] Thompson, J. F., Mitchell, F. G., and Rumsay, T. R., 2008, Commercial Cooling of Fruits, Vegetables, and Flowers, University of California, Agriculture and Natural Resources.

[6] Pathare, P., Opara, U., Vigneault, C., Delele, M., and Al-Said, F.-J., 2012, "Design of Packaging Vents for Cooling Fresh Horticultural Produce," Food and Bioprocess Technology, **5**(6), pp. 2031‑2045.

[7] Zou, Q., 2002, "A CFD modelling system for air flow and heat transfer in ventilated packing systems during forced-air cooling of fresh produce," Doctor of Philosophy, Massey University.

[8] Amos, N. D., 1995, "Mathematical Modelling of Heat Transfer and Water Vapour Transport in Apple Coolstores," Doctor of Philosophy, Massey University.

[9] Tanner, J. D., 1998, "Mathematical Modelling for Design of Horticultural Packaging.," Massey University.

[10] Ferrua, M. J., and Singh, R. P., 2009, "Modeling the forced-air cooling process of fresh strawberry packages, Part I: Numerical model," International Journal of Refrigeration, **32**(2), pp. 335‑348.

[11] Ferrua, M. J., and Singh, R. P., 2009, "Modeling the forced-air cooling process of fresh strawberry packages, Part II: Experimental validation of the flow model," Int.J.Refrig., **32**(2), pp. 349‑358.

[12] Talbot, M. T., 1988, "An Approach to Better Design of Pressure-Cooled Produce Containers," Proceedings of the Florida State Horticultural Society, **101**, pp. 165‑175.

[13] Xu, Y., and Burfoot, D., 1999, "Simulating the bulk storage of foodstuffs," Journal of Food Engineering, **39**(1), pp. 23‑29.

[14] G. C. Misener and Gene C. Shove, 1976, "Simulated Cooling of Potatoes," Transactions of the American Society of Agricultural Engineers, **19**(5), pp. 954‑957&961.

[15] Verboven, P., Flick, D., Nicolaï, B. M., and Alvarez, G., 2006, "Modelling transport phenomena in refrigerated food bulks, packages and stacks: basics and advances," International Journal of Refrigeration, **29**(6), pp. 985‑997.

[16] Brown, G. O., 2002, "Henry Darcy and the making of a law," Water Resources Research, **38**(7), pp. 11‑1‑11‑12.

[17] Gauch, H. G., 2003, Scientific Method in Practice, Cambridge University Press.

[18] Nield, D. A., and Bejan, A., 2012, Convection in Porous Media, Springer.

[19] Dixon, A. G., and Cresswell, D. L., 1979, "Theoretical prediction of effective heat transfer parameters in packed beds," AIChE Journal, **25**(4), pp. 663‑676.

[20] Handley, D., and Heggs, P., 1968, "Momentum and heat transfer mechanisms in regular shaped packings," Transactions of the Institution of Chemical Engineers and the Chemical Engineer, **46**(9), p. T251.

[21] Wakao, N., and Kagei, S., 1982, Heat and Mass Transfer in Packed Beds, Gordon and Breach Science Publishers.

[22] Basu, P., 2006, Combustion and Gasification in Fluidized Beds, CRC Press.

[23] Martins, J. P., and Rankin, G. W., 2015, "An Investigation of Produce Cooling Tunnel Performance.," 11th International Conference on Heat Transfer, Fluid Mechanics and Thermodynamics, Skukuza, Kruger National Park, South Africa, pp. 737‑742.

[24] "Water Content and Water Activity: Two Factors That Affect Food Safety" [Online]. Available: http://www.gov.mb.ca/agriculture/food-safety/at-the-food-processor/water-content-water-activity.html. [Accessed: 22-May-2014].

[25] DeGroot, C. T., 2012, "Numerical Modelling of Transport in Complex Porous Media: Metal Foams to the Human Lung," University of Western Ontario.

[26] Priddy, K. L., and Keller, P. E., 2005, Artificial Neural Networks: An Introduction, Society of Photo Optical.

[27] "Portable precooler and recooler, best precooler, pressure cooler, and forced air precooler" [Online]. Available: http://www.pre-coolers.net/jet-precoolers.php. [Accessed: 15-Jun-2014].

[28] White, F. M., 2011, Fluid Mechanics, McGraw Hill.

[29] Fraser, H. W., 1998, Tunnel Forced-Air Coolers for Fresh Fruits and Vegetables, Ontario Ministry of Agriculture, Food and Rural Affairs, Ontario.

[30] Figliola, R. S., and Beasley, D. E., 2008, Theory and Design for Mechanical Measurements, 3RD ed, Wiley India Pvt. Limited.

[31] Kline, S. J., and McClintock, F., 1953, "Describing uncertainties in single-sample experiments," Mechanical engineering, **75**(1), pp. 3‑8.

Appendix A Permissions

A.1 Permissions for Use of Figure 1 and Figure 2

Dear Jean-Paul -

By way of this e-mail, permission is granted to Jean-Paul Martins to use Figure 7, appearing on page 8 and Figure 10 appearing on page 10 in Commercial Cooling of Fruits, Vegetables and Flowers, (ANR Publication 21567, ISBN 978-1-60107-619-9, J. Thompson) in your masters thesis as described in your e-mail inserted below. Please indicate that the material is "Copyright © 2008 Regents of the University of California. Used by permission."

Because of the age of this publication, we do not have an original file of the requested artwork; you may feel free to use a scan of the figures in your thesis.

Thank you for your interest in our publications, and furthering the work of Cooperative Extension.

Best regards,

Cynthia

Cynthia Kintigh
Marketing Director
University of California
Division of Agriculture and Natural Resources
Communication Services and IT
2801 2nd Street, Room 126
Davis, CA 95618

V: 530-750-1217

ucanr.edu
anrcatalog.ucanr.edu

A.2 Permission for Use of Figure 4

Springer

PERMISSION LETTER

Permission free of charge does not prejudice any rights we might have to charge for reproduction of our copyrighted material in the future.

Rights and Permissions
Springer Science+Business Media
Tiergartenstr. 17
69121 Heidelberg
Germany

Appendix B Preliminary Experiments

Preliminary experiments are necessary to obtain the porous medium and porous jump coefficients for the produce and produce container respectively. The test section constructed to obtain the required empirical coefficients and its functionality are described in section B.1. The experimental procedure, in point form, is covered in section B.2. The steps taken to reduce the data are given in section B.3. The Matlab code used along with an example of the curves fitted is included in section B.4. Finally, detailed drawings for the designed and constructed test section can be found in section B.5

B.1 Description of the Test Section and Functionality

A photo of the designed and constructed test section can be seen in Figure B1. In the figure, the test section is shown with the lid removed to display the enclosed produce.

Figure B1: Photo of Test Section

The experiments are conducted with the produce inside the product container and with the container empty in order to separate the effect of the product from that of the box. A vacuum is connected to the valve, which pulls air into the test section sown in the schematic Figure B2. The pressure drop is recorded across the full and empty boxes at pressure taps, on each side of the produce container, with an OMEGA HHP-103 handheld manometer. The flow rates are varied with the use of a valve set at different positions. The flow rates are obtained with the use of a Meriam Instruments E200I

78

handheld manometer along with the relationship of the pressure drop vs flow rate across a sharp edged orifice.
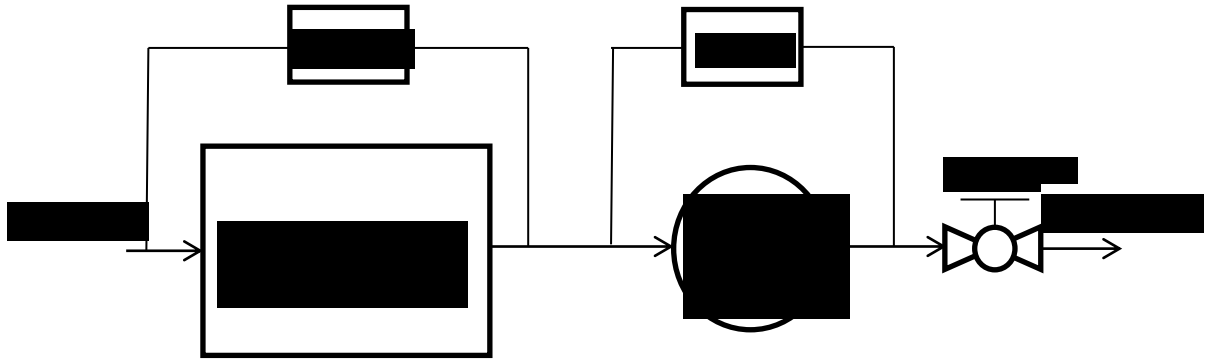
Figure B2: Test Section Schematic

B.2 Preliminary Experiments Procedure

In order to obtain the coefficient for multiple produce types and across both directions of the boxes the following experimental procedure is used:

1. Place produce container filled with produce into test section
2. Seal potential leak areas with tape
3. Place lid on test section and seal
4. Set valve to almost closed
5. Turn on vacuum on low setting
6. Record pressure drop across the container and orifice
7. Adjust valve to half closed
8. Record pressure drop across the container and orifice
9. Adjust valve to fully open
10. Record pressure drop across the container and orifice
11. Set valve to almost closed
12. Switch vacuum to high setting
13. Repeat steps 6 to 10
14. Complete a second trial by repeating steps 4 to 13
15. Turn the vacuum off
16. Open the lid and remove the produce from the container
17. Place lid on test section and seal

18. Repeat steps 4 to 14

19. Turn the vacuum off

This procedure is conducted for 7 different produce types in both (perpendicular) directions of the produce container with the container full and then empty. A total of 28 data sets are obtained.

B.3 Data Reduction

The resulting data set from one container in a single direction (full or empty) contains 12 measurements for both pressure drops across the entire produce container and sharp edged orifice. First, the pressure readings are converted from inches of water to Pa. The pressure drops are then divided by the length of the container in the flow direction; this will yield units of Pa/m. The pressure drops across the sharp edged orifice is converted into volume flow rates using Equation B1 obtained from Fluid mechanics 7th edition by Frank M. White [28].

$$Q = A_t V_t = C_d A_t \left[\frac{2(p_1 - p_2)/\rho}{1 - \beta_o^4} \right]^{1/2} \tag{B1}$$

In the above equation Q is the volume flow rate in units of m^3/s. It is assumed that the dimensionless discharge coefficient C_d is 0.6 and that the ratio of diameters is sufficiently large for β_o^4 to be essentially zero. The density of air, ρ_f, isassumed to be 1.225 kg/m^3 while A_t represents the cross-sectional area of the sharp edged orifice of diameter 1.25 inches (0.03175 m). The volume flow rate is then used to determine the superficial velocity by dividing the flow rate by the cross-sectional area of the container. Finally, the data for the pressure drop across the container per unit length is plotted against the superficial velocity, and a least squares fit with y intercept of zero is obtained to determine A and B in Equation B2. The coefficients obtained in the previous step can then be related to the required porous medium coefficients K and C_2using Equation B2.

$$\nabla P = \frac{\Delta P}{L} = Av + Bv^2 = -\frac{\mu}{K}v - \frac{1}{2}C_2\rho_f|v|v \tag{B2}$$

To separate the pressure losses associated with the vent holes in the product container from that of the flow passing through the porous medium, experiments are conducted

with the product containers full of produce and with empty containers. In this way when the pressure for the empty produce container is subtracted from that of the product container full of product, the pressure loss associated to the produce is all that remains. The assumption is also made that the pressure drop for the air entering or exiting the empty container is equal to half of that of the pressure drop across the entire empty container.

B.4 Matlab Code

The post processing of the experimental data obtained in the initial experiments is conducted using Matlab. The original data and some parameters are scanned into Matlab from the original Excel files using the built in "xlsread" function. The data is then processed accordingly in order to get the coefficients in the correct desired units. A sample code for the data reduction of medium cucumbers can be found below in Figure B3, along with the curve for the pressure drop vs superficial velocity in Figure .

```
%medium cucumber
clear
clc

%data collection and plotting

%Global variables
rho=1.225; %air density in (kg/m^3)
mu=1.7894*(10^-5); %air viscosity in (kg/m*s)
tb=.35*25.4/1000; %measured thickness of the cardboard box in (m)
H2OtoPa=249.174; %coverts inches of water to pascals
Cd=0.6; %dimesionless discharge coeficcient
dt=1.25*25.4/1000; %diameter of the orifice in (m)
At=(pi*dt^2)/4; %area of the orifice in (m^2)

%Dimensions of the box
ll=xlsread('medium cucumber  nov 5th long.xlsx','Test1','N2'); %length of the box in (m)
ls=xlsread('medium cucumber  nov 5th short.xlsx','Test1','N2'); %width of the box in (m)
hbox=4.25*25.4/1000; %height of the box in (m)

%Long Direction Full
dpfulll=xlsread('medium cucumber  nov 5th long.xlsx','Test1','D2:D13'); %reads pressure
drop across the box in inches of water
dpfulll=dpfulll*H2OtoPa; %converts inches of water to Pa
plfulll=dpfulll./ll;
dpofulll=xlsread('medium cucumber  nov 5th long.xlsx','Test1','E2:E13'); %reads pressure
drop across the orifice in inches of water
dpofulll=dpofulll*H2OtoPa;
Qfulll=Cd*At*sqrt(2*dpofulll./rho);
```

```matlab
Ufulll=Qfulll./(ls*hbox);
%fitting the data
plfl=polyfitzero(Ufulll,plfulll,2);
plflcurve=polyval(plfl,linspace(0,max(Ufulll)));
Cfl=2*plfl(1)/rho;
Kfl=mu/plfl(2);
dpfl=polyfitzero(Qfulll,dpfulll,2);


%Long Direction Empty
dpempl=xlsread('medium cucumber  nov 5th long.xlsx','Test1','D17:D28'); %reads pressure
drop across the box in inches of water
dpempl=dpempl*H2OtoPa; %converts inches of water to Pa
plempl=dpempl./ll;
dpoempl=xlsread('medium cucumber  nov 5th long.xlsx','Test1','E17:E28'); %reads pressure
drop across the orifice in inches of water
dpoempl=dpoempl*H2OtoPa;
Qempl=Cd*At*sqrt(2*dpoempl./rho);
Uempl=Qempl./(ls*hbox);
%fitting the data
plel=polyfitzero(Uempl,plempl,2);
plelcurve=polyval(plel,linspace(0,max(Uempl)));
Cel=2*plel(1)/rho;
Kel=mu/plel(2);
dpel=polyfitzero(Qempl,dpempl,2);


%Short Direction Full
dpfulls=xlsread('medium cucumber  nov 5th short.xlsx','Test1','D2:D13'); %reads pressure
drop across the box in inches of water
dpfulls=dpfulls*H2OtoPa; %converts inches of water to Pa
plfulls=dpfulls./ls;
dpofulls=xlsread('medium cucumber  nov 5th short.xlsx','Test1','E2:E13'); %reads pressure
drop across the orifice in inches of water
dpofulls=dpofulls*H2OtoPa;
Qfulls=Cd*At*sqrt(2*dpofulls./rho);
Ufulls=Qfulls./(ll*hbox);
%fitting the data
plfs=polyfitzero(Ufulls,plfulls,2);
plfscurve=polyval(plfs,linspace(0,max(Ufulls)));
Cfs=2*plfs(1)/rho;
Kfs=mu/plfs(2);
dpfs=polyfitzero(Qfulls,dpfulls,2);


%Short Direction Empty
dpemps=xlsread('medium cucumber  nov 5th short.xlsx','Test1','D17:D28'); %reads pressure
drop across the box in inches of water
dpemps=dpemps*H2OtoPa; %converts inches of water to Pa
plemps=dpemps./ls;
dpoemps=xlsread('medium cucumber  nov 5th short.xlsx','Test1','E17:E28'); %reads pressure
drop across the orifice in inches of water
dpoemps=dpoemps*H2OtoPa;
Qemps=Cd*At*sqrt(2*dpoemps./rho);
Uemps=Qemps./(ll*hbox);
%fitting the data
```

```matlab
ples=polyfitzero(Uemps,plemps,2);
plescurve=polyval(ples,linspace(0,max(Uemps)));
Ces=2*ples(1)/rho;
Kes=mu/ples(2);
dpes=polyfitzero(Qemps,dpemps,2);

%Properties of the Produce
Cpl=(2/rho)*(plfl(1)-plel(1))
Kpl=mu/(plfl(2)-plel(2))
Apl=dpfl(1)-dpel(1)
Bpl=dpfl(2)-dpfl(1)
Cps=(2/rho)*(plfs(1)-ples(1))
Kps=mu/(plfs(2)-ples(2))
Aps=dpfs(1)-dpes(1)
Bps=dpfs(2)-dpfs(1)

%Properties of the interface
Cbl=(plel(1)*ll/tb)/rho
Kbl=(2*mu/plel(2))*tb/ll
Abl=dpfl(1)/2
Bbl=dpfl(2)/2
Cbs=(ples(1)*ls/tb)/rho
Kbs=(2*mu/ples(2))*tb/ls
Abs=dpfs(1)/2
Bbs=dpfs(2)/2

%properties of combined interfaces
Cbls=((plel(1)*ll+ples(1)*ls)/tb)/rho
Kbls=(2*mu/((plel(2)*ll+ples(2)*ls)))/tb
Abls=Abl+Abs
Bbls=Bbl+Bbs

%Plotting aquired data curves and fit
subplot(1,2,1)
plot(linspace(0,max(Ufulll)),plflcurve,'b',linspace(0,max(Uempl)),plelcurve,'r',Ufulll,pl
fulll,'*b',Uempl,plempl,'*r');
grid on
title('Long')
xlabel('U (m/s)')
ylabel('DeltaP/l (Pa/m)')
legend('full','empty')

subplot(1,2,2)
plot(linspace(0,max(Ufulls)),plfscurve,'b',linspace(0,max(Uemps)),plescurve,'r',Ufulls,pl
fulls,'*b',Uemps,plemps,'*r');
grid on
title('Short')
xlabel('U (m/s)')
ylabel('DeltaP/l (Pa/m)')
legend('full','empty')
```
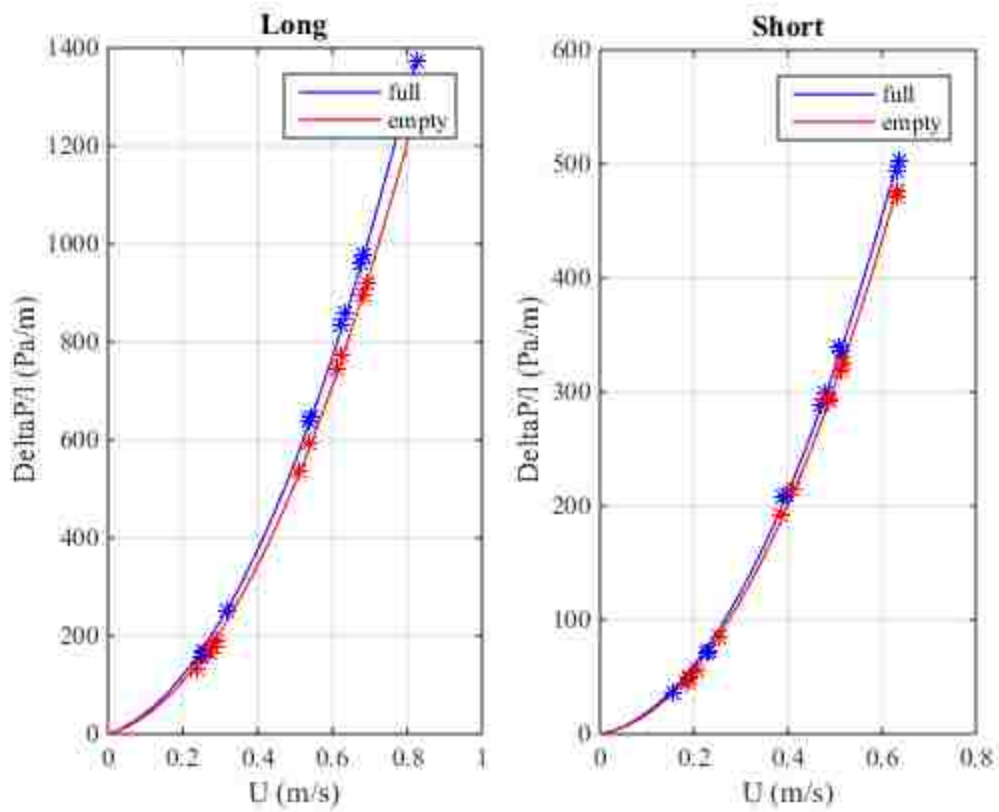
Figure B3: Matlab Code for Preliminary Experiments

Figure B4: Pressure Drop vs Superficial Velocity

B.5 Detailed Drawings of Test Section

The detailed drawings of the test section used for these experiments have been included in order to allow reproduction of the experiment. All units are in inches.
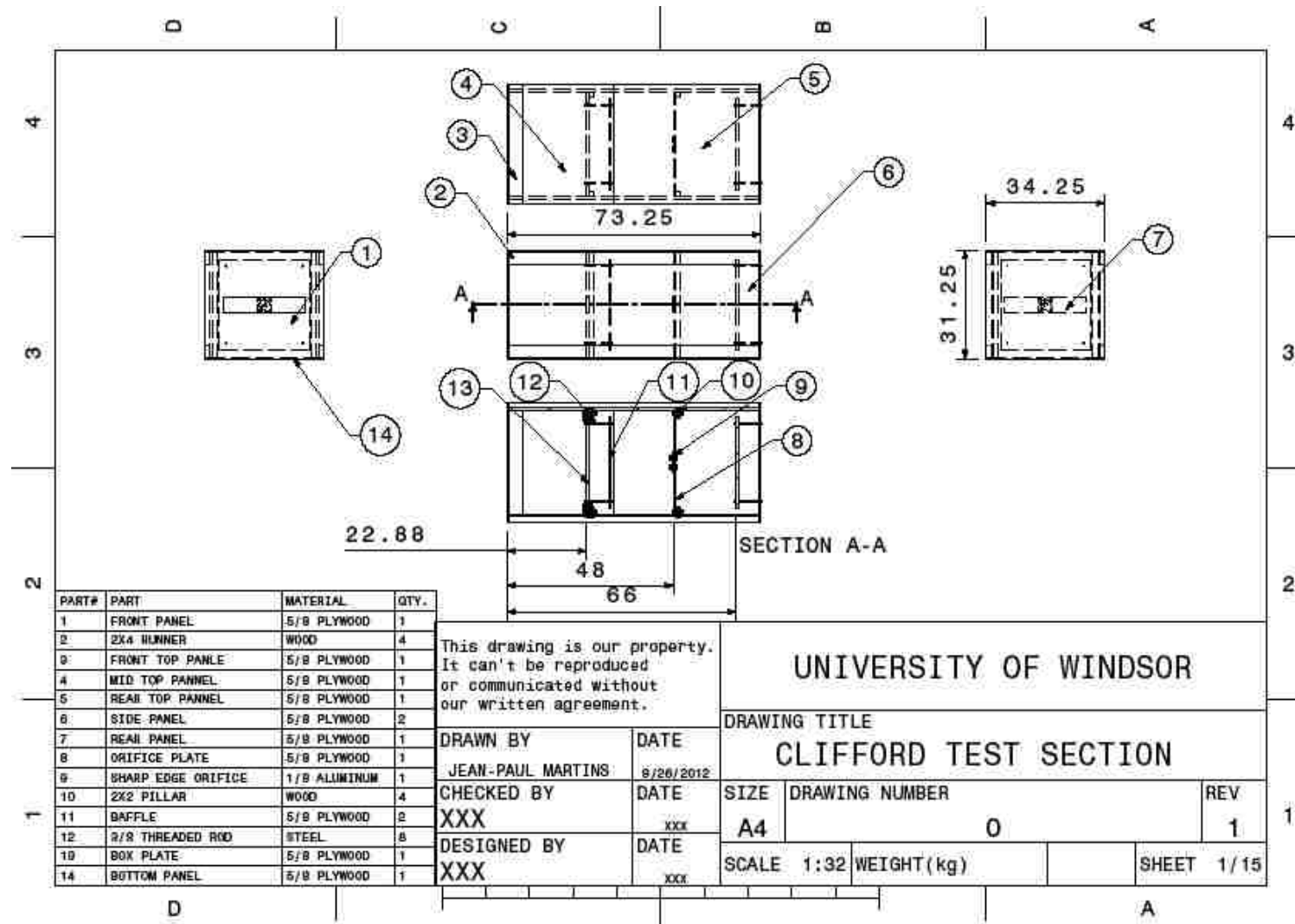
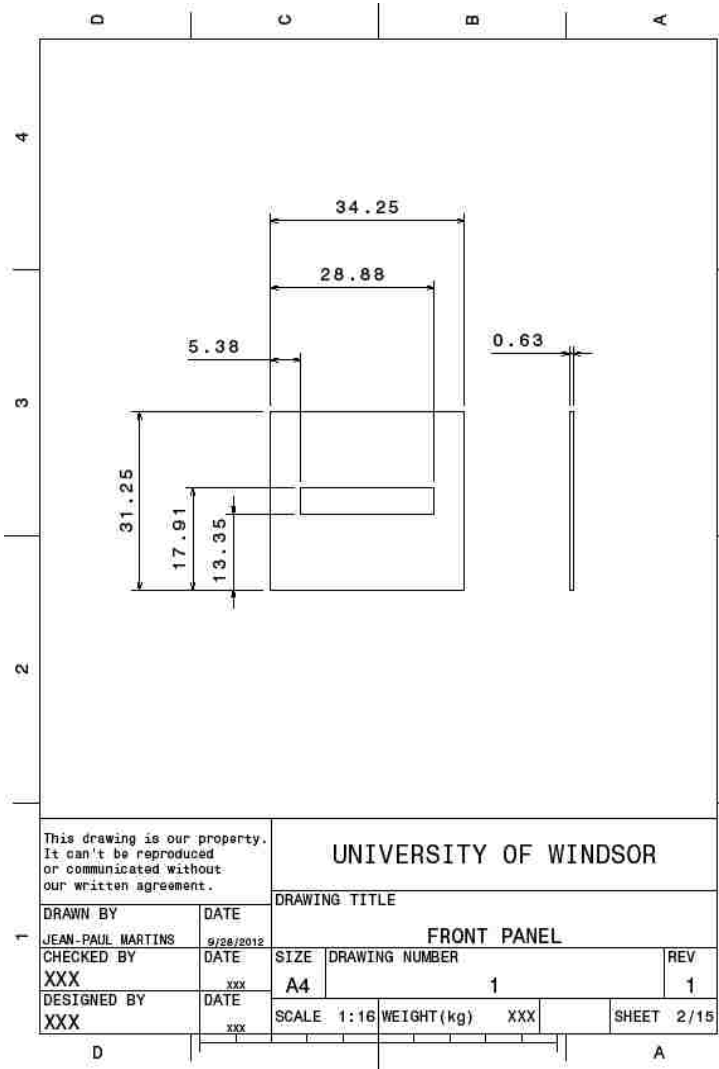**Figure B5: Assembly Drawing of Test Section**
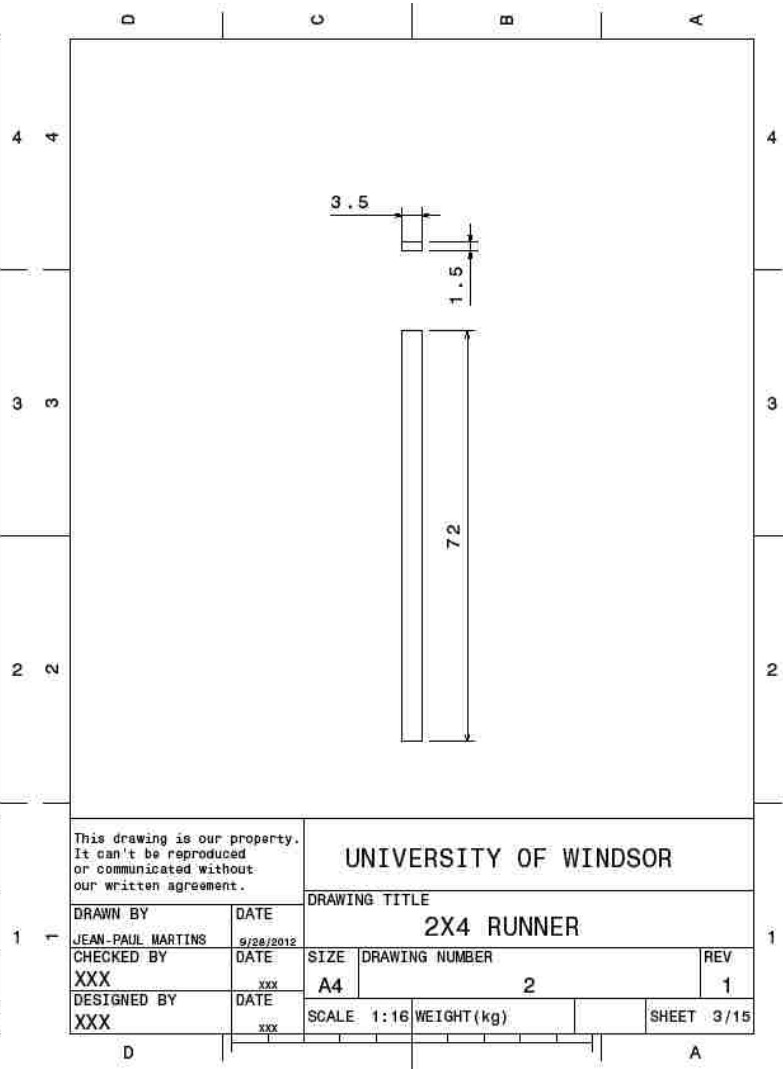
Figure B6: Front Panel

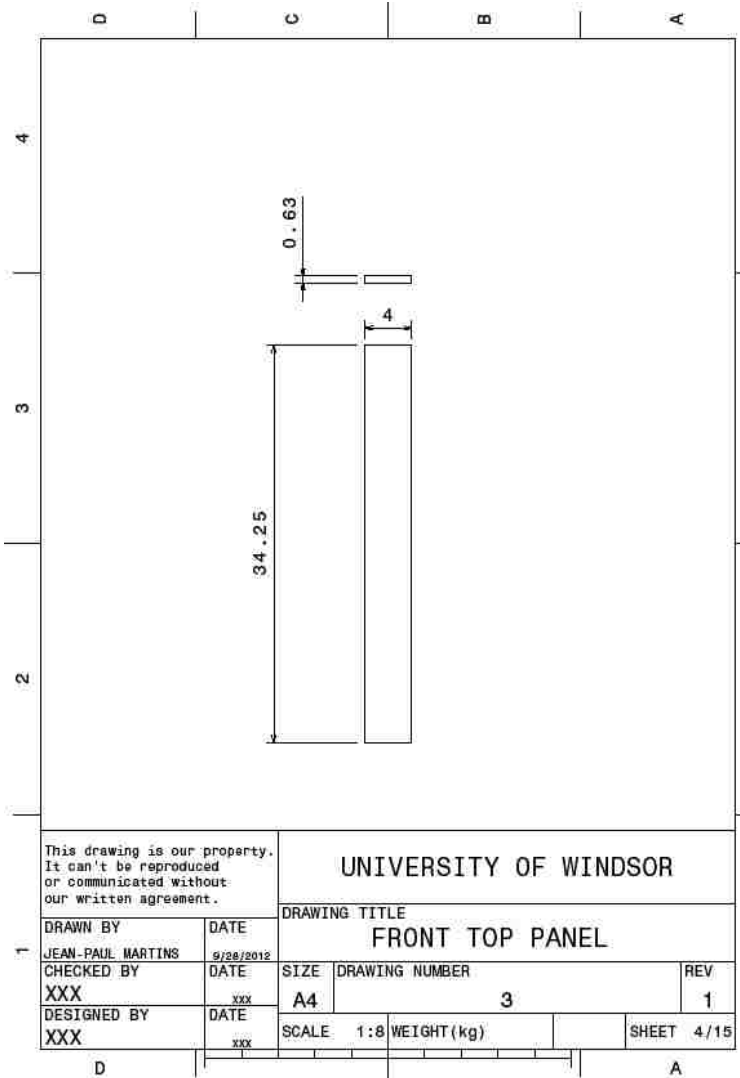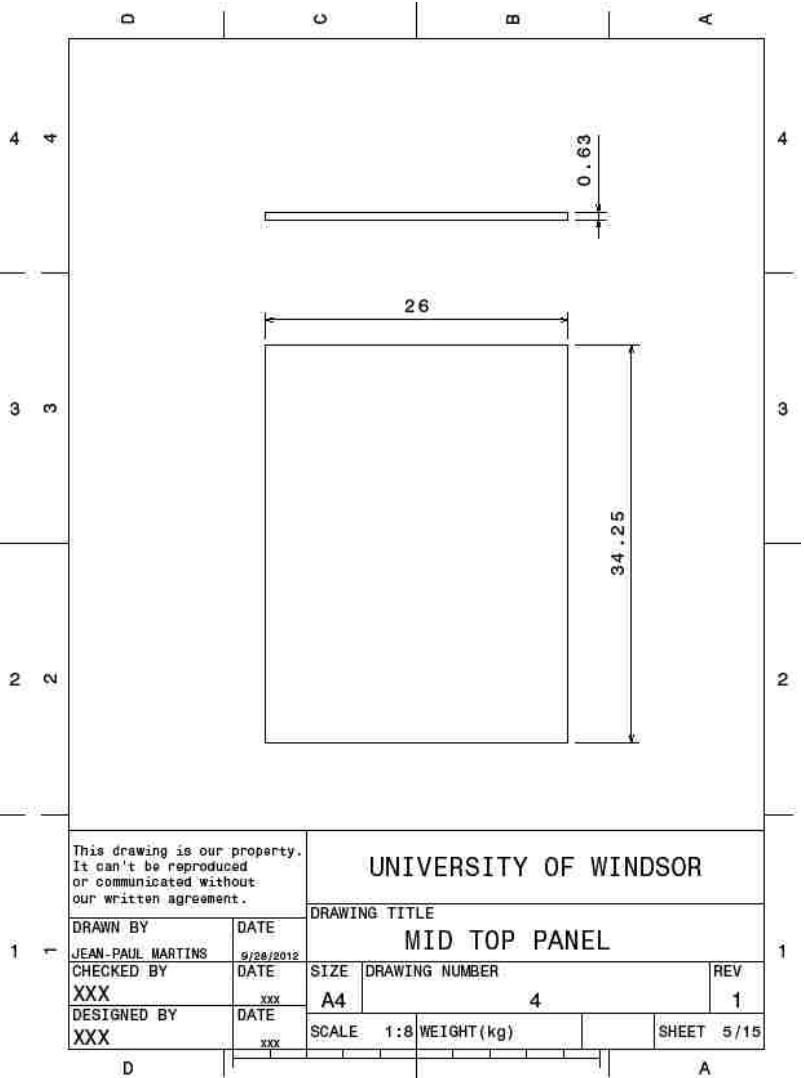**Figure B7: 2X4 Runner**

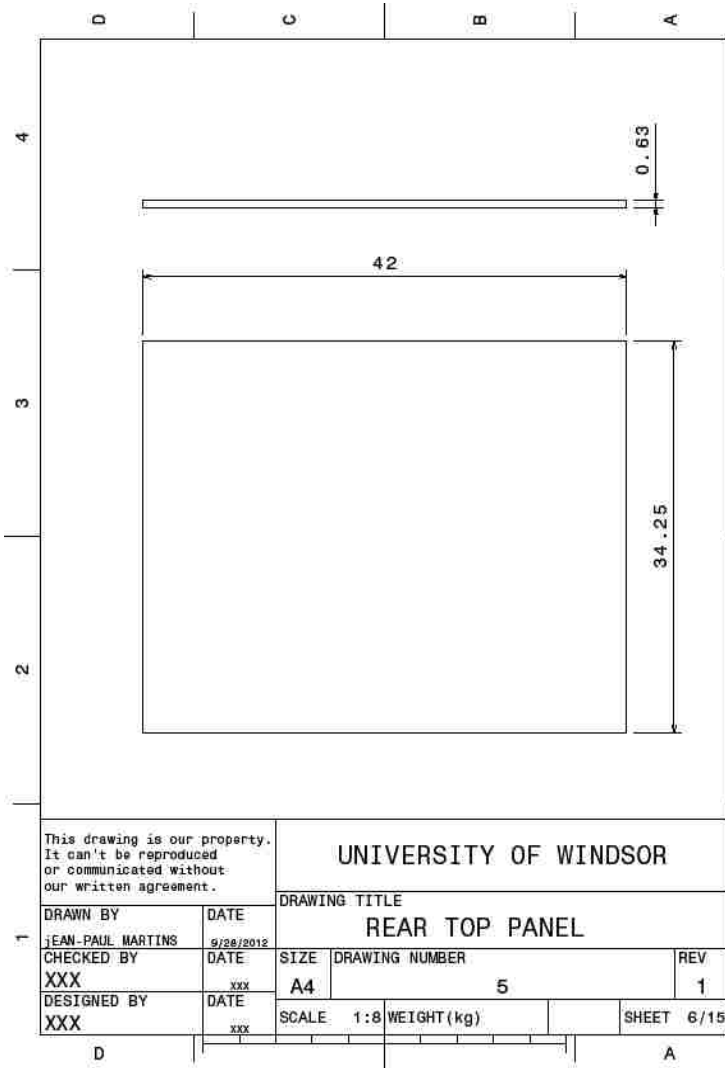**Figure B8: Front Top Panel**

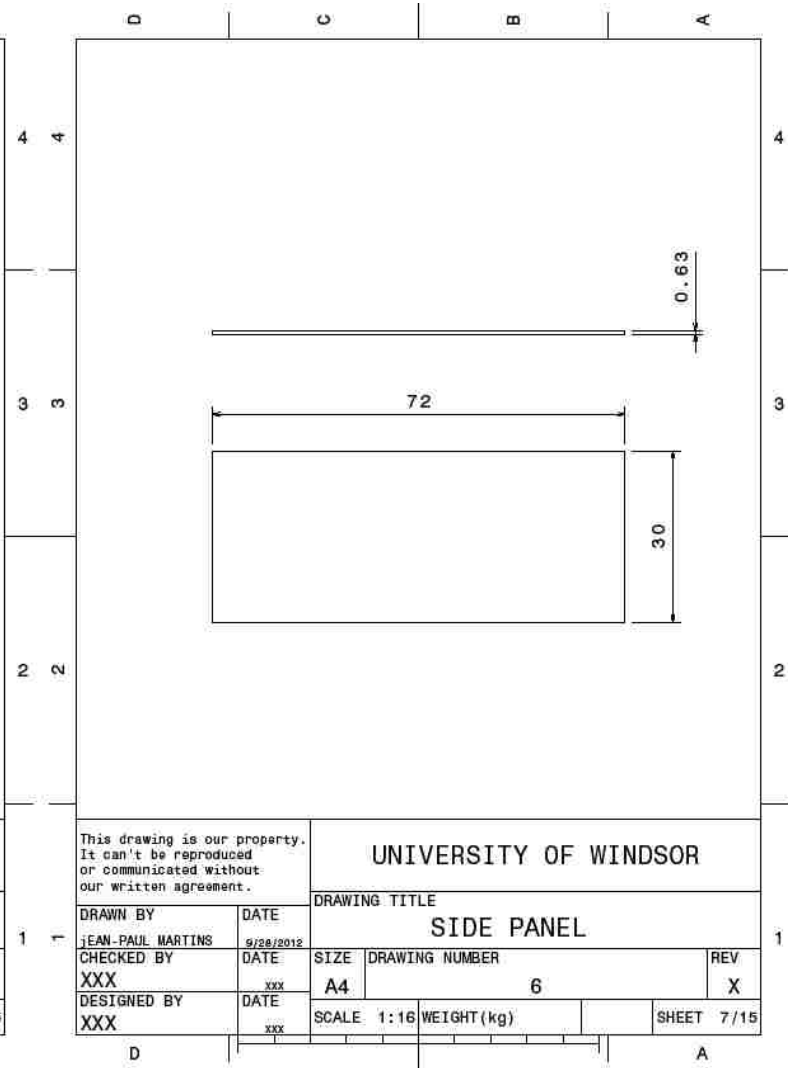**Figure B9: Mid Top Panel**
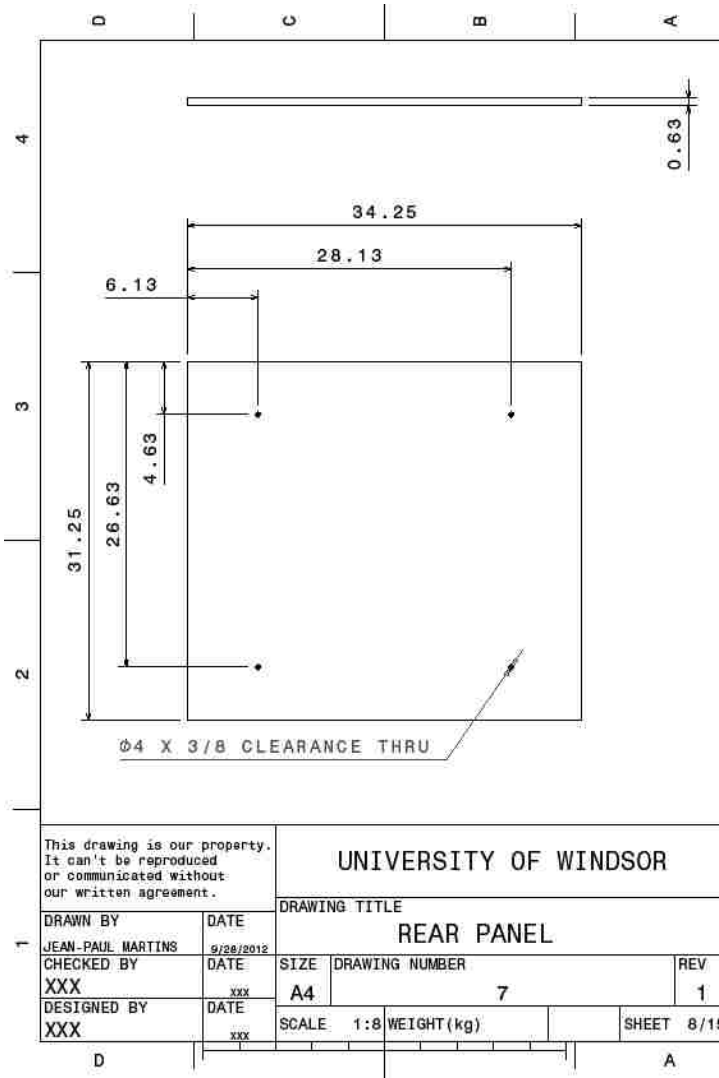
Figure B10: Rear Top Panel
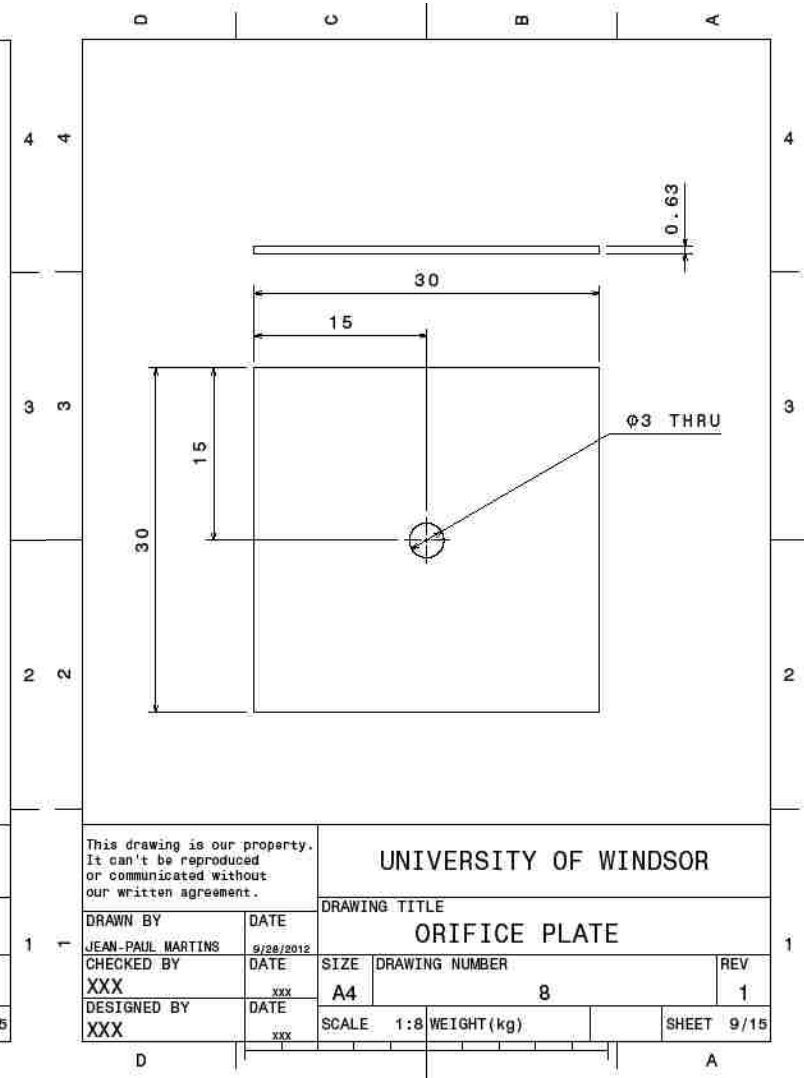

Figure B11: Side Panel
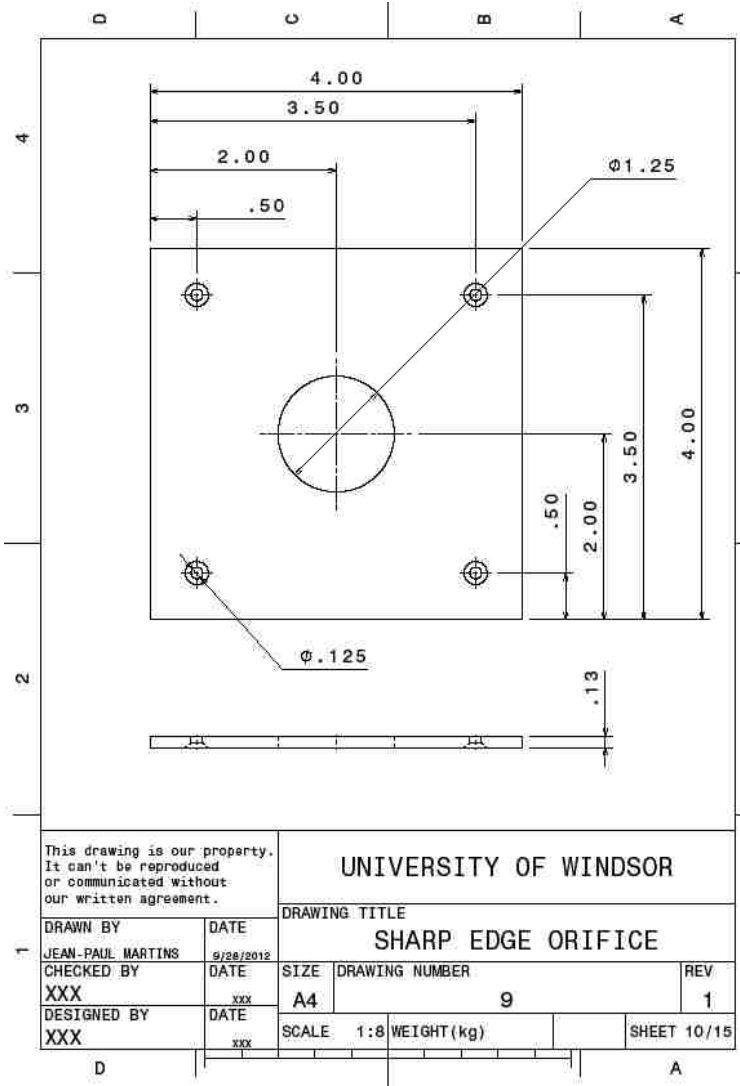
Figure B12: Rear Panel

Figure B13: Orifice Plate

89

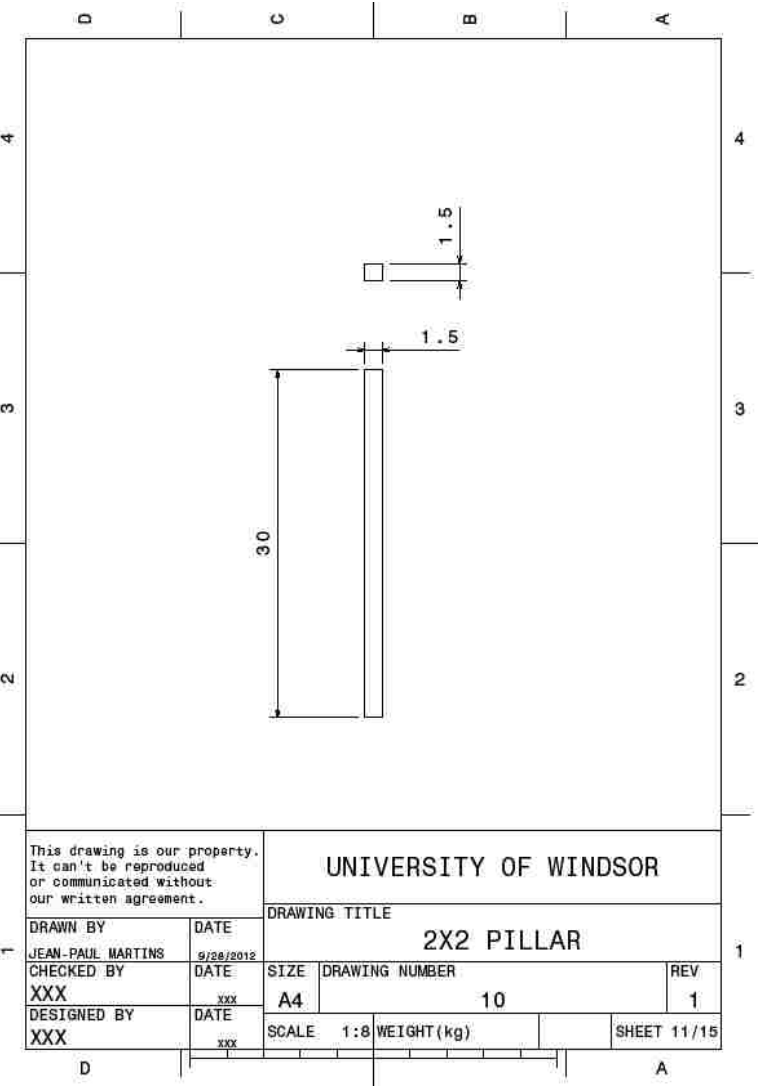**Figure B14: Sharp Edge Orifice**

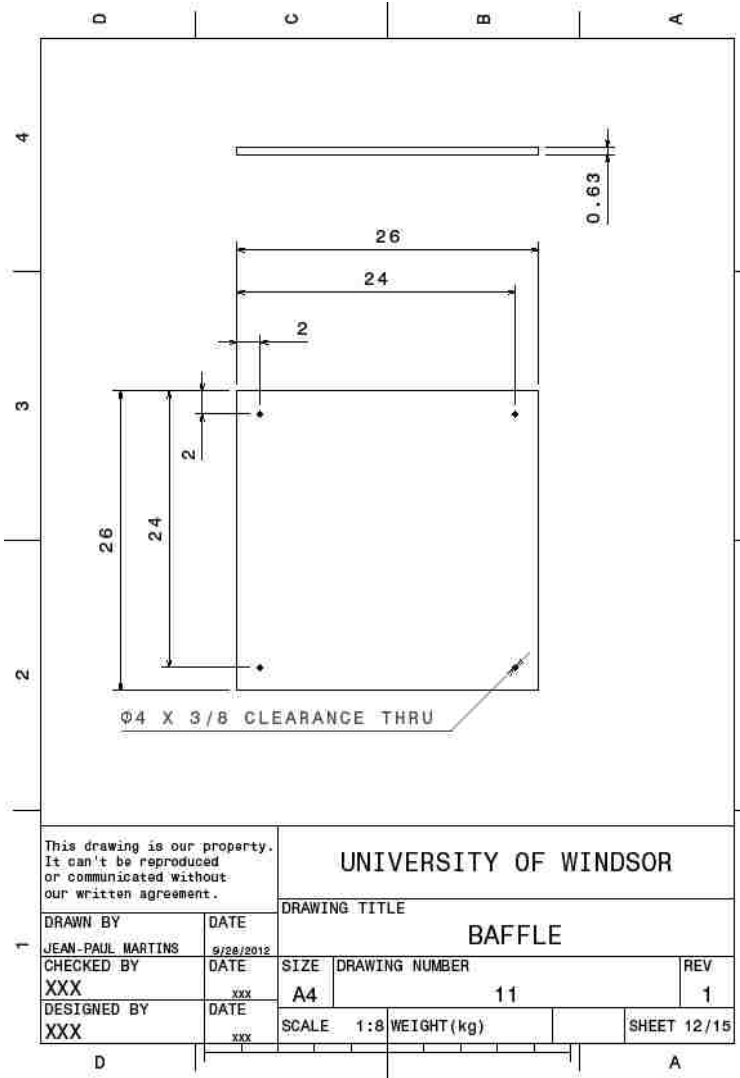**Figure B15: 2X2 Pillar**

90
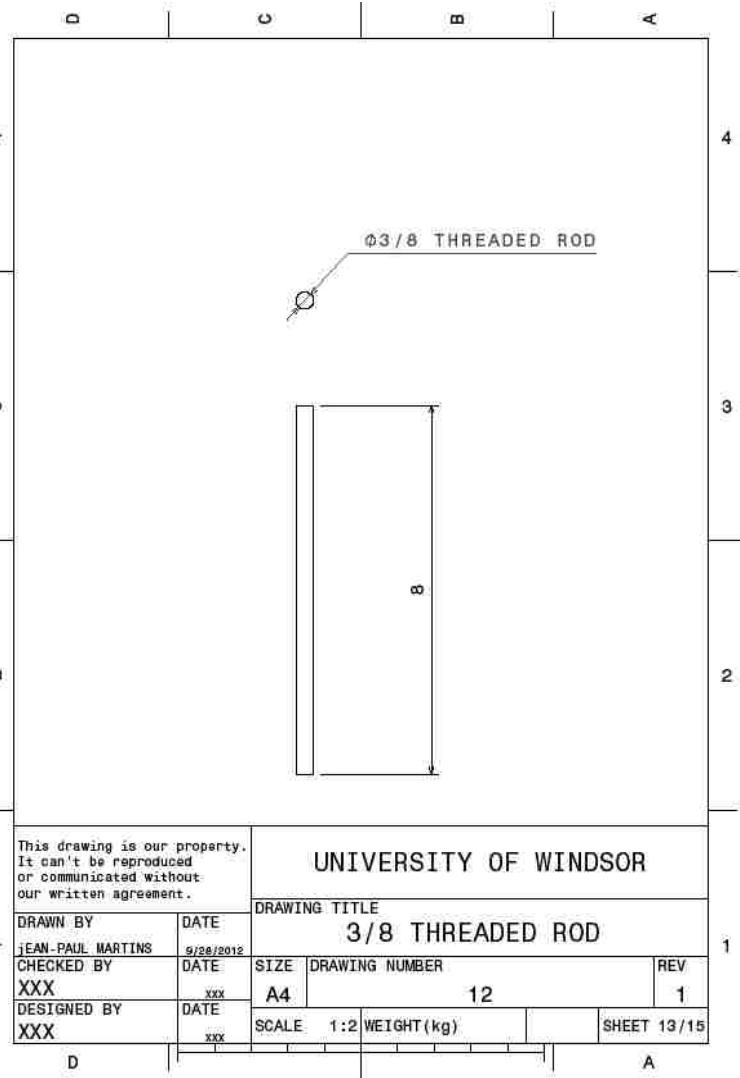
Figure B16: Baffle

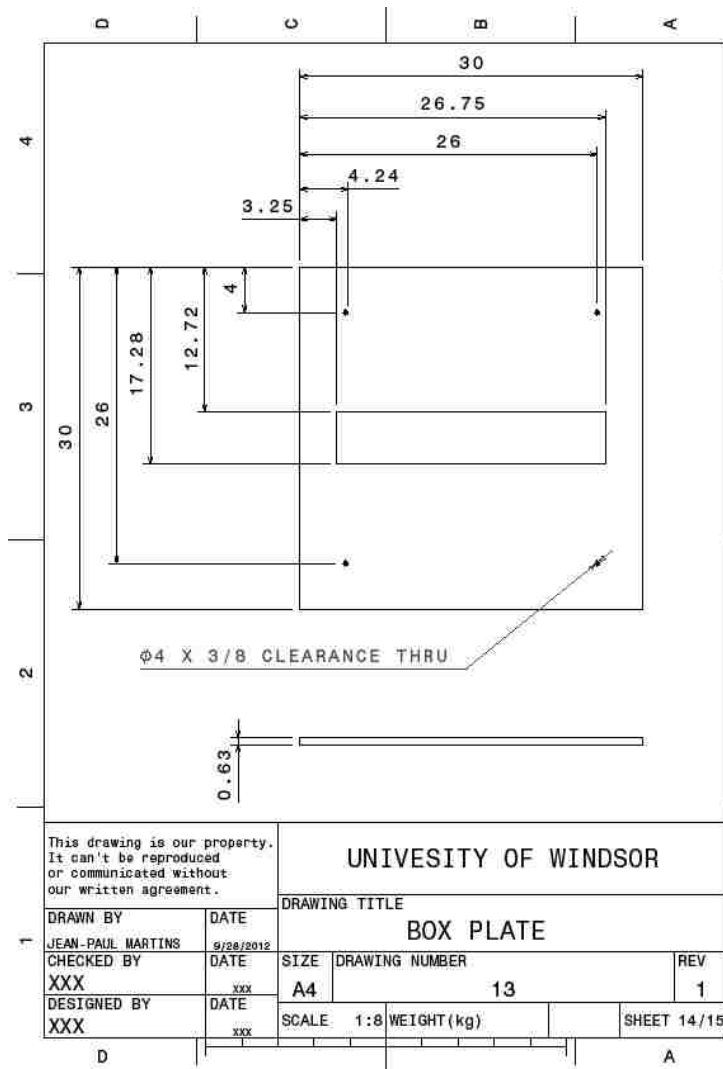**Figure B17: 3/8 Threaded Rod**
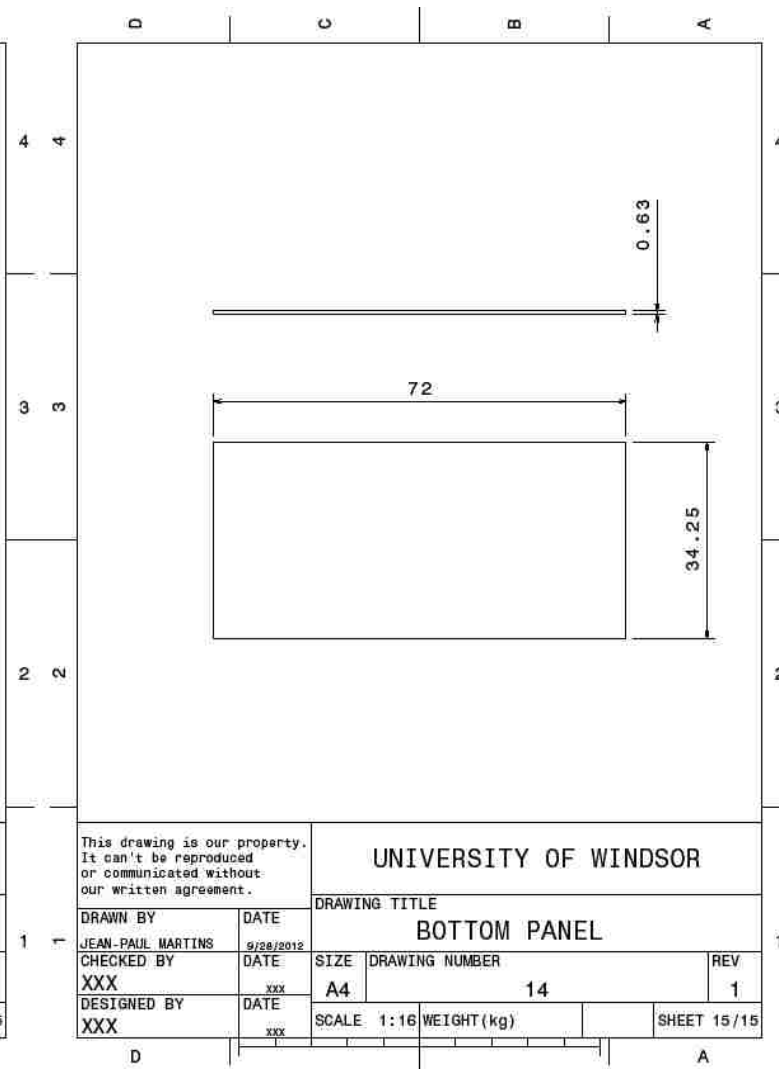
91

Figure B18: Box Plate

Figure B19: Bottom Panel

92

Appendix C Calculation of the Heat Transfer Coefficients

Empirical equations obtained from the literature are used to determine the heat transfer coefficient. Within this appendix, sample calculations are given for the determination of the heat transfer coefficients along with the required values. Procedures for calculating the heat transfer coefficient with example values are then presented for the cases of flow across the short and long direction of the produce containers.

C.1 Required Values

In order to complete the following sample calculations, certain material properties, geometrical characteristic lengths, and flow variables are required. The material properties are the thermal conductivity of the fluid and solid (air and cucumber) represented by k_f and k_s respectively as well as the specific heat at constant pressure, viscosity, and density of the working fluid represented by C_{pf}, μ_f, and ρ_f respectively. The geometrical parameters associated with the produce porous media model include the porosity given by the symbol φ, the particle diameter denoted by d_p and the shape factor for the flow aligned with the short and long directions across the produce containers given by β_{short}, $V_{avgshort}$ and β_{long}, respectively. The flow variable that needs to be specified is the area weighted average fluid velocity denoted by $V_{avglong}$. The particular values used for these quantities are as follows:

$$k_f = 0.0242 \frac{W}{m \cdot K} \qquad k_s = 0.6 \frac{W}{m \cdot K} \quad C_{pf} = 1006.43 \frac{J}{kg \cdot K} \quad \mu_f = 1.794 \times 10^{-5} \frac{kg}{m \cdot s}$$

$$\rho_f = 1.225 \frac{kg}{m^3} \qquad \varphi = 0.522 \qquad\qquad d_p = 0.043m \ \beta_{short} = 8$$

$$V_{avgshort} = 0.514 \frac{m}{s} \qquad\quad \beta_{long} = 6 \qquad V_{avglong} = 0.221 \frac{m}{s}.$$

C.2 Calculation of the Heat Transfer Coefficient in the Short Direction

First, it is required to calculate the particle Reynolds Number, with the air flowing across the short direction of the container, defined by Equation 8 from section2.6.6.

$$Re_p = \frac{\rho v d_p}{\mu} = \frac{(1.225 \frac{kg}{m^3})(0.514 \frac{m}{s})(0.04317m)}{1.794 \times 10^{-5} \frac{kg}{m \cdot s}} = 1519$$

Next, the Prandtl Number must be calculated.

$$Pr = \frac{C_{pf} \mu_f}{\rho_f} = \frac{(1006.43 \frac{J}{kg \cdot K})(1.794 \times 10^{-5} \frac{kg}{m \cdot s})}{(1.225 \frac{kg}{m^3})} = 0.7442$$

Once the Reynolds and Prandtl Numbers have been calculated, they can be used to determine the fluid solid Nusselt Number (Nu_{fs}) from Equation 17 in section 2.6.10. Recall the relationship used is the one presented by Handley and Heggs, since $Re > 80$.

$$Nu_{fs} = \frac{0.255}{\varphi} Pr^{1/3} Re_p^{2/3} = \frac{0.255}{0.5222}(0.7442)^{1/3}(1519.0561)^{2/3} = 58.47$$

From the fluid solid Nusselt Number the fluid to solid heat transfer coefficient (h_{fs}) can be determined using Equation 16 in section 2.6.10.

$$h_{fs} = \frac{Nu_{fs} k_f}{d_p} = \frac{(58.4761)(0.0242 \frac{W}{m \cdot K})}{(0.04317m)} = 32.78 \frac{W}{m^2 \cdot K}$$

Finally, the heat transfer coefficient can be calculated using Equation 15 from section 2.6.10.

$$\frac{1}{h^*} = \frac{1}{h_{fs}} + \frac{d_p}{\beta k_s} = \frac{1}{32.7802 \frac{W}{m^2 \cdot K}} + \frac{0.04317m}{(8)\left(0.6 \frac{W}{m \cdot K}\right)} = 0.0395 \frac{m^2 \cdot K}{W}$$

Thus the heat transfer coefficient (h^*) for the flow aligned with the short length of the containers, is 25.31 $\frac{W}{m^2 \cdot K}$ in the short direction.

C.3 Calculation of the Heat Transfer Coefficient in the Long Direction

The calculation procedure is the same as that for the short direction, except the area weighted average velocity ($V_{avglong}$) and shape factor (β_{long}) are different.

Appendix D User Defined Function for Initial Model

Within this appendix the User Defined Functions (UDFs) are explained, and then 7/8 cooling time UDF for use in the initial numerical model is described.

D.1 User Defined Functions Explained

ANSYS Fluent allows UDFs to be used to enhance the standard features of the solver. A UDF is written in the C computer language. Some additional macros are made available within the UDF language to simplify the functionality of the written C codes. The macros allow the code to be executed at the end of each iteration or time step, and upon exit or loading of the case. UDFs are advantageous when customized boundary conditions, property definitions, surface and volume reaction rates, and transport equations are required. The UDF can also be useful in the initialization of the model. They can be used to adjust computed values on a per iteration basis. Lastly, UDFs can be used to enhance post processing of the numerical models.

D.2 7/8 Cooling Time UDF for the Initial Numerical Model

In the initial User Defined Function the "DEFINE_PROPERTY" macro is used. This macro is applied to an entire material within the numerical model. In this specific case, it is applied to the density of the solid. Each time the density of the solid is used within the numerical solution, the UDF is executed. A flow chart describing the functioning of the UDF can be seen in Figure D1.
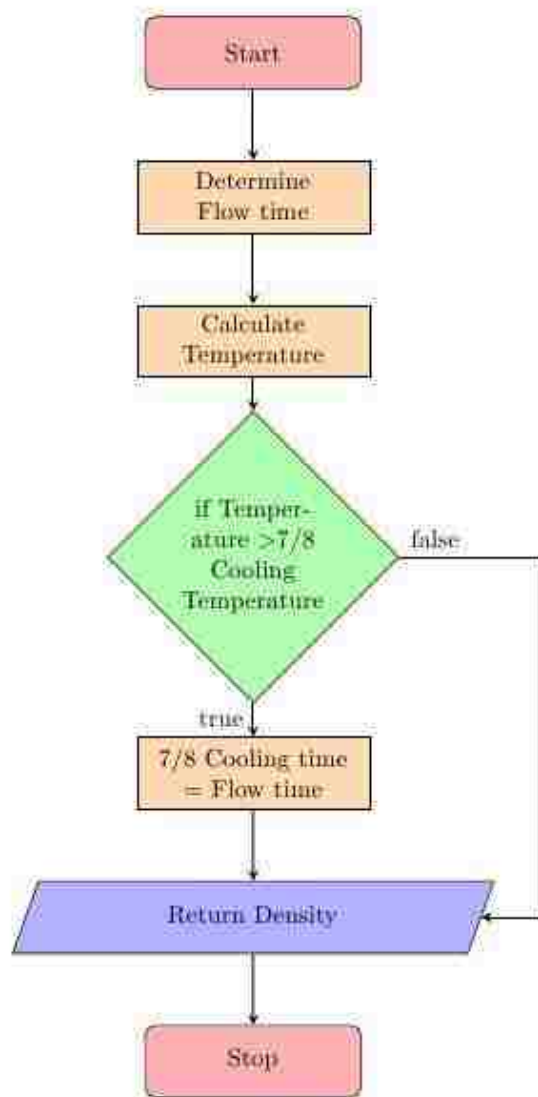
Figure D1: 7/8 Cooling Time Flowchart

The UDF begins by determining the flow time. The temperature of each cell is then determined. If the temperature of the cell is greater than the seven eights cooling temperature, the time in seconds is stored for that cell. If temperature is below the seven eights cooling temperature the time is not stored for that cell. The UDF terminates by

returning the density of the solid, which is constant. The C code used can be found in Figure D2 below.

```c
#include "udf.h"
DEFINE_PROPERTY(rho,cell,thread)
{
real t = CURRENT_TIME;
real rho=998.2;
real sect;
real temp = C_T(cell,thread);
if (temp >= 285.25)
{
sect = CURRENT_TIME;
C_UDMI(cell,thread,0)=sect;
}
return rho;
}
```

Figure D2: C Code Used for Initial Model UDF

Appendix E Fan Selection and Tunnel Design

The method used to select the cooling tunnel fan and other details of the tunnel construction are given in this appendix for completeness.

E.1 Fan Selection

In order to select a fan to ensure proper operation and sufficient cooling of the produce, rough estimates of the system requirements are made. In the case of forced air cooling of cucumbers, it is recommended that the airflow should be 1.5-0.5 cubic feet per minute (CFM) for every 1 pound (lb.) of agricultural product or 0.39-1.16 cubic meters per hour for every kilogram (kg) of product[29]. It is assumed that the small cucumber orientation of containers, seen in Figure E1, offer the largest resistance to flow, since that configuration has the largest number of porous jumps in series with the largest flow resistance. Hence, it is taken as the worst-case scenario for the system requirements. The use of the small cucumber arrangement is also beneficial due to its simple layout compared to other products. Since it has previously been seen that the produce offers negligible pressure drop compared to the container openings, the losses associated with the product are overlooked and the losses due to the containers only considered. It is also assumed that there is no flow between lanes of containers as there should not be any pressure gradients in that direction.

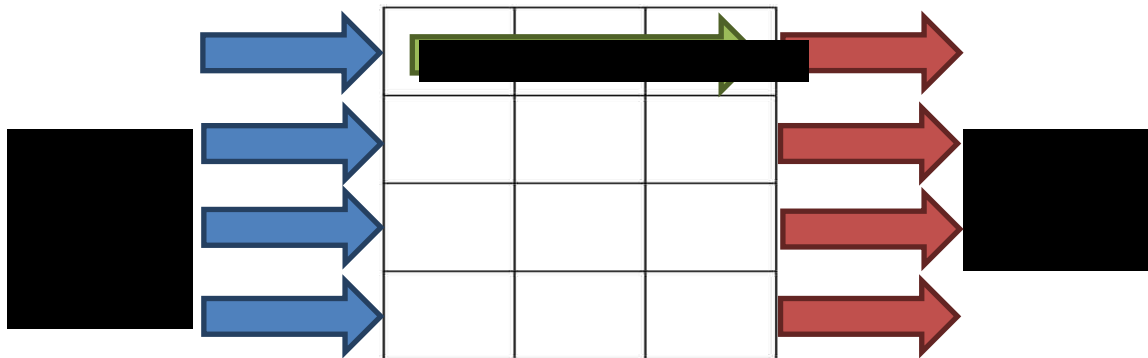**Figure E1: Airflow through a Single Lane of Containers**

First, it is required to estimate the total volume flow rate. This is done by knowing approximately the weight of cucumbers in each product container. Each product container is assumed to contain approximately 10 lbs. of cucumbers since there are 12 containers in each layer, 13 layers in each pallet, and 4 pallets of produce, the total

volume flow rate required is 6420 CFM ($3.03 m^3/s$). The midpoint of the suggested range of cooling flow rates per pound (1 CFM/lb) is used in the calculation. The superficial velocity can be determined by dividing the volume flow rate going through one lane of containers by the cross-sectional area of the container (0.108 m x 0.2826 m) which gives 0.464 m/s. The pressure drop equation through a single lane of product containers is the sum of the pressure losses associated to the four container openings seen in Figure E1. Since all the pressure drops are identical and they are in series, the resulting equation for the total pressure drop is similar to a single container opening only with four times the length. In this specific case, the viscous and inertial resistances are $3.2285 \times 10^{-9} m^2$ and $7.0490 \times 10^4 m^{-1}$ respectively. The resulting pressure drop is 422.26Pa. This means the selection of the fan must be such that it can supply 6420 CFM ($3.03 m^3/s$) of air at a pressure of 422.26 Pa (1.695 inches of water). A Twin City Fan and Blower Company fan with part number WPD-24-E8-24 is selected. The pump curve along with the system curve is presented in Figure E2.
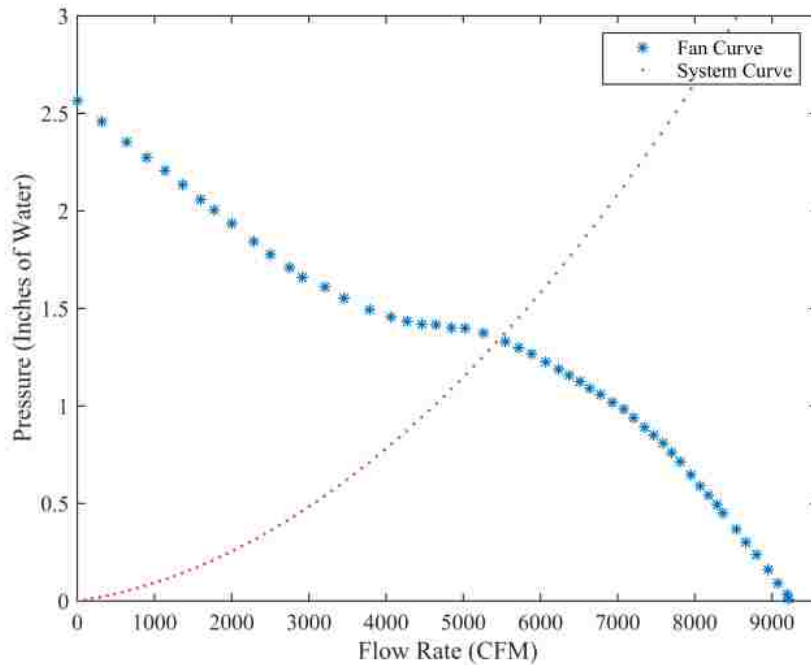

Figure E2 Fan and System Curves

From the figure, it is clear that the fan will not be able to achieve 6420 CFM ($3.03 m^3/s$) at 1.695 inches of water (422.26 Pa), but rather it will be able to achieve around 5500 CFM ($2.6 m^3/s$) at close to 1.5 inches of water (373.68 Pa). If we substitute this value

99

into equation E1, we find the flow rate per pound of product is approximately 0.88 CFM/lb. $(0.68 m^3/s \cdot kg)$. , which is well above the suggested minimum airflow of 0.5 CFM/lb. Since this configuration is our worst-case scenario, all other products should obtain higher flow rates at lower pressures.

E.2 Cooling Tunnel Design

Knowing the dimensions of the selected axial flow fan, the cooling tunnel is designed. The assembly drawing, and detail drawings can be found on the following pages.
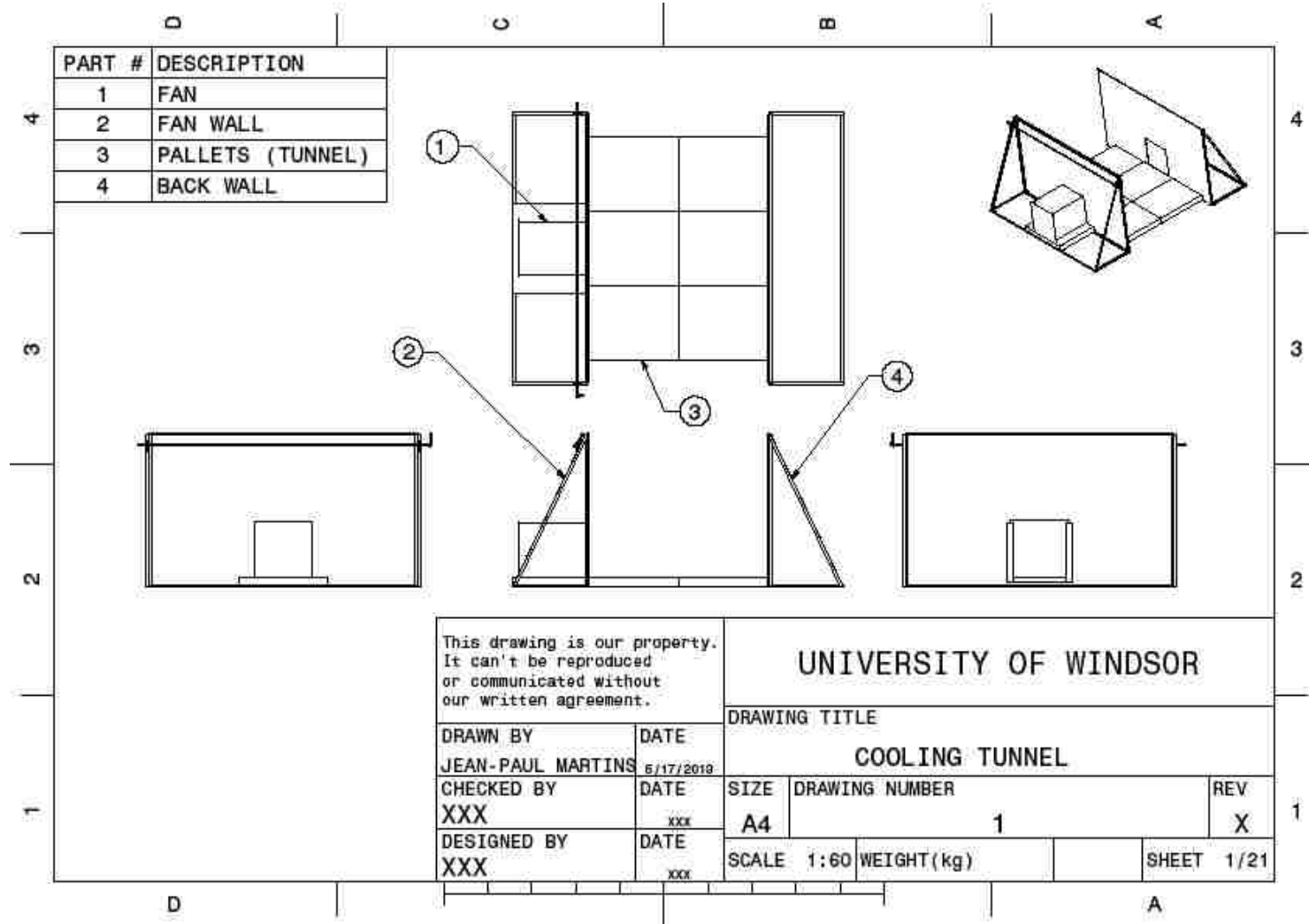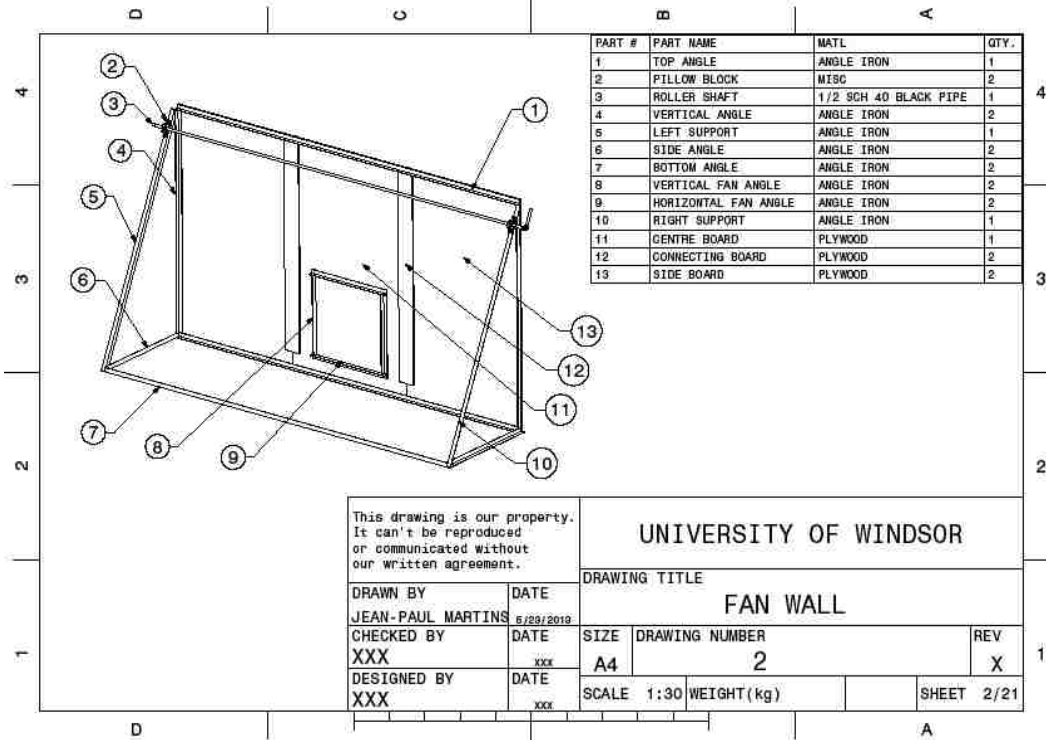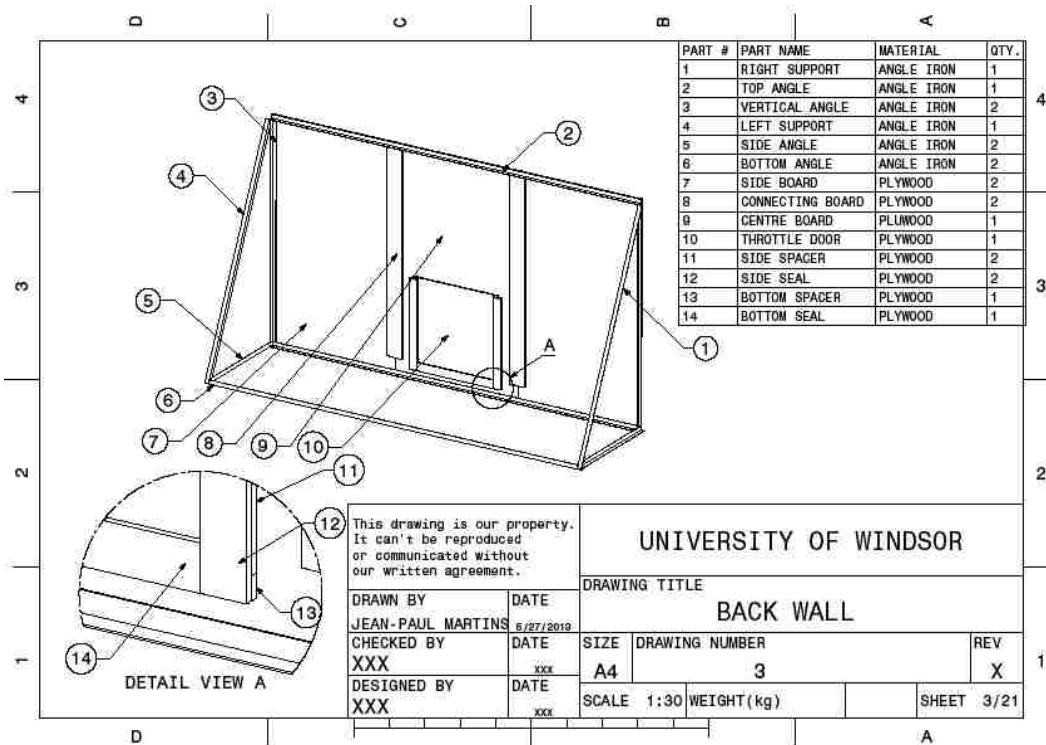
Figure E3: Cooling Tunnel Design

PART #	PART NAME	MATL	QTY.
1	TOP ANGLE	ANGLE IRON	1
2	PILLOW BLOCK	MISC	2
3	ROLLER SHAFT	1/2 SCH 40 BLACK PIPE	1
4	VERTICAL ANGLE	ANGLE IRON	2
5	LEFT SUPPORT	ANGLE IRON	1
6	SIDE ANGLE	ANGLE IRON	2
7	BOTTOM ANGLE	ANGLE IRON	2
8	VERTICAL FAN ANGLE	ANGLE IRON	2
9	HORIZONTAL FAN ANGLE	ANGLE IRON	2
10	RIGHT SUPPORT	ANGLE IRON	1
11	CENTRE BOARD	PLYWOOD	1
12	CONNECTING BOARD	PLYWOOD	2
13	SIDE BOARD	PLYWOOD	2

UNIVERSITY OF WINDSOR

DRAWING TITLE

FAN WALL

This drawing is our property.
It can't be reproduced
or communicated without
our written agreement.

DRAWN BY	DATE			
JEAN-PAUL MARTINS	5/29/2019			
CHECKED BY	DATE	SIZE	DRAWING NUMBER	REV
XXX	XXX	A4	2	X
DESIGNED BY	DATE	SCALE 1:30 WEIGHT(kg)		SHEET 2/21
XXX	XXX			

Figure E4: Fan Wall

PART #	PART NAME	MATERIAL	QTY.
1	RIGHT SUPPORT	ANGLE IRON	1
2	TOP ANGLE	ANGLE IRON	1
3	VERTICAL ANGLE	ANGLE IRON	2
4	LEFT SUPPORT	ANGLE IRON	1
5	SIDE ANGLE	ANGLE IRON	2
6	BOTTOM ANGLE	ANGLE IRON	2
7	SIDE BOARD	PLYWOOD	2
8	CONNECTING BOARD	PLYWOOD	2
9	CENTRE BOARD	PLUWOOD	1
10	THROTTLE DOOR	PLYWOOD	1
11	SIDE SPACER	PLYWOOD	2
12	SIDE SEAL	PLYWOOD	2
13	BOTTOM SPACER	PLYWOOD	1
14	BOTTOM SEAL	PLYWOOD	1

UNIVERSITY OF WINDSOR

DRAWING TITLE

BACK WALL

This drawing is our property.
It can't be reproduced
or communicated without
our written agreement.

DETAIL VIEW A

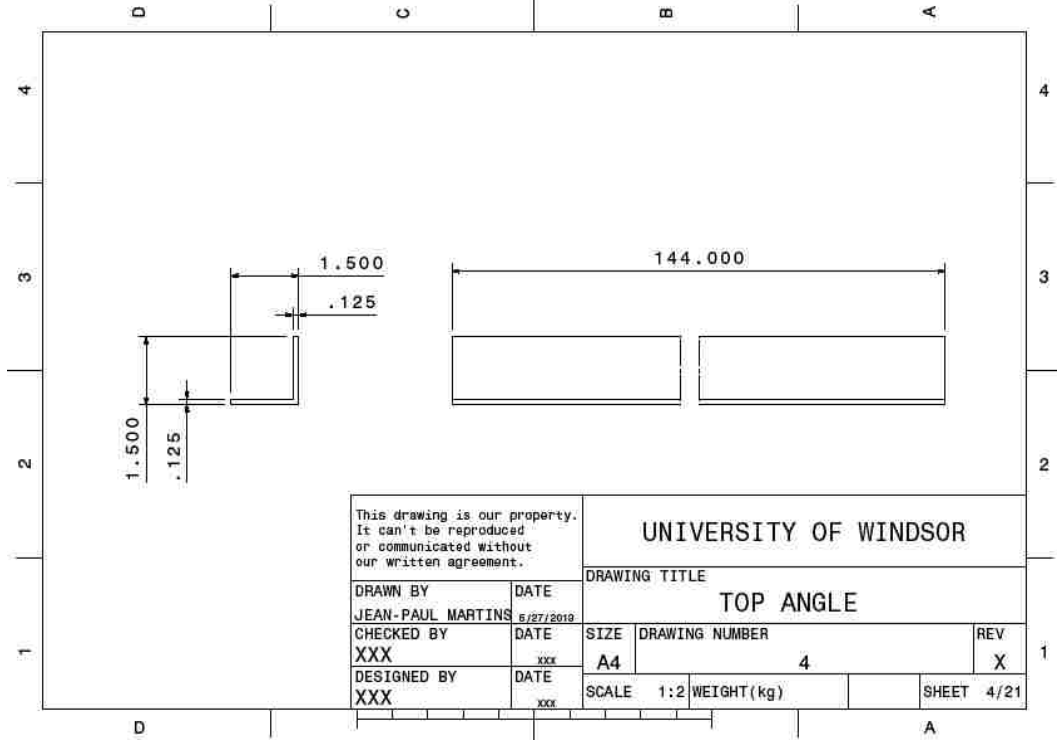| DRAWN BY	DATE			
JEAN-PAUL MARTINS	5/27/2019			
CHECKED BY	DATE	SIZE	DRAWING NUMBER	REV
XXX	XXX	A4	3	X
DESIGNED BY	DATE	SCALE 1:30 WEIGHT(kg)		SHEET 3/21
XXX	XXX			

Figure E5: Back Wall

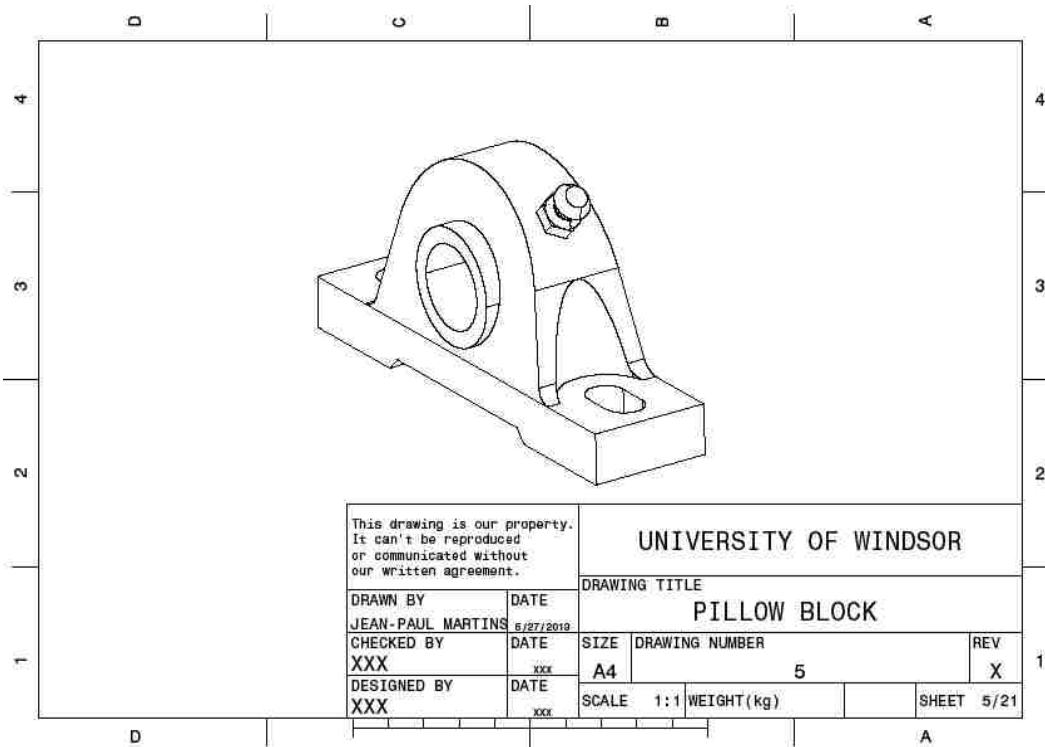102

Figure E6: Top Angle
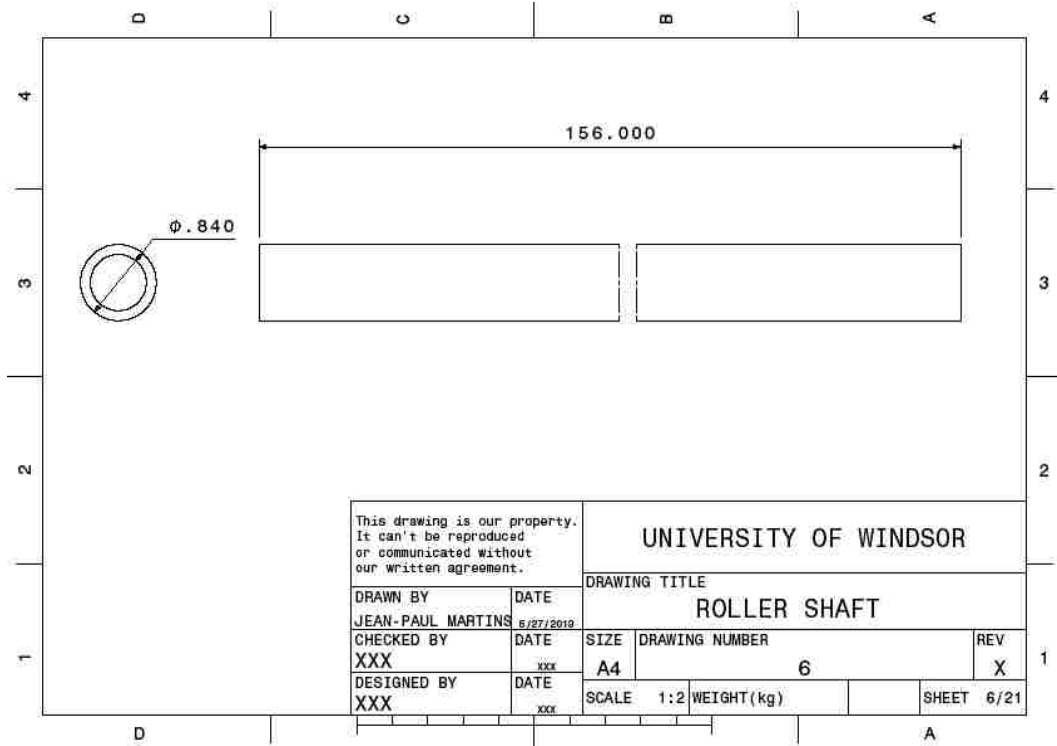

Figure E7: Pillow Block
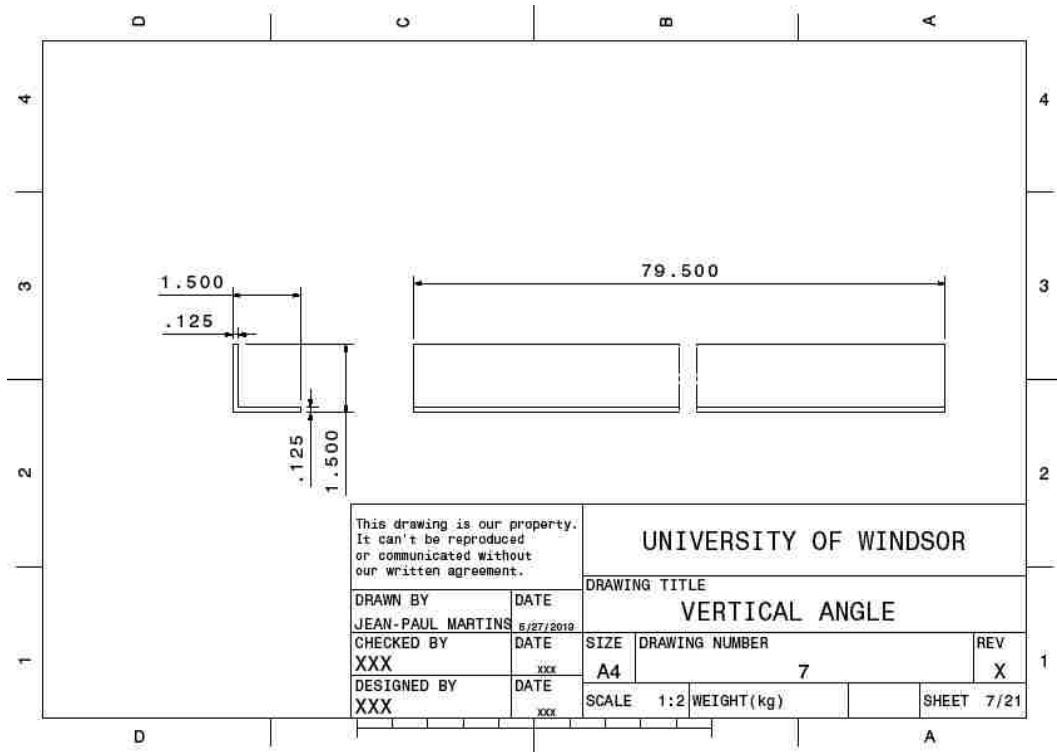
Figure E8: Roller Shaft
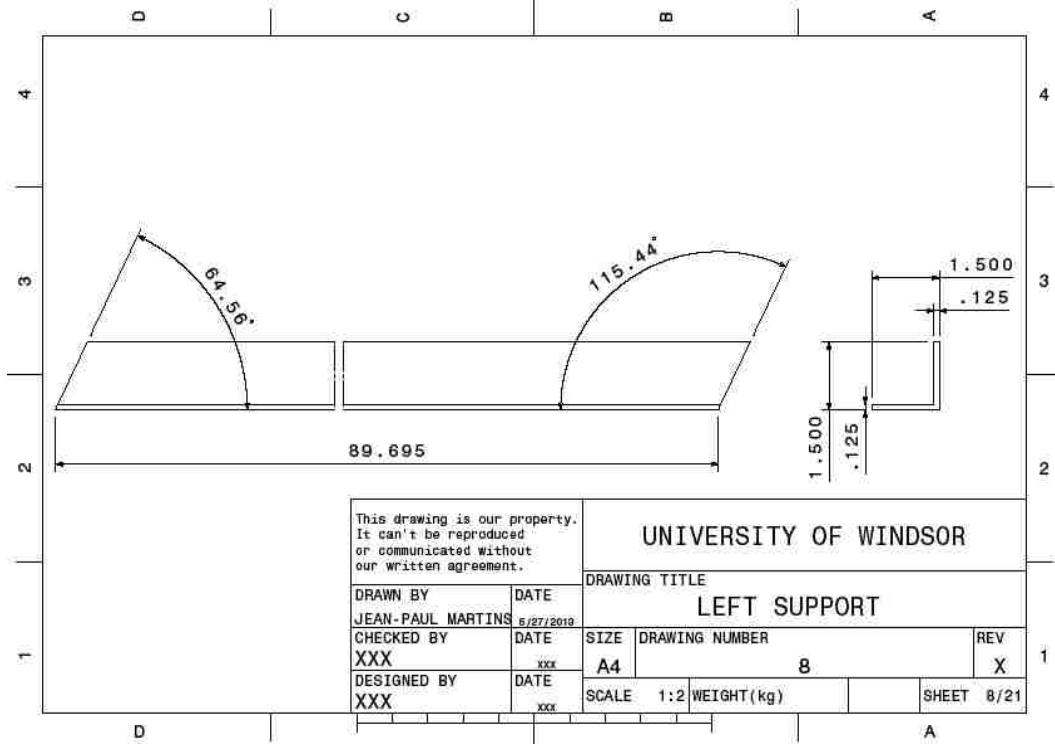

Figure E9: Vertical Angle
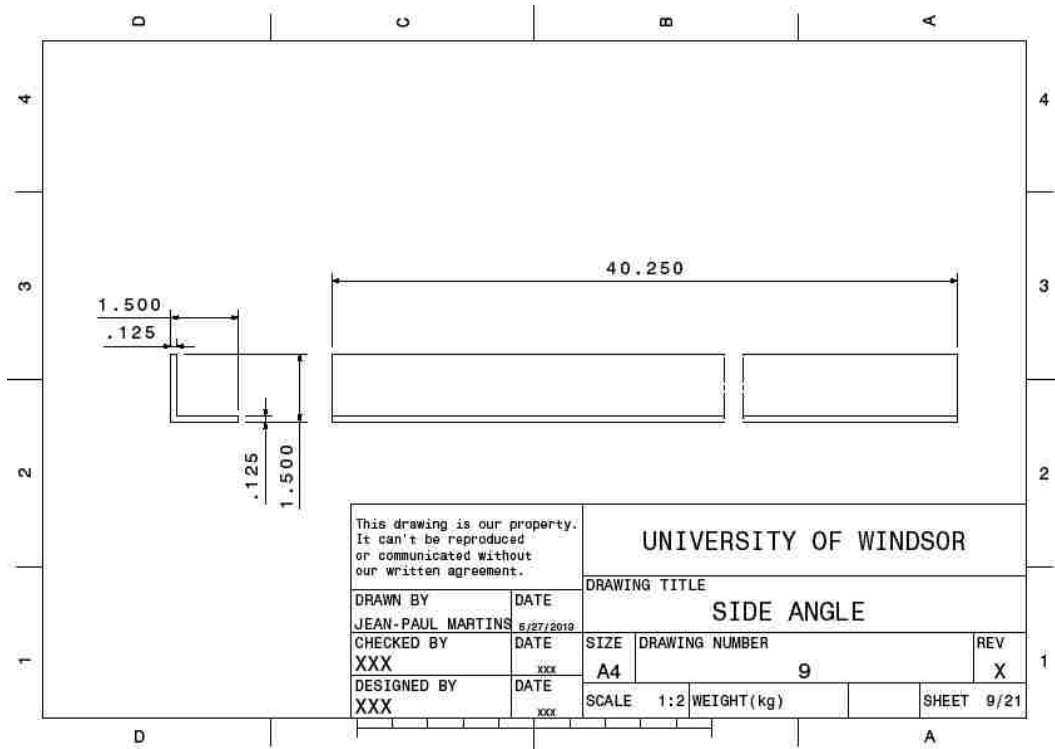
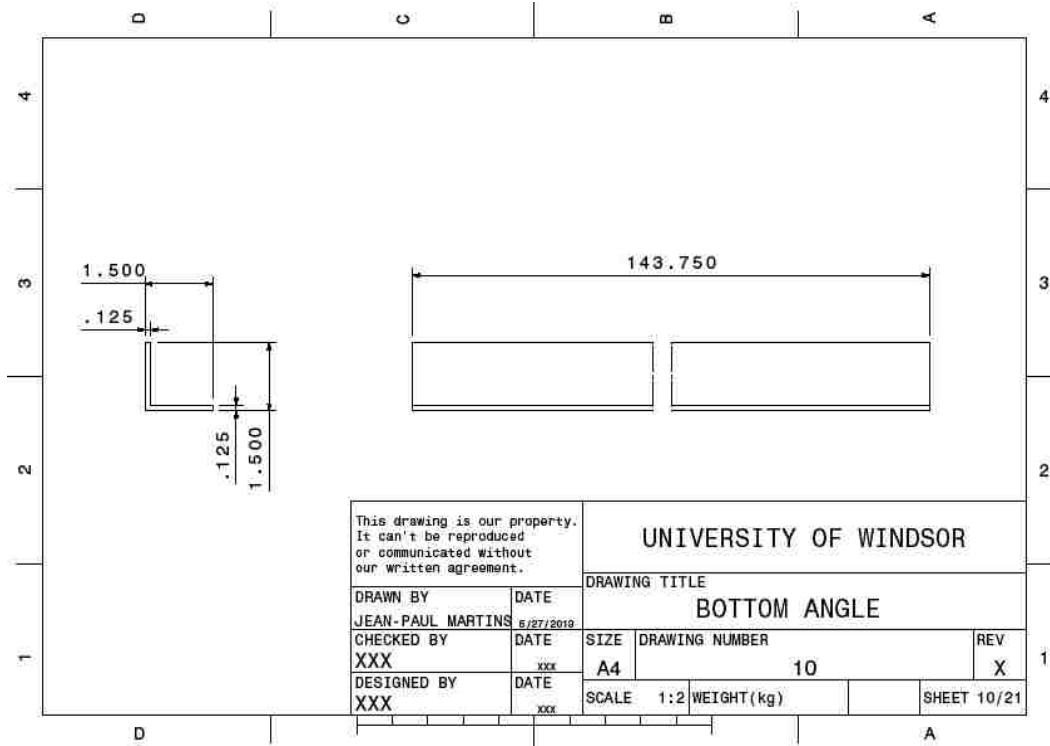**Figure E10: Left Support**

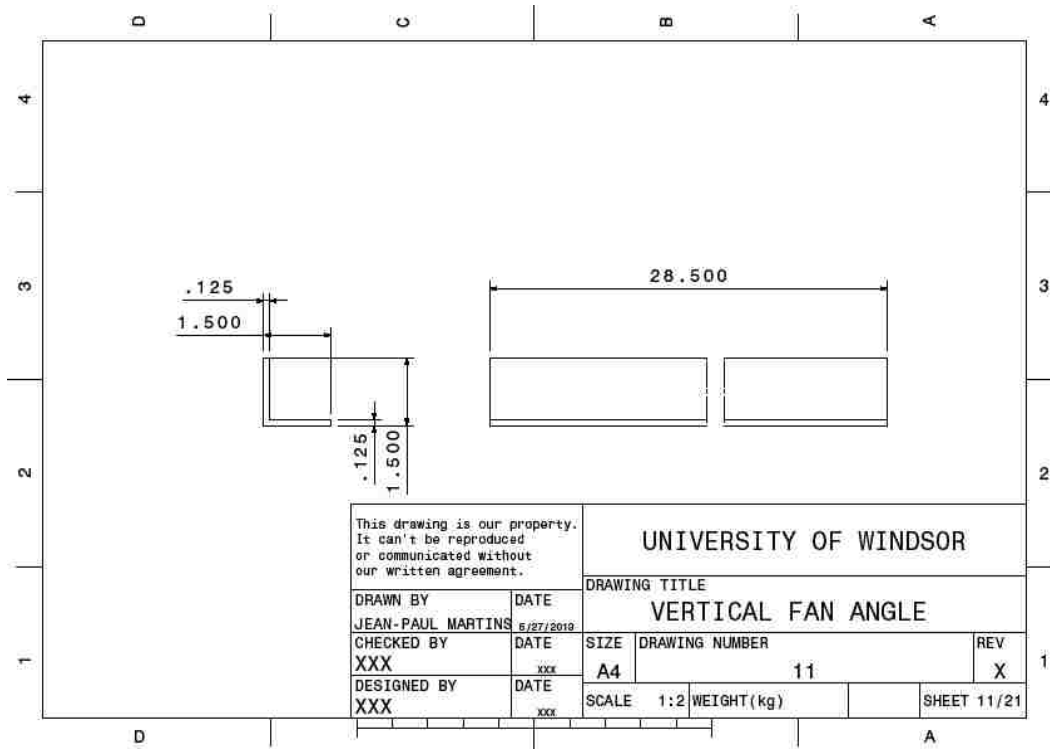**Figure E11: Side Angle**

Figure E12: Bottom Angle
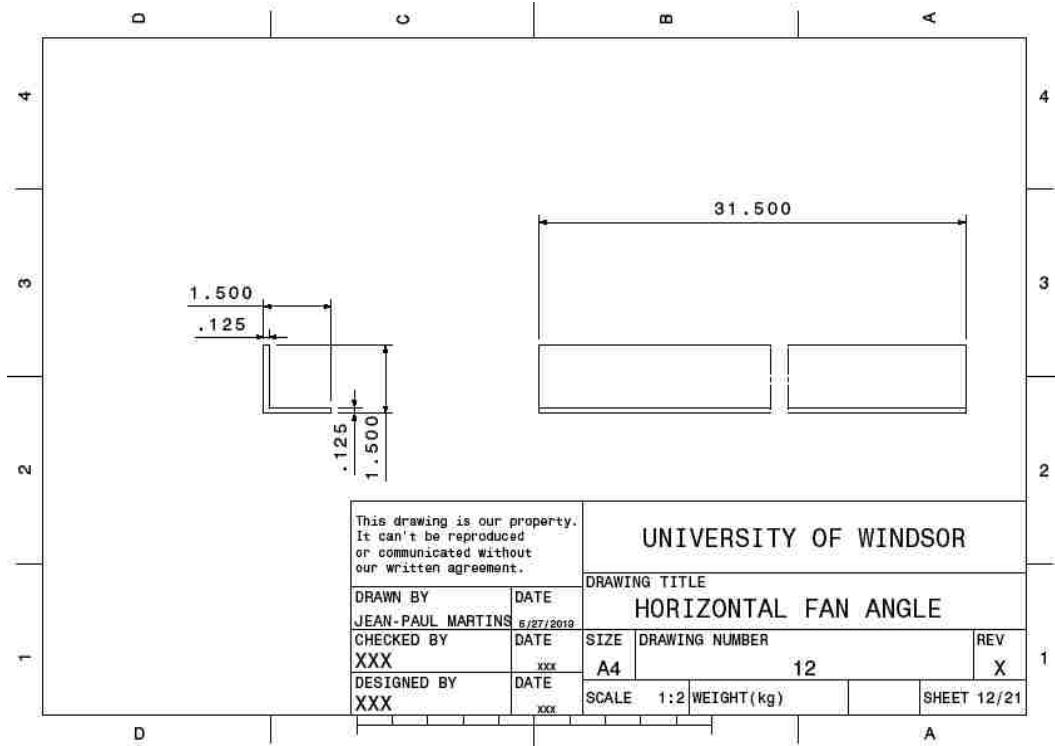

Figure E13: Vertical Fan Angle

106

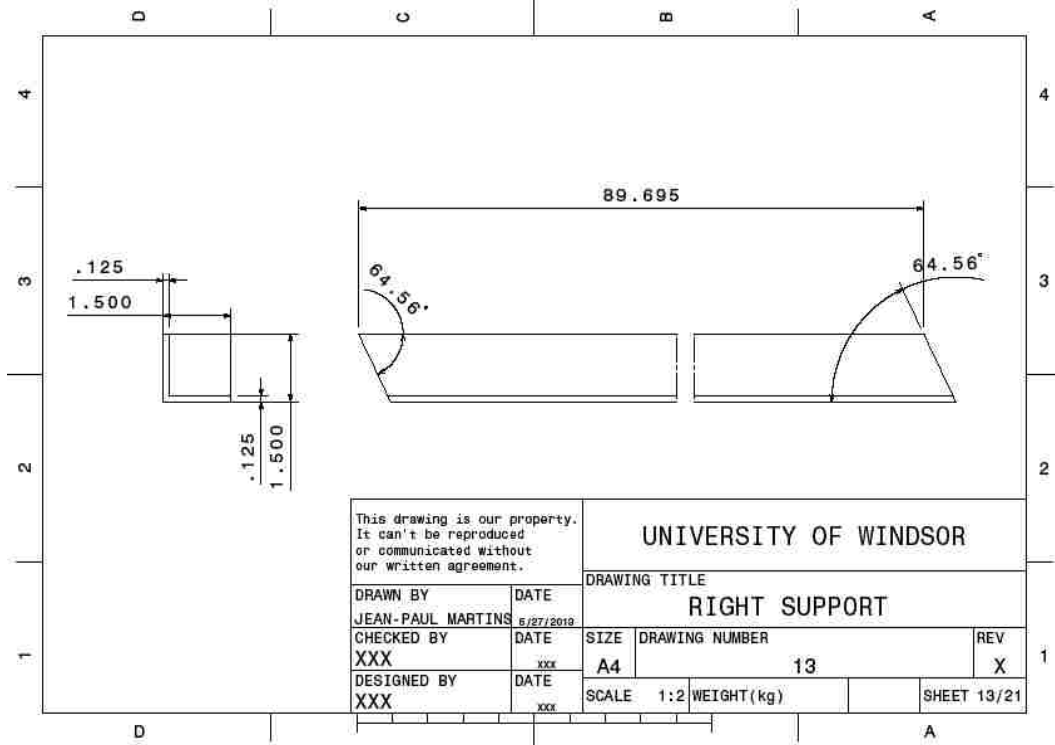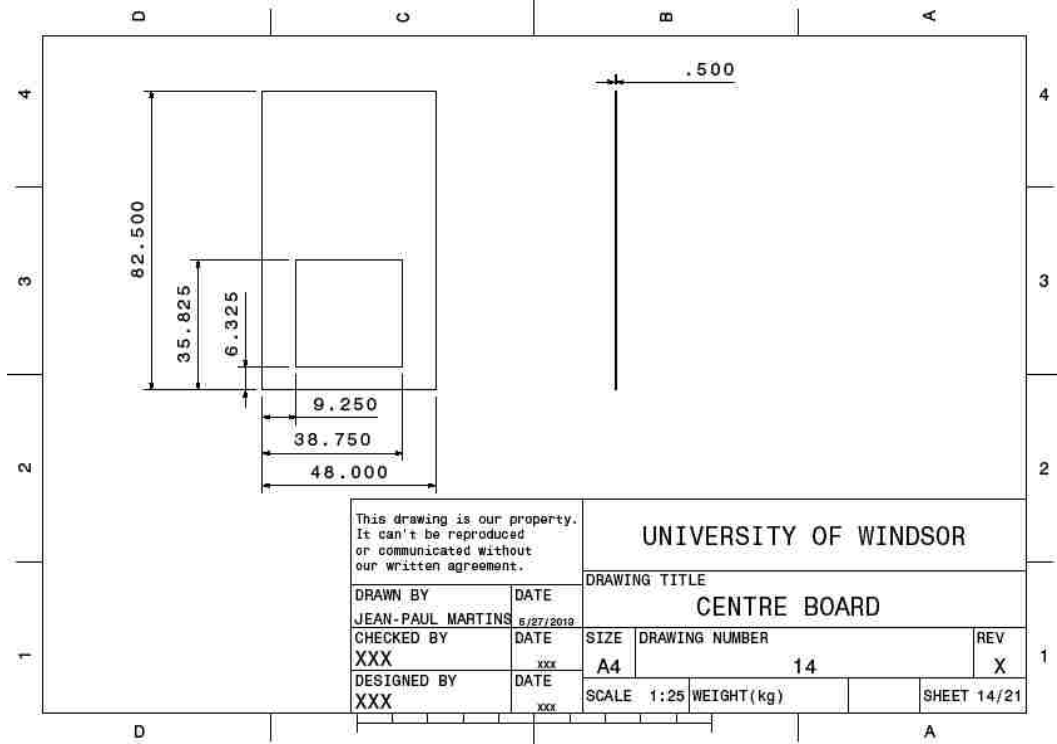**Figure E14: Horizontal Fan Angle**

Figure E15: Right Support

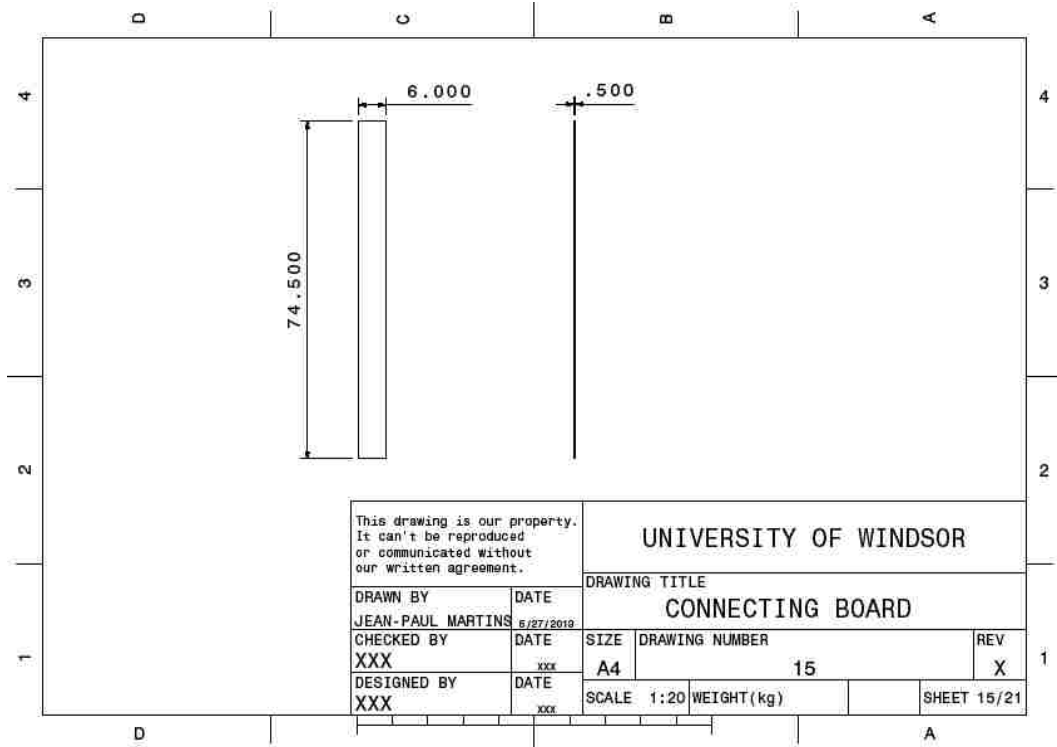**Figure E16: Centre Board**

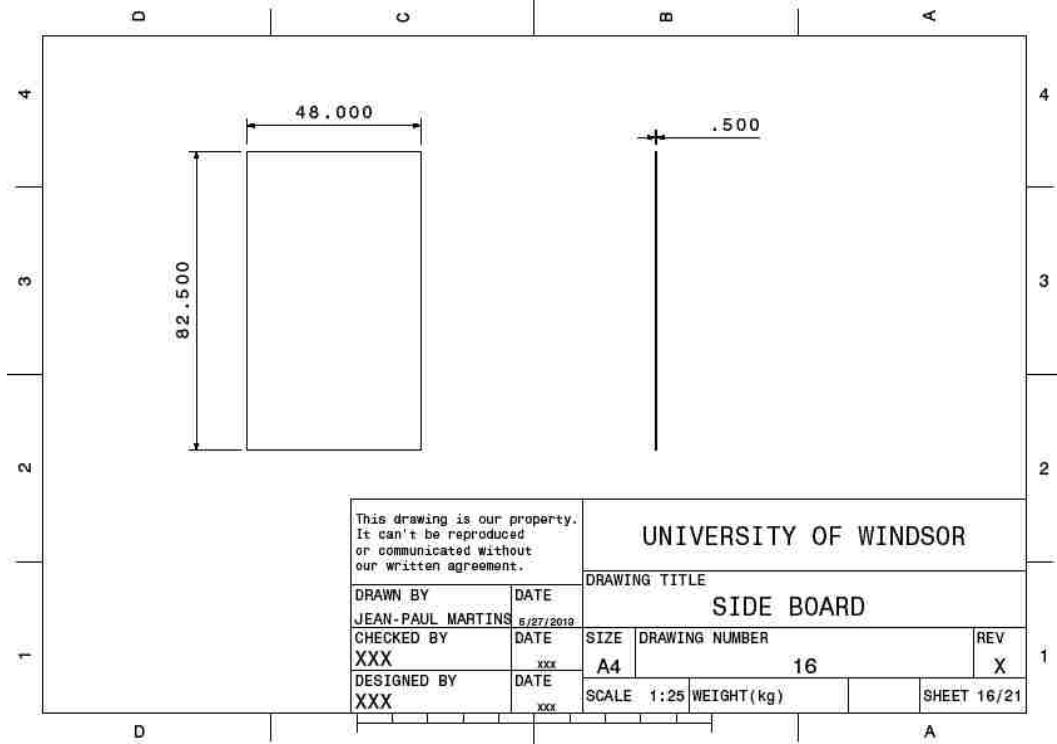**Figure E17: Connecting Board**
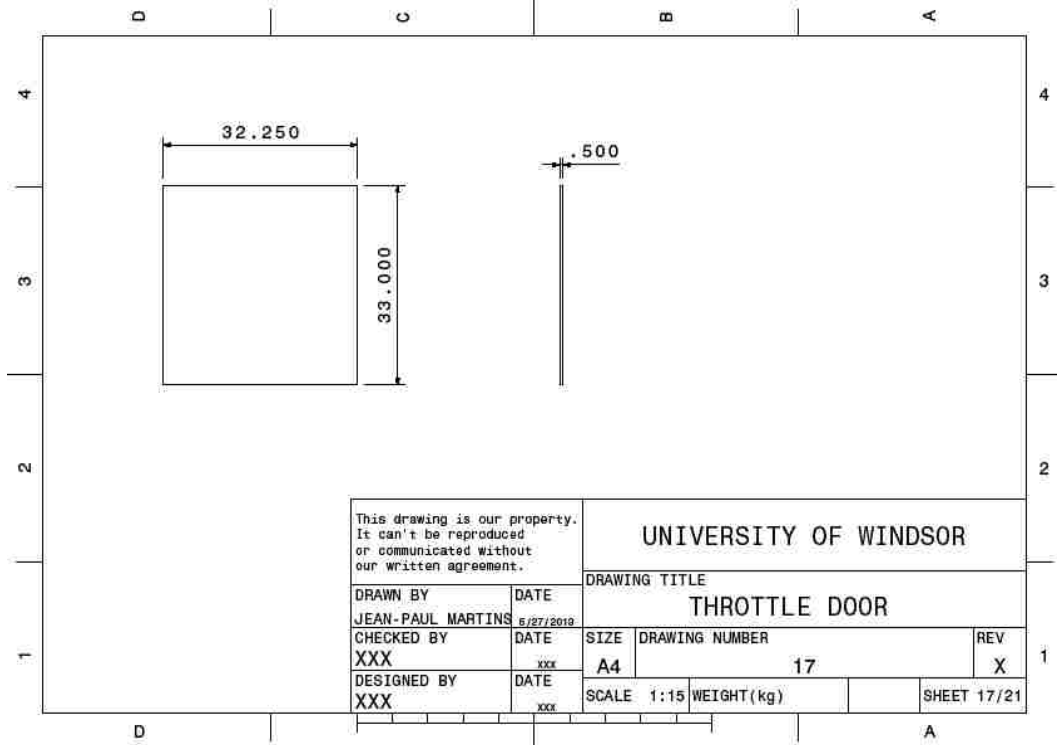
Figure E18: Side Board
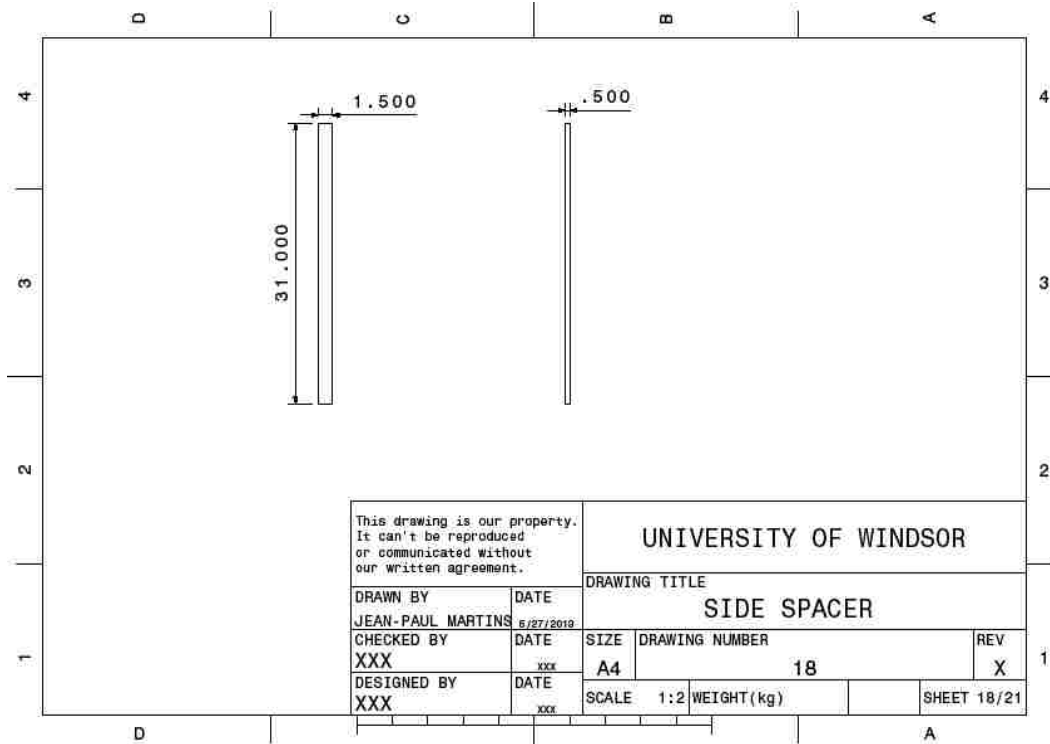

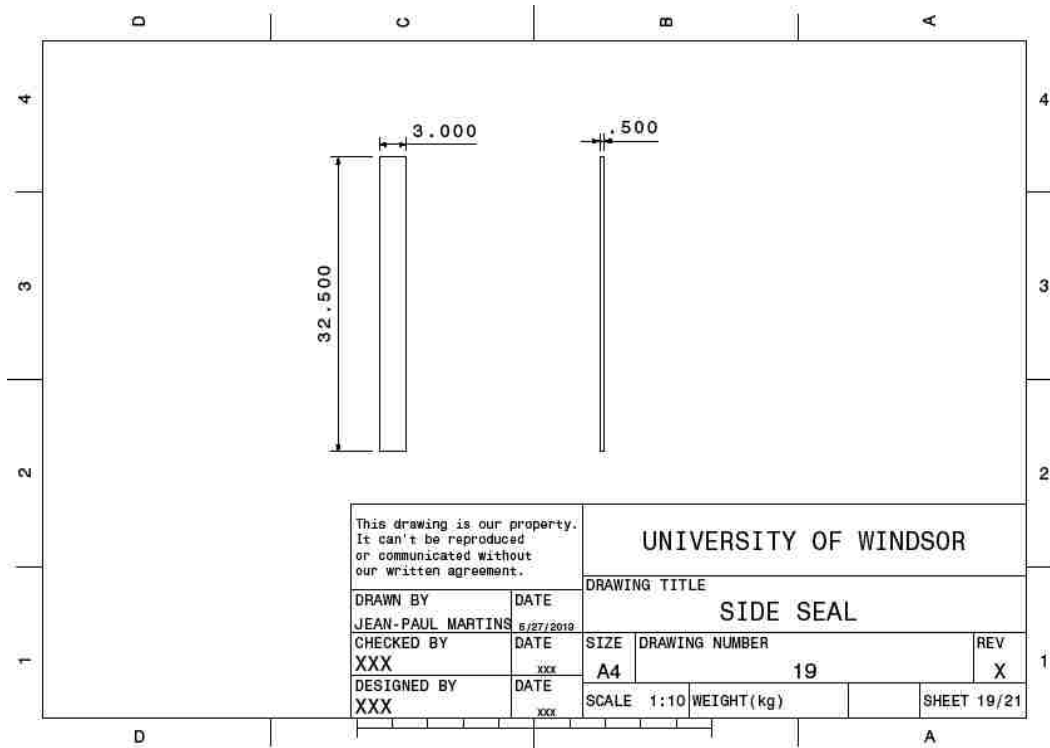**Figure E19: Throttle Door**

Figure E20: Side Spacer

Figure E21: Side Seal
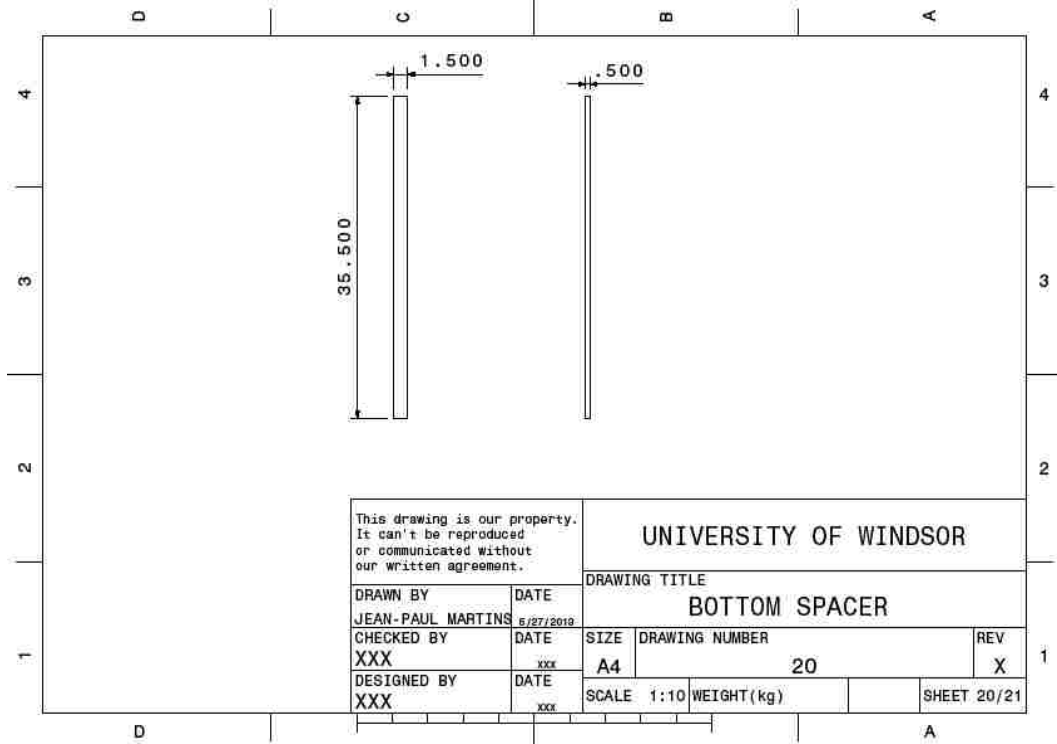
Figure E22: Bottom Spacer
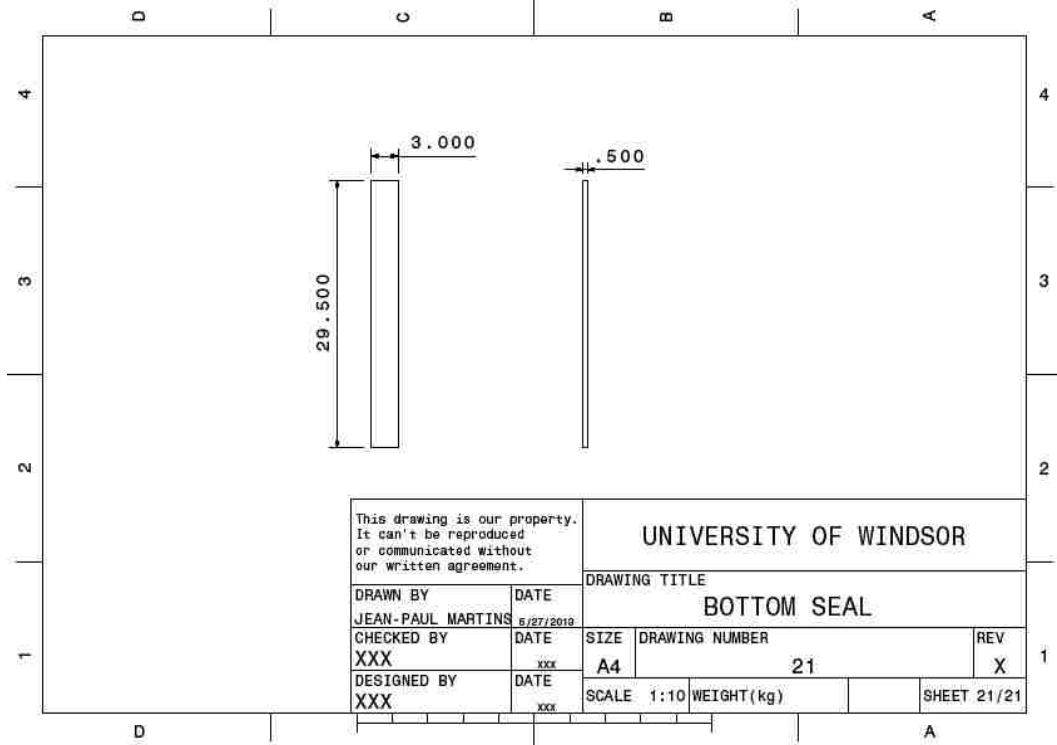
Figure E23: Bottom Seal

111

Appendix F Labview Data Acquisition Programs

National Instruments Labview is used to record and monitor the desired temperature data obtained in the experiments. In the front panel seen in Figure F1, four waveform charts each contain 8 waveforms which indicate the temperature of a given thermocouple in degrees Celsius. On the far right is the numerical value corresponding to each thermocouple. The average temperature of the 32 thermocouples is displayed as well as the amplitude of each of waveform chart. A stop button can be found on the far left, which terminates the Data Acquisition process. Finally, a save button and save indicator are present in order to save the data.
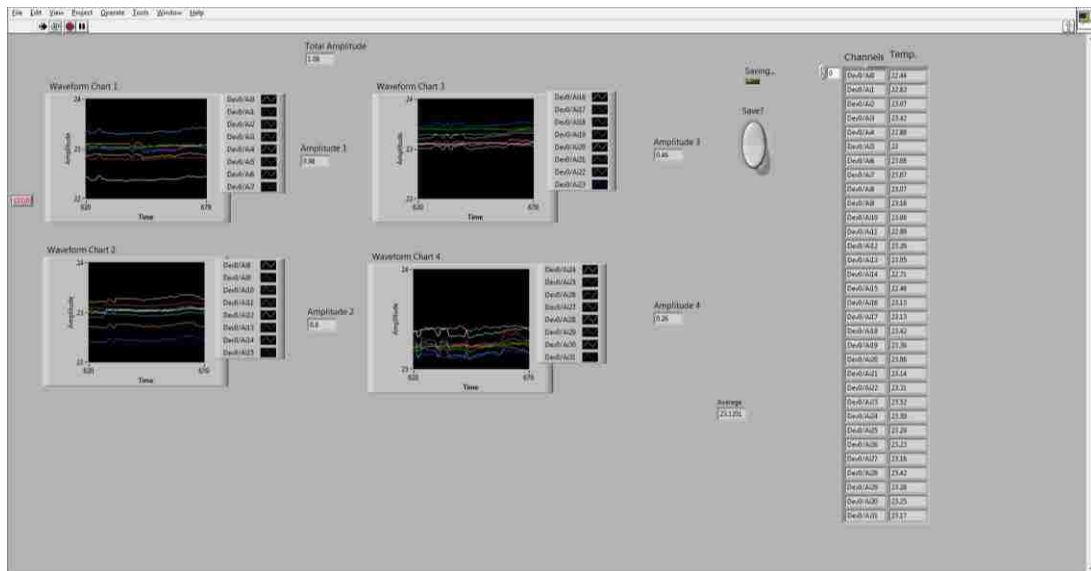
Figure F1: Labview Front Panel

The block diagram for the Virtual Instrument (VI) can be seen in Figure F2. It is constructed within a while loop which begins when the VI is set to run and terminated when the stop button is pressed. The while loop operates on a 5 second time delay seen in the figure. The Data comes in 8 channels at a time via a sub VI block and is transmitted on the brown wires, to the waveform chart blocks, amplitude analyzer blocks, and signal combiner block. Once the data enters the signal combiner all 32 channels of data are combined and can be sent down a single blue wire. The data is then sent to the "temp" block and "average temp" block for digital display on the front panel. The data is also

sent to the write to measurement file block that saves all the data into an Excel sheet. Finally, the pink string blocks are present in order to keep track of the data coming from each channel.
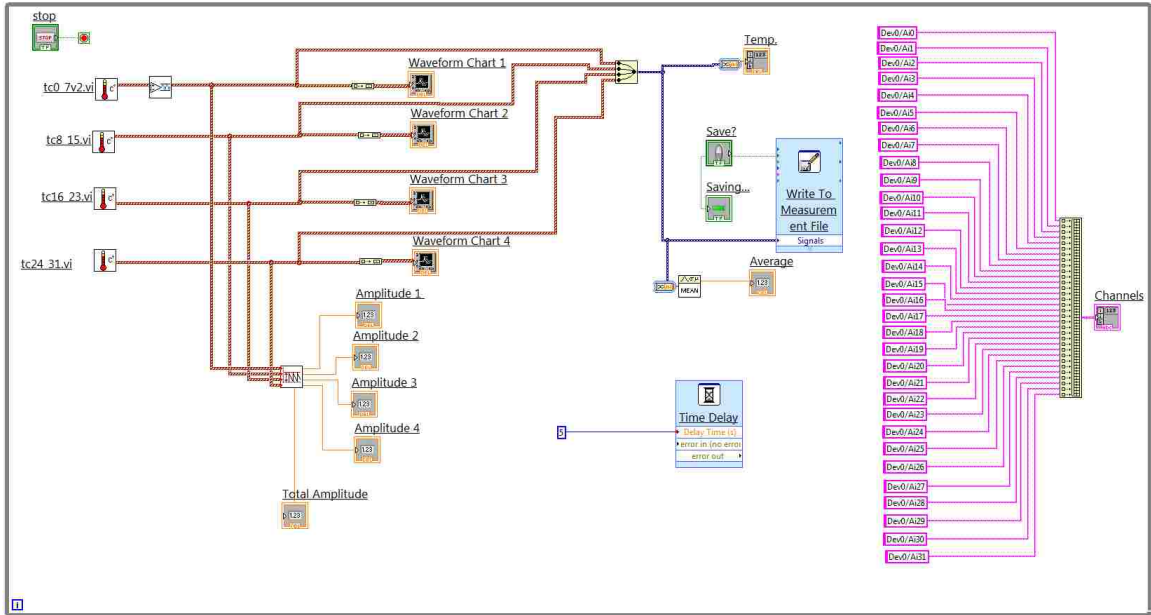
Figure F2: Labview Block Diagram

The sub VI block diagram is shown in Figure F3, and is required to read the data from the multifunction DAQ . The purple IO block indicates which channels to be scanned for analog data. The data then passes into a Read block and is output on the brown wire to a waveform graph and converted into an array data type. Finally, it passes to a write block and is checked for errors.

Figure F3: Labview Sub VI

Appendix G Uncertainty Analysis

Within this section, equations used to determine the uncertainty of measurements are presented. The methodology for determining the uncertainty of the dimensionless pressure and temperature measurements are also given.

G.1 Design Stage Uncertainty

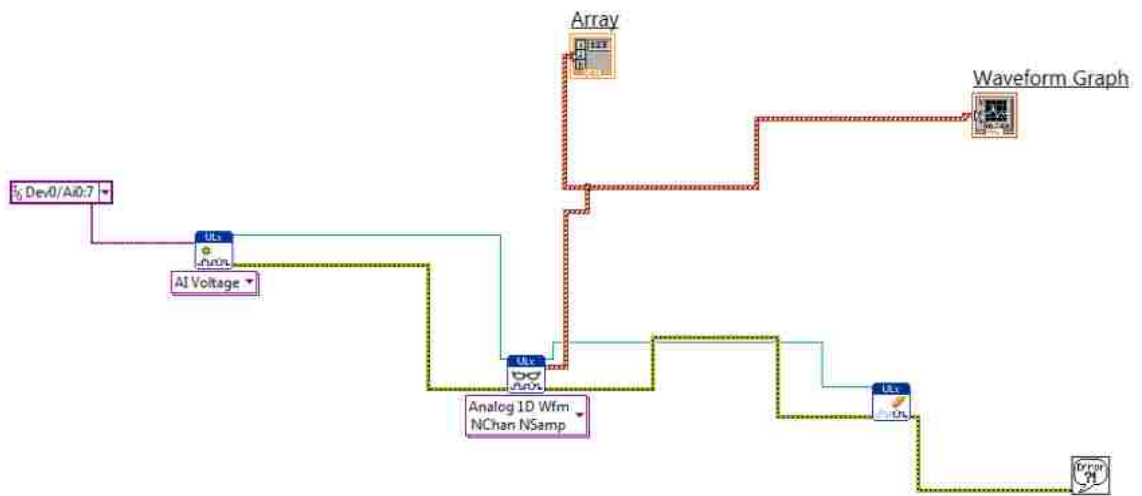In general the uncertainty in the measurement given by the device is called the design stage uncertainty and given by equation G1[30].

$$U_d = \sqrt{U_o^2 + U_c^2} \tag{G1}$$

In Equation G1, U_o corresponds to the zero order uncertainty given by Equation G2, and U_c corresponds to instrument errors defined by Equation G3.

$$U_o = \frac{1}{2} \; instrument \; scale \; resolution \tag{G2}$$

$$U_c = \sqrt{\sum_{i=1}^{N} e_i^2} \tag{G3}$$

In equation G3, e_i represents the errors listed by the manufacturer with the index i given since there may be more than one.

G.2 Uncertainty of Functions Composed of Independent Variables

In the case where the uncertainty of a function composed of multiple independent variables is required (i.e. $R = R(x_1, x_2, x_3, \ldots, x_n)$), the equation proposed by Kline and McClintock is used shown in Equation G4 [31].

$$U_R = \sqrt{\left(\frac{\partial R}{\partial x_1} U_1\right)^2 + \left(\frac{\partial R}{\partial x_2} U_2\right)^2 + \cdots + \left(\frac{\partial R}{\partial x_n} U_n\right)^2} \tag{G4}$$

In Equation G4 U_i denotes the uncertainty of each independent variable.

G.3 Uncertainty in Pressure

The design stage uncertainty of the measurements taken with the HHP-103 handheld manometer is determined to be ±0.0201 inches of water (±5 Pa). The zero order error is determined from the device resolution of 0.001 inches of water. The manufacturer's specification of 0.2 % of high scale range of 10.04 inches of water for is used for the instrument error. It is assumed that the error due to the spatial variation of the pressure inside the containers, and the unknown exact orientation of the pressure tap is equal to the

design stage uncertainty. The total uncertainty in the pressure is determined to be ±0.0284 inches of water (±7Pa).

G.4 Uncertainty in Dimensionless Vacuum Pressure

To determine the uncertainty in the dimensionless vacuum pressure we must recall Equation 26 restated as Equation G5.

$$P^* = \frac{P - P_{min}}{P_{max} - P_{min}} \tag{G5}$$

During the experimental investigation, pressures are measure using the HHP-103 handheld manometer. This specific manometer takes differential pressure measurements; thus, one port on the handheld manometer is always open to the pressure in the room, which corresponds to P_{min}. The dimensionless vacuum pressure is therefore composed of two measurements. The numerator of equation G1 corresponds to any pressure measured within the flow field, and similarly the denominator represents the maximum pressure measured within the flow field. In the specific application of tunnel forced air cooling of produce, the maximum pressure always occurs in the tunnel.

Equation J4 is used with equation J5 to calculate the uncertainty in the dimensionless vacuum pressure. The minimum uncertainty in the dimensionless pressure is determined to be ±0.051with the lowest measured pressure of 0 inches of water (0 Pa). Similarly, the maximum uncertainty is determined to be ±0.088 from the maximum measured pressure of -0.455 inches of water (-113.25 Pa).

G.5 Uncertainty in Temperature

The design stage uncertainty of the measurements taken with the USB-2416 is estimated to be ±0.487℃. The zero order error is determined based on the device resolution of 0.001℃. The instrument error is determined based on the manufacturer's specification of ±0.487℃. No other assumptions are made to increase the level of uncertainty of the temperature measurements; therefore, the total uncertainty in temperature is the same as the design stage uncertainty of ±0.487℃.

G.6 Uncertainty in Dimensionless Temperature

Equation G4 is used along with Equation 27 from the main text, stated below as Equation G6. From Equation G6 it can be seen that the resulting uncertainty of the

dimensionless vacuum pressure is a function of three variables: the initial temperature (T_i), the minimum room temperature (T_r), and the instantaneous temperature ($T(t)$).

$$\tau = \frac{T(t) - T_r}{T_i - T_r} \tag{G6}$$

The minimum uncertainty in the dimensionless temperature is determined to be ±0.047, occurring in the original configuration in location RM7. The maximum uncertainty in the dimensionless temperature is determined to be ±0.085, occurring at location RM10 in the experiment for the alternate configuration.

Appendix H UDF used to Initialize Product Temperatures

An Initialize UDF is written in order to initialize the product temperatures to those seen in the experiment. This is accomplished with the use of the DEFINE_INIT macro available in the ANSYS Fluent UDF library. The DEFINE_INIT macro ensured that the code is executed when the fluent case is initialized. The Initialize routine begins by patching the initial temperature of the room and saving it to a .txt file. It then loops through the product containers and patches the temperature in the container to be identical to that seen in the experiment. While looping through the product containers the program also calculates the seven eights and half-cooling temperatures of each container for future use. The initial temperature of each container is also saved in a .txt file within the loop. Once the program has looped through all the product containers, the program terminates. A flow chart describing the behavior of the UDF code can be seen in Figure H1. Finally, the C code used can be found in Figure H2.
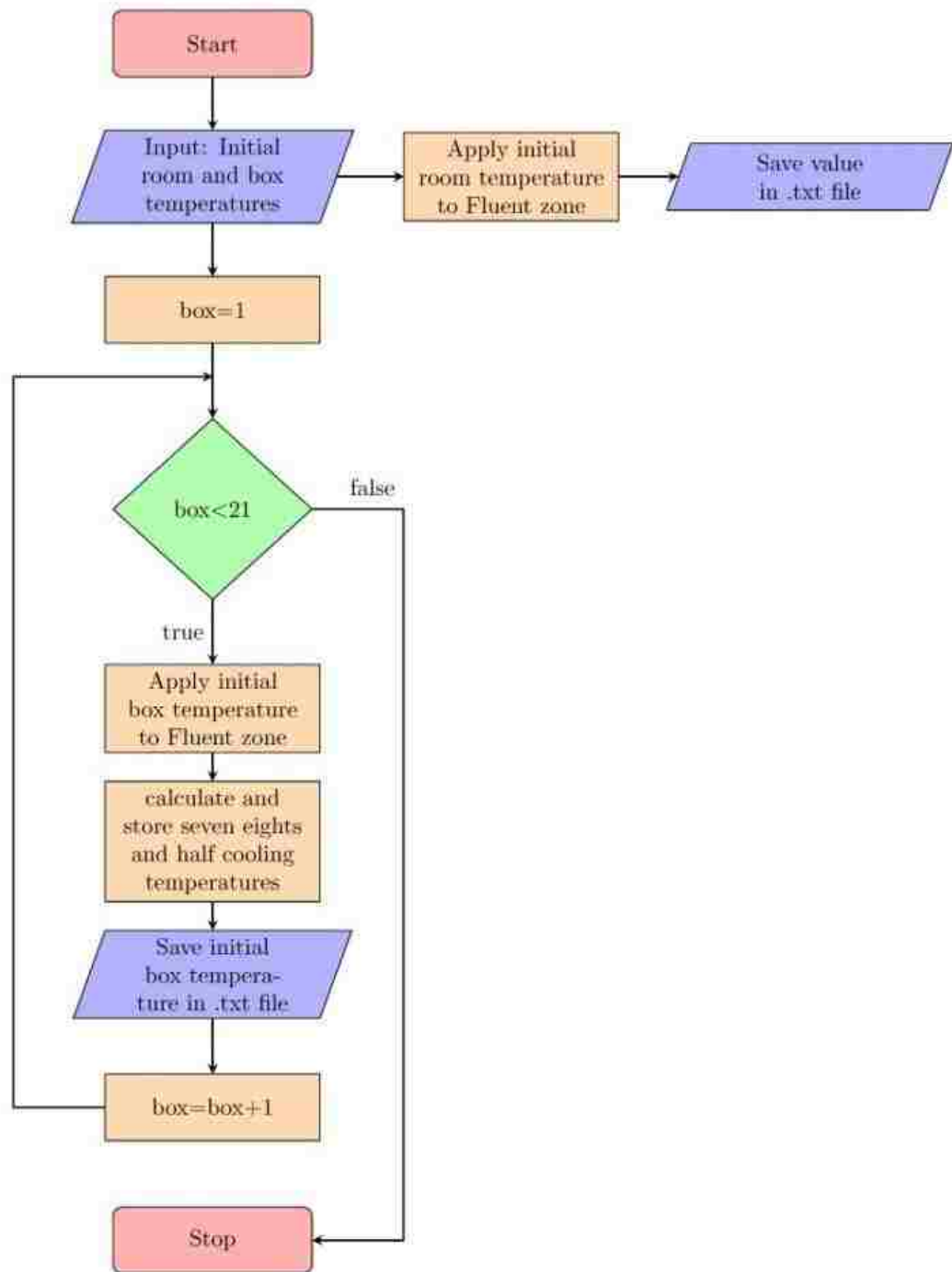
Figure H1: Initialize Flowchart

```c
/* UDF which initialized the Temperature of the boxes to
match those of the data*/
#include "udf.h"

double
Temp[20]={296.5059,296.0633,296.3793,296.7549,296.7930,296.
8311,295.7876,297.5839,297.1672,296.7505,295.7495,296.4921,
291.4679,295.8683,292.1760,288.3836,294.2593,291.7912,289.3
230,291.0190};
double Tse[20];
double Thalf[20];
double Tf=284.9792;
double time;
double RoomT;
char str[sizeof "p10.txt"];
int roomid=3.;

FILE *temperature;

/* C function that returns the Volume average temperature
of zone id*/
double roomtemp(int id)
{
Thread *t;
Domain *d;
cell_t c;

double Volume=0;
double Tr=0;

d=Get_Domain(1);
t=Lookup_Thread(d,id);

/*determining the volume average temperature*/
begin_c_loop(c,t)
{
Tr+=C_T(c,t)*C_VOLUME(c,t);
Volume+=C_VOLUME(c,t);
}
end_c_loop(c,t)
Tr=Tr/Volume;
return Tr;
}

DEFINE_INIT(ITemp,d)
{
Thread *t;
```

```
cell_t c;
int i;
int j=0;
time=0;
RoomT=0;
/*this portion saves the room temperature*/
RoomT=roomtemp(roomid);
temperature = fopen("troom.txt","a+");
fprintf(temperature,"%f %f\n",time,RoomT);
fclose(temperature);

/*this portion loops throught the produce*/
for (i=23;i>3;i--)
{
sprintf(str,"p%02d.txt",j+1);
temperature = fopen(str,"a+");
fprintf(temperature,"%f %f\n",time,Temp[j]);
fclose(temperature);
Tse[j]=(Temp[j]-Tf)*0.125 + Tf;
Thalf[j]=(Temp[j]-Tf)*0.5 + Tf;
t= Lookup_Thread(d,i);
begin_c_loop(c,t)
C_UDMI(c,t,5)=Tse[j];
C_UDMI(c,t,6)=Thalf[j];
C_T(c,t)=Temp[j];
end_c_loop(c,t)
j=j+1;
}
}
```

Figure H2: C Code for Temperature Initialization UDF

Appendix I UDF to Model Transient Room Temperature

The room temperature is not constant in the experiments and in some cases show a cyclical behavior. For this reason a Fourier series approximation is used to model the transient behavior of the room temperature. The DEFINE_PROFILE UDF macro is used to attach the code to the cold room zone of the numerical model. The UDF for the room temperature begins by inputting the Fourier series coefficients. The code then scans the flow time, inputs the flow time into the Fourier serious to determine the temperature at that specific time, and finally returns it to Fluent for use as the instantaneous room temperature. A flow chart describing the behavior of the UDF can be seen in Figure I1. The source code for the room temperature UDF can be found in Figure I2.
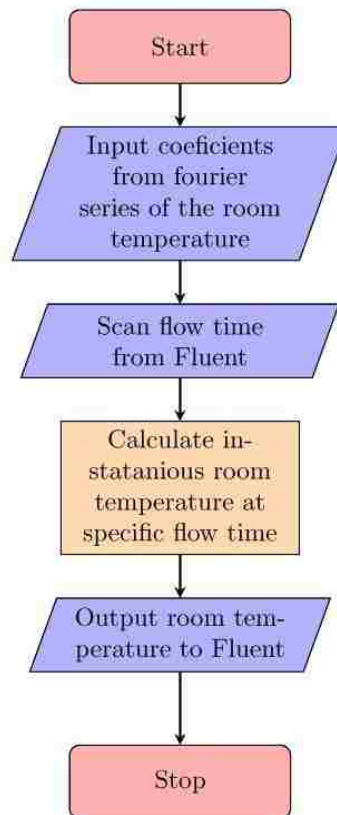

Figure I1: Room Temperature Flowchart

122

```c
/* Time dependat temperature based on a fourier series that
utilizes C_PROFILE*/
#include "udf.h"

#define PI 3.14159265359
double a[26]={572.9165,0.1944,-0.2567,0.2969,-
0.1868,0.0872,-0.0529,0.0402,-0.0507,0.0576,-0.0163,-
0.0191,0.0227,-0.0294,0.0052,-0.0112,0.0019,0.0106,-
0.0072,0.0269,-0.0408,0.0140,-0.0175,-0.0052,-
0.0007,0.0110};
double b[25]={-0.9714,0.3849,-0.1615,-
0.0183,0.0185,0.0041,-0.0116,-0.0027,0.0321,-
0.0494,0.0368,-0.0254,-0.0180,0.0305,-0.0020,0.0232,-
0.0173,0.0265,-0.0272,-0.0045,0.0063,-0.0076,0.0195,-
0.0029,0.0030};
double time;

DEFINE_PROFILE(Troom,t,nv)
{
cell_t c;
double sum_cos=0;
double sum_sin=0;
int i=1;
real Temp;
time=CURRENT_TIME;

for(i=1;i<26;i++)
{
sum_cos=sum_cos+a[i]*cos(i*PI*(2.*time/13330.-1.));
sum_sin=sum_sin+b[i-1]*sin(i*PI*(2.*time/13330.-1.));
}
begin_c_loop(c,t)
Temp=a[0]/2+sum_cos+sum_sin;
C_PROFILE(c,t,nv) = Temp;
end_c_loop(c,t)
}
```

Figure I2: C Code for Transient Room Temperature UDF

Appendix J UDF to Calculate Heat Transfer Coefficients

In some flow situations it is possible for the velocity within the container to be non-uniform. This is especially true if the flow within a pallet is not unidirectional. For these situations, the particle Reynolds number is calculated for each cell within the porous region using a UDF. A logical statement is used in order to ensure that the proper relationship is used based on the particle Reynolds number. The heat transfer coefficient is then calculated based on the flow variables at each cell and returned to fluent for input into the energy equation. A flow chart describing the behavior of the UDF used can be seen in Figure J1. The source code used to implement the UDF can be found in Figure J2.
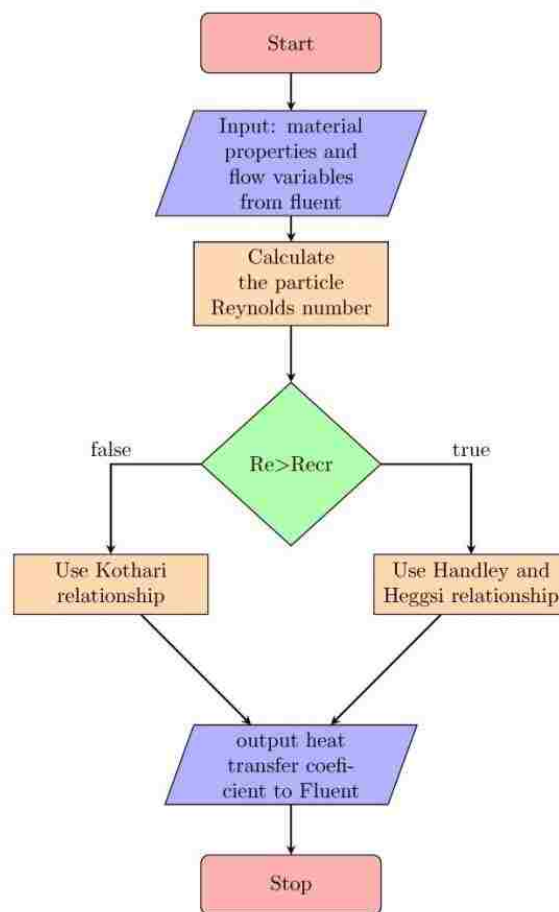

Figure J1: Heat Transfer Coefficient Flowchart

```c
/* Heat Transfer Coeficient Profile UDF in a Porous Zone
that utilizes C_PROFILE*/
#include "udf.h"
DEFINE_PROFILE(hlongDC,t,nv)
{
cell_t c;
double Nufsy;
double Nufsx;
double hfsy;
double hfsx;
double h;
double a=0.3333333333; /*power of Pr*/
double b=0.6666666667; /*power of Re*/
double Bi;
real lc = 0.0211;
begin_c_loop(c,t)
real T = C_T(c,t); /* Temperature */
real rho = C_R(c,t); /* Density */
real Cp = C_CP(c,t); /* Specific Heat*/
real mu = C_MU_L(c,t); /* Laminar Viscosity */
real ka = C_K_L(c,t); /*Thermal Conductivity of air*/
real E = 0.5737; /* Porosity (calculated)*/
real vy = C_V(c,t); /* Y-Component of velocity*/
real vx = C_U(c,t); /* X-Component of velocity*/
real kw = 0.6; /* Thermal Conductivity of Water
(estimated)*/
real dp = 0.037; /*diameter of produce 2* is for slab*/
real By = 6; /* Beta is 10,8,6 for spheres, cylinders, and
slabs*/
real Bx = 8; /* Beta is 10,8,6 for spheres, cylinders, and
slabs respectively*/
real Pr= Cp*mu/ka; /* Calculates the Prandtl Number*/
real Rey= fabs(vy*dp*rho/mu); /* Calculates the Reynolds
Number in Y */
real Rex= fabs(vx*dp*rho/mu); /* Calculates the Reynolds
Number in X */
real Recr=80.4994; /*this is the critical reynolds number
to switch nusselt coreelations*/
C_UDMI(c,t,1)=Rey; /*Displaying contours of reynolds number
in Y*/
C_UDMI(c,t,2)=Rex; /*Displaying contours of reynolds number
in X*/
if (Rey>Recr)
{
Nufsy= (0.255/E)*(pow(Pr,a))*(pow(Rey,b));
} /*calculates the films solid Nusselt Number in Y*/
else
```

```
{
Nufsy=0.033*(pow(Rey,1.3));
}
if (Rex>Recr)
{
Nufsx= (0.255/E)*(pow(Pr,a))*(pow(Rex,b));
} /*calculates the films solid Nusselt Number in X*/
else
{
Nufsx=0.033*(pow(Rex,1.3));
}
hfsy=Nufsy*ka/dp; /* calculates the film solid heat
transfer coeficient in Y */
hfsx=Nufsx*ka/dp; /* calculates the film solid heat
transfer coeficient in X */
h=1/((1/hfsy)+((dp/By)/kw))+1/((1/hfsx)+((dp/Bx)/kw));
C_UDMI(c,t,0)=h; /* checking the h value */
C_PROFILE(c,t,nv) = h;
Bi=h*lc/kw;
C_UDMI(c,t,7)=Bi; /* checking the Bi Number */
end_c_loop(c,t)
}
```

Figure J2: C Code for Heat Transfer Coefficient UDF

Appendix K UDF Used To Calculate Cooling Times

The seven eights and half-cooling times are obtained through use of the DEFINE_EXECUTE_AT_END macro within a UDF. The macro ensures that the specific code executes once at the end of each time step. The code begins by computing the average temperature of the room and stores it to file. The code then loops through each container of product checking if the temperature of each cell is greater than the seven eights and half cooling temperature. If the temperature is greater than seven eights and half cooling temperature, the current time is returned to Fluent. Once temperature is no longer greater than the seven eights or half-cooling temperature, the time will no longer be returned. The program also takes this time to save the average temperature of the produce in each container to file. Once the program has looped through all the product containers, the program terminates until the end of the next time step. A flowchart of describing the behavior of the UDF can be seen in figure K1. Finally, the source code for the UDF can be found in Figure K2.
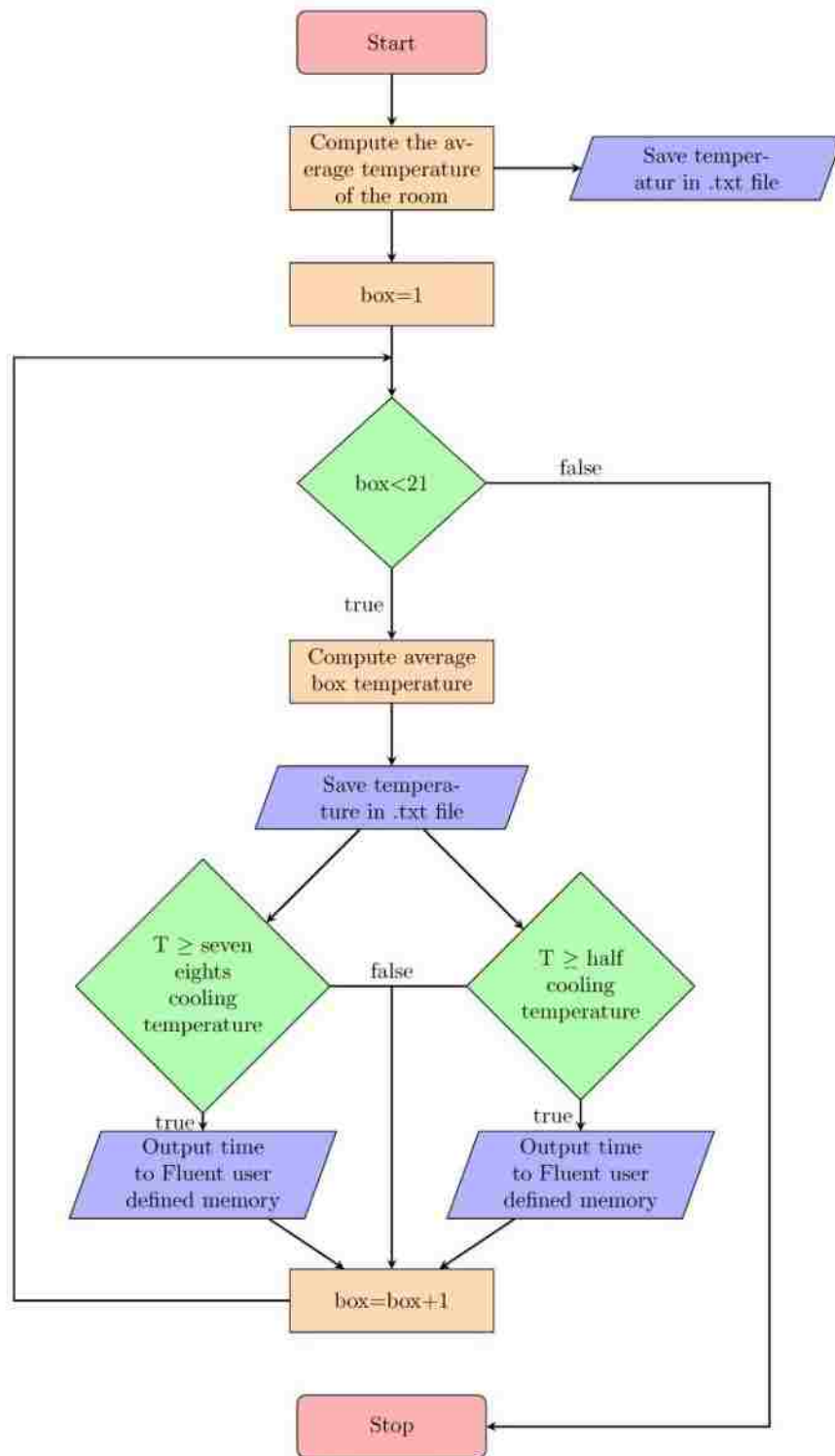
Figure K1: Cooling Time Flowchart

```c
/* UDF wich calculates and returns the Seven eights and
half cooling times*/
#include "udf.h"

extern double Tse[20];
extern double Thalf[20];
double time;
extern char str[sizeof "p10.txt"];
extern int roomid;

FILE *temperature;

/* C function that returns the Volume average temperature
of zone id*/
double boxtemp(int id)
{
Thread *t;
Domain *d;
cell_t c;

double Volume=0;
double Tr=0;

d=Get_Domain(1);
t=Lookup_Thread(d,id);

/*determining the volume average temperature*/
begin_c_loop(c,t)
{
Tr+=C_T(c,t)*C_VOLUME(c,t);
Volume+=C_VOLUME(c,t);
}
end_c_loop(c,t)
Tr=Tr/Volume;
return Tr;
}

DEFINE_EXECUTE_AT_END(CoolingTimes)
{
Domain *d;
Thread *t;
cell_t c;
double BoxT=0;
int x=0;
int i;
time=CURRENT_TIME;
```

```
/*this portion saves the room temperature*/
BoxT=boxtemp(roomid);
temperature = fopen("troom.txt","a+");
fprintf(temperature,"%f %f\n",time,BoxT);
fclose(temperature);

for (i=23;i>3;i--)
{
BoxT=boxtemp(i);
sprintf(str,"p%02d.txt",x+1);
temperature = fopen(str,"a+");
fprintf(temperature,"%f %f\n",time,BoxT);
fclose(temperature);
/*this portion maps the seven eights and half cooling times
with userdefined memory*/
d=Get_Domain(1);
t=Lookup_Thread(d,i);
begin_c_loop(c,t)
real T = C_T(c,t);
/*for seven eights cooling time*/
if (T >= Tse[x])
{
C_UDMI(c,t,3)=time;
}
if (T >= Thalf[x])
{
C_UDMI(c,t,4)=time;
}
end_c_loop(c,t)
x=x+1;
}
}
```

Figure K2: C Code for Cooling Time UDF

Vita Auctoris

Name: Jean-Paul E. Martins

Place of Birth: Windsor, Ontario

Year of Birth: 1985

Education: St. Clair College, Windsor ON

                         2004-2007 Technical Diploma

                         University of Windsor, Windsor ON

                         2007-2012 BASc

                         University of Windsor, Windsor ON

                         2012-2016 MASc